SUPERSONIC DESCENT STAGING AERODYNAMIC AND PERFORMANCE ANALYSIS

A Dissertation
Presented to
The Academic Faculty

By

David J. Blette

In Partial Fulfillment
of the Requirements for the Degree
Doctor of Philosophy in the
School of Aerospace Engineering

Georgia Institute of Technology

May 2020

SUPERSONIC DESCENT STAGING AERODYNAMIC AND PERFORMANCE ANALYSIS

Approved by:

Dr. John-Paul Clarke, Co-Advisor - Committee Chair
School of Aerospace Engineering
Georgia Institute of Technology

Dr. Robert D. Braun, Co-Advisor
School of Aerospace Engineering
Georgia Institute of Technology

Dr. Brian J. German
School of Aerospace Engineering
Georgia Institute of Technology

Dr. Charles H. Campbell
PDT Project Manager
NASA Johnson Space Center

Dr. Soumyo Dutta
Atmospheric Flight and Entry Systems Branch
NASA Langley Research Center

Date Approved: November 01, 2019

We but mirror the world. All the tendencies present in the outer world are to be found in the world of our body. If we could change ourselves, the tendencies in the world would also change. As a person changes their own nature, so does the attitude of the world change towards them. This is the divine mystery supreme. A wonderful thing it is and the source of our happiness. We need not wait to see what others do.

Mahatma Gandhi

To my Wife. To my Family. To my Friends. To my Past. To my Future.

ACKNOWLEDGEMENTS

I would like to thank both my Georgia Tech advisors, Dr. Robert Braun and Dr. John-Paul Clarke. Their guidance and advice during my time at Georgia Tech immensely shaped both my research and personal development. I appreciate them lending me their time and insight so that I may grow as a researcher and engineer. I would also like to thank all my committee members for lending me their time and expertise in reviewing my Ph.D. research.

I would like to thank my NSTRF advisor, Dr. Charles Campbell, for all his time, input, and the many back and forth brainstorming sessions that helped develop some of the early ideas for this research. I would like to thank my Langley advisor, Dr. Eric Queen, for his help in the latter stages of my Ph.D. implementing and refining various aspects of my analysis and writing. I would like to thank Dr. Soumyo Dutta for his invaluable assistance during the development of my POST2 simulations and analyses as well as his feedback on my ideas.

This work was sponsored in part by a NASA Space Technology Research Fellowship (NASA Grant NNX14AL44H) as well as a NASA Langley Pathways position. I want to thank both organizations for providing funding and a wealth of opportunities to engage in the NASA community and missions.

Finally, I would like to thank my family and friends. First, my wife, who started as my girlfriend and adventure companion at the beginning of this journey. Thank you for accompanying me on this pursuit and keeping me headed in the right direction. Thank you to my family: Phil, LeeAnna, Danielle, Steven, Karl, and Lucia. It takes a team of unwaivering supporters to achieve anything of consequence in life. My family provided that for me. Thank you to my friends and colleagues at Georgia Tech: Grant, Adam, Lin, Kier, Hisham, and Steve. I wouldn't have done it without you all.

TABLE OF CONTENTS

LIST OF TABLES

LIST OF FIGURES

SUMMARY

Supersonic Retropropulsion (SRP) is one potential enabling technology to extend Mars entry, descent, and landing (EDL) capability beyond current Viking-era technological landed mass upper limits of 1 mT to human-class landed payloads requiring 20-40 mT. To utilize SRP for human Mars missions, it is necessary to perform supersonic descent vehicle staging to transform an entry vehicle from its hypersonic configuration to a configuration that enables the use of SRP. These reconfigurations may require jettisoning the vehicle aeroshell as debris during supersonic flight. The ejected debris present risk to catastrophically recontact the primary descent vehicle during and after ejection. The flight dynamics of the ejected debris are complicated by supersonic interference aerodynamics between the primary descent vehicle and the ejected debris. The development of strategies to understand and mitigate debris recontact risk during supersonic descent vehicle reconfigurations is paramount to advancing SRP technology readiness level and therefore to enabling human missions to Mars. However, supersonic descent vehicle staging has not been flight proven and published research in the field is non-existent.

The methodology developed in this thesis represents the first assessment of supersonic descent staging aerodynamic and performance analysis. The methodology addresses a gap in current analysis capability by providing the means to rapidly, quantitatively, and competitively evaluate a variety of proposed supersonic vehicle staging architectures to determine a subset of fittest candidates for further detailed investigation. Quantitative methodology output metrics consist of required ejection subsystem performance for a variety of jettison initiation conditions and jettison maneuver durations. The methodology also serves as a risk mitigation tool by enabling users to specify tolerable levels of recontact risk posed to the primary descent vehicle by the ejected debris.

The methodology employs an iterative process between three primary analysis modules. The first module analyzes a piece of debris to determine the spatial flight envelope of the

debris when it undergoes uncontrolled tumbling. The second module determines nominal flight trajectories that the debris must fly post-separation to ensure minimum offset distances are achieved between the primary vehicle and the debris before uncontrolled debris tumbling begins. The third module determines uncertainties about the nominal transit trajectories. The methodology iterates until successive solutions converge. The methodology is demonstrated on a 10x30 meter ellipsled entry vehicle utilizing a symmetric clam-shell supersonic aeroshell jettison maneuver for a reference human Mars mission.

As a supplement to the methodology contribution, multi-fidelity modeling techniques are evaluated for applicability toward generating surrogate models of expensive interference aerodynamic responses by leveraging available inexpensive isolated aerodynamic response data. Multi-fidelity modeling techniques are found to improve the accuracy and k-fold cross-validation metrics of interference aerodynamics drag coefficient surrogate models as compared to single-fidelity modeling techniques. Multi-fidelity modeling techniques performed particularly well for models built from sparse sets of interference data.

CHAPTER 1
INTRODUCTION AND THESIS ORGANIZATION

1.1 Background

The present work investigates separation subsystem performance requirements for human-scale supersonic descent jettison maneuvers such as the ejection of an aeroshell prior to the ignition of supersonic retropropulsion during a human mission to the Martian surface. The work addresses a gap in current analysis capability to quantitatively competitively evaluate a variety of proposed supersonic vehicle staging architectures to determine a subset of fittest candidates for further detailed investigation.

There is currently no published work on descent supersonic staging. There is a wealth of published work on the topic of ascent supersonic staging, primarily centered around booster separation from ascent vehicles such as the Space Shuttle. There are several important differences between ascent staging and descent staging. Due to the direction of motion during descent staging, the vehicle and debris move in the same direction after separation (Figure 1.1), where as they move in opposite directions during ascent staging. The co-motion of the vehicle and debris increases the duration that objects are in near-field proximity as compared to ascent vehicles and introduces far-field recontact risks for descent staging that are not present for ascent staging.

The methodologies and analysis techniques developed during the design of the Space Shuttle ascent booster separation served as the foundation of all subsequent parallel stage ascent separation analyses. The design approach can be summarized as follows. An analysis typically begins late in the vehicle design phase when the vehicle design and configuration have largely been determined based on considerations from other disciplines. High fidelity interference aerodynamics are developed either experimentally or computa-

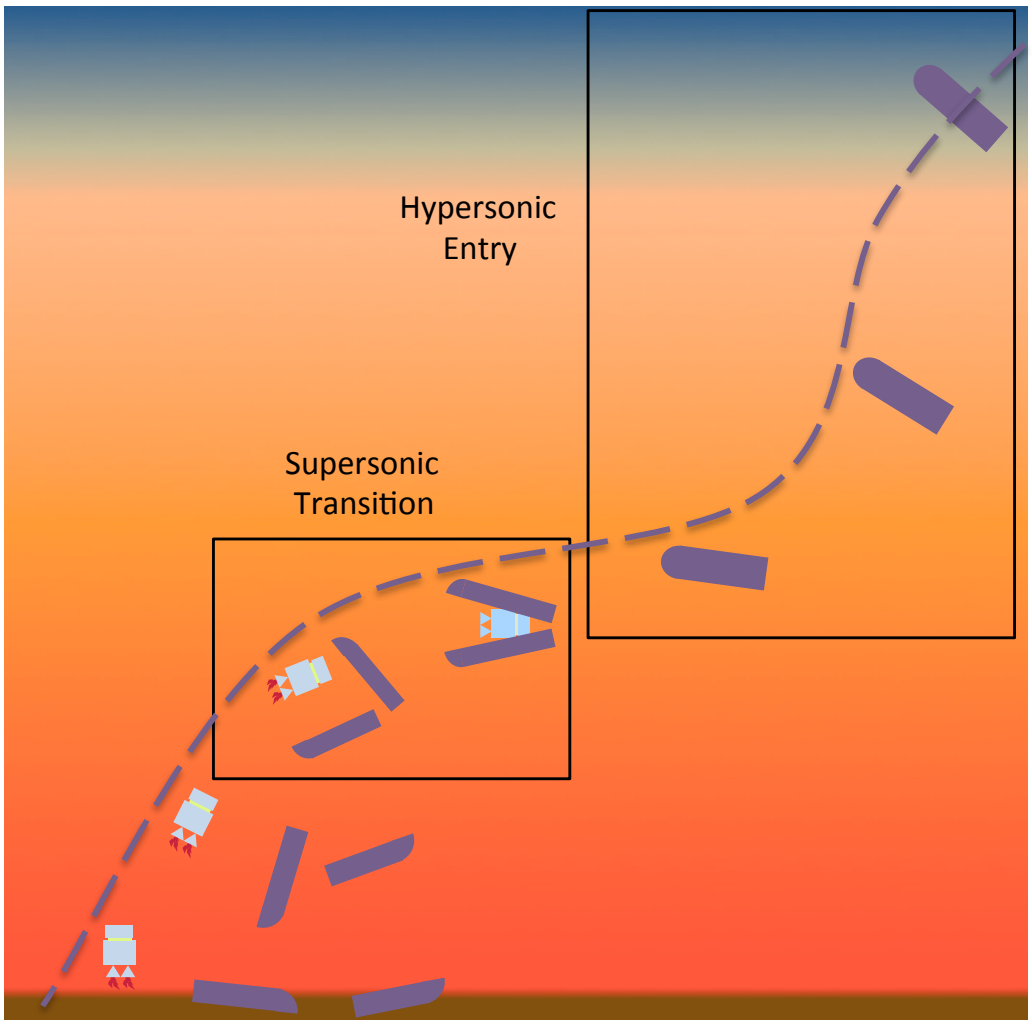

Figure 1.1: An illustration of a supersonic vehicle reconfiguration during Mars EDL [1]. In the depicted transition architecture, the descent vehicle supersonically sheds its aeroshell prior to supersonic retropropulsion initiation. Notice that after the aeroshell is separated from the primary descent vehicle, the debris falls in the same direction of motion as the descent vehicle.

tionally. Due to the number of independent variables involved in a proximity aerodynamic database, the development of these databases is extremely costly and time intensive. Having developed the interference database, high fidelity flight dynamics simulations are used to determine the feasibility of the proposed separation scheme and whether or not any recontact risks occur. These simulations are developed to look at a short duration of flight prone to near-field recontacts, where the primary vehicle and the debris are in close proximity. In an ascent separation, ejected debris falls in the direction opposite to the primary vehicle's motion. Consequently, the time during which the two bodies are in close proximity is very short, on the order of 3-5 seconds. If a passive aerodynamic separation is infeasible, the separation design may be augmented to include aerodynamic control surfaces or solid rocket separation motors. Because separation analyses typically occur late in the ascent vehicle design phase, designers have very limited options available to them to modify the separation system. Typically, designers must follow the mentality of "make the given vehicle configuration work" instead of "determine the optimal separation vehicle configuration."

This separation design methodology has been utilized extensively in ascent separation analyses and has proven effective for ascent vehicle designs that do not deviate significantly from the vehicle architecture pioneered for the Shuttle program. While ascent and descent supersonic separations share many of the same challenges, including threats due to debris recontact and complex interference aerodynamics acting on similar size objects in proximity, supersonic descent separations involve significantly enhanced challenges. Due to the co-motion of the primary vehicle and ejected debris (see Figure 1.1), near-field recontact risks exist over much longer flight times. The co-motion also introduces the challenges of far-field vehicle recontact risks and risks to pre-deployed ground assets near the landing zone.

Ascent vehicle configurations were explored extensively during the Apollo and Shuttle programs. Trade studies considered many alternative designs before settling on the ubiq-

uitous series and parallel staging vehicle configurations we are familiar with today. The current state of the human Mars descent vehicle reference architecture is significantly more volatile. The NASA human Mars reference mission architecture has changed every few years. Some proposed architectures call for landed payload masses on the order of 10 mT while other architectures call for 40 mT [2]. It is currently unclear what landed mass capability will be required of future human vehicles or what suite of descent technologies will be used to put humans on the surface. Numerous studies have concluded that SRP is very likely necessary for human mars EDL [3], but it is less certain which deceleration technology will be utilized directly before SRP initiation. Some studies baseline a slender lifting aeroshell that transitions directly to SRP [2], while other studies consider the use of aerodynamic inflatable decelerators before initiating SRP [3].

The expansive nature of the challenges involved in descent separations combined with the changing nature of human Mars descent vehicle reference architectures and mission performance requirements make the use of time intensive heritage ascent separation analysis methodologies unsuitable for descent separation analysis. Each analysis that is performed using the detailed, low-level ascent methodology absorbs significant time and resources, making it infeasible for mission designers to find the optimal descent separation architecture given the significant number of unknowns, the fickle nature of human Mars reference missions, and the limited time and resources allocated for separation studies. A new tool is required that is suitable for making rapid, high-level decisions commensurate with the current high level and malleable nature of Mars reference missions.

1.2 Methodology to Determine Ejection Subsystem Performance Requirements to Mitigate Descent Debris Recontact Risks

A methodology is put forth to address the need for rapid, high-level systems analysis of supersonic descent separation architectures. The methodology provides high-level estimates of ejection sub-system performance requirements necessary to successfully achieve a safe

debris (aeroshell) separation with respect to far-field recontact risks. Separation subsystems considered in this work are assumed to be composed of a combination of debris center-of-gravity thrust and debris aerodynamic control immediately following physical separation from the primary descent vehicle. The present work demonstrates the methodology by studying the ejection of an aeroshell from a 10x30 meter ellipsled vehicle immediately prior to ignition of supersonic retropropulsion. After ejection, the aeroshell is considered hazardous debris. Far-field recontact risks are catastrophic collision risks posed by an ejected piece of debris after it has initially been successfully separated. Far-field risks are posed to either the primary vehicle or pre-deployed ground assets near the primary descent vehicle landing site (e.g. habitat, power generation plant). Risks associated with the process of initially jettisoning debris are termed near-field recontact risks and are not addressed in this analysis.

The methodology utilizes an iterative process between three main analysis modules. The first module analyzes a piece of debris to determine the spatial flight envelope of the debris when it tumbles. This debris envelope forms a keep-out zone that the primary descent vehicle must not fly through. Prohibiting the primary vehicle's flight trajectory through the debris field achieves two goals. First, in-flight far-field recontact risks between the debris and primary vehicle are avoided. Second, the primary vehicle is assumed to be landing near pre-deployed ground assets such as human habitats or power generation facilities. Prohibiting the debris field from overlapping with the primary vehicle trajectory mitigates the risk of debris causing damage to these pre-deployed ground assets.

The second methodology module assumes the ejected debris is actively controlled for a period of time between the initial jettison and a point at which the debris is no longer actively controlled and begins to tumble. This segment of flight is termed the transit trajectory. An optimized transit trajectory is determined such that the debris achieves a minimum safe proximity distance with respect to the primary vehicle before the debris begins to tumble. The minimum safe proximity distance is defined to be the distance between the primary

vehicle and the debris at the time of tumbling such that the tumbling debris field does not overlap with the primary vehicle descent trajectory to the Martian surface. Debris angle of attack and center of gravity thrust are optimized to determine a transit trajectory that satisfies minimum safe proximity distance constraints while minimizing separation subsystem mass. Separation subsystem mass is assumed to be proportional to the thrust magnitude, thrust propellant, and required debris trim angle of attack.

The third methodology module determines transit trajectory end-state uncertainties. Uncertainties are then plugged into the first methodology module to update flight parameters and begin the next iteration of the methodology. The methodology is considered converged when successive iterations of the methodology arrive at the same solution. In practice, the optimization space is highly nonlinear and volatile, so bounded convergence is accepted in lieu of asymptotic convergence. Bounded convergence is taken to mean successive methodology iterations produce solutions within a bounded range of a mean-value solution.

In addition to providing sub-system performance estimates, the methodology inherently provides a risk-mitigation strategy for far-field recontact. Subsystem performance estimates are developed around the core principle that far-field recontact risks must be mitigated to a user-specified level. The present study utilizes a 95% far-field recontact risk mitigation approach. The debris field is constructed such that 95% of Monte Carlo tumbling debris trajectories are encapsulated within the bounding structure. Since the transit trajectory is optimized to ensure the primary descent vehicle trajectory does not overlap with the debris field, a 95% confidence interval is obtained on mitigation of far-field recontact risks. Alternatively, a user could have specified the debris field to bound 80% or 99% of tumbling debris trajectories, for example, and obtained far-field recontact risk confidence intervals of 80% or 99%, respectively.

Each module may be constructed according to a user defined set of assumptions. The assumptions associated with a particular module implementation limit the applicability of

methodology results in-line with the assumptions made. However, the methodology is deigned with flexibility in mind and can generate results for a variety of user-input module assumptions. In this way, the final fidelity of the methodology outputs is, to an extent, a user input. The user is required to determine what level of fidelity to trade for ease, speed, and cost of simulation. As an example, the assumption that the debris free-tumbles at the end of the transit trajectory could be replaced by a passive-stabilization system such as a trailing aerodynamic decelerator or spin stabilizing the debris. Both approaches would increase the complexity of the separation system for the benefit of reducing the span of the debris field thereby decreasing minimum required offset distance constraints and required ejection subsystem performance during the transit trajectory.

This methodology is developed to address a gap in current simulation capabilities to perform high-level, rapid assessment of a multitude of proposed descent vehicle and jettison architectures. It is not intended, nor designed, to perform high-fidelity, low-level, detailed analysis of a specific descent jettison architecture. Rather, it is designed to provide rapid, quantitative data to be used to down-select among many proposed architectures in order to choose a limited set of the most promising architectures on which to perform further detailed, in-depth analysis.

The work presented in this dissertation is envisioned to lay the foundation of a methodology that can be further developed and adapted to suit a variety of mission design needs. One envisioned improvement is the incorporation of interference aerodynamics into the simulation to provided improved estimates of required system performance. Currently, the methodology generates approximated required ejection subsystem performance and relative vehicle trajectories under the influence of isolated aerodynamics. Interference aerodynamic force perturbations have the potential to disrupt these isolated trajectories and affect required ejection subsystem performance.

A final contribution of this dissertation presents a multi-fidelity modeling approach to improve interference aerodynamic model fidelity for a small amount of available interfer-

ence data by leveraging a comparatively larger amount of available isolated aerodynamic data. The use of the present methodology requires the development of extensive isolated aerodynamic databases for all body geometries involved in an investigation. These extensive databases are sufficient to generated data-saturated models of the underlying isolated aerodynamic responses. The multi-fidelity modeling contribution shows these isolated aerodynamic response models may be used in combination with sparse interference aerodynamic data to generated higher-fidelity interference aerodynamic response models than if pure interference data alone is use to generate the response models.

1.3 Contributions

The goal of this work is to develop a methodology to enable rapid, quantitative, and competitive high-level analysis of descent vehicle supersonic reconfiguration architectures. The intended use of the methodology is to aid mission designers in understanding the benefits and costs of a particular descent vehicle reconfiguration architecture before investing significant time and resource in low-level, detailed analyses of the same reconfiguration architecture. Additionally, multi-fidelity modeling techniques are evaluated for their potential to increase the accuracy of interference aerodynamic coefficient surrogate models as compared to more common single-fidelity modeling techniques. This body of work puts forth two main contributions to advance the state of the art.

1.3.1 Methodology to Determine Ejection Subsystem Performance Requirements Necessary to Mitigate Descent Debris Far-Field Recontact Risks

The methodology provides high-level estimates of ejection sub-system performance requirements necessary to achieve a safe debris (aeroshell) separation with respect to far-field recontact risks. Separation subsystems considered in this work are assumed to be composed of a combination of debris center-of-gravity thrust and debris aerodynamic control immediately following physical separation from the primary descent vehicle. In the

context of this work, a safe debris separation is taken to mean the primary vehicle does not fly through the debris field of a tumbling piece of debris. This assumption ensures far-field debris recontact risks to the primary vehicle and risks to pre-deployed ground assets near the primary vehicle landing site are contained to a user-specified confidence interval.

The methodology utilizes an iterative process between three main analysis modules. The first module analyzes a piece of debris to determine the spatial flight envelope of the debris when it tumbles. The second module optimizes the relative-motion trajectory of the jettisoned debris as it actively maneuvers away from the primary vehicle until a sufficient offset distance is achieved such that when the active debris control is terminated, the span of the tumbling debris field will not overlap with the primary vehicle descent trajectory. The third and final module determines uncertainties about the end-state of the debris relative-motion trajectory. These uncertainties feed back into the first module to complete one iteration of the methodology.

The methodology is demonstrated on the ejection of an aeroshell from a 10x30 meter ellipsled Mars descent vehicle immediately prior to ignition of supersonic retropropulsion.

1.3.2 Application of Multi-Fidelity Modeling Techniques to Model Interference Aerodynamic Responses by Leveraging Isolated Aerodynamic Data

Multi-fidelity modeling techniques are applied to the task of modeling interference aerodynamic drag as a function of angle of attack for one of three bodies in near proximity. NASA's CART3D solver is used to generate aerodynamic data. The configuration of bodies in the interference aerodynamic solutions is meant to represent a hinged-exit reconfiguration architecture at supersonic flight conditions. In the context of multi-fidelity modeling, interference aerodynamics represent expensive data sets and isolated aerodynamics represent cheap data sets. Cross-validation metrics are used to assess the quality of surrogate models. Results show multi-fidelity models generally out-perform single-fidelity models. This performance difference is most significant in models with sparse training sets of data.

1.4 Thesis Organization

The remainder of this thesis is organized as follows. Chapter 2 provides detailed background information pertinent to the present research task. An in-depth review of the literature from relevant fields is presented. Chapter 3 presents details of the Methodology to Determine Ejection Subsystem Performance Requirements to Mitigate Descent Debris Recontact Risks. A methodology overview is presented followed by low-level details of each step of the methodology. Details are presented in-line with an example analysis of a separation system proposed by the Entry, Descent, and Landing Systems Analysis study [4] performed by NASA. Discussion on how to interpret and use the methodology output metrics is presented along with an exposition on the advantages of using the methodology. Chapter 4 presents an approach to improve interference aerodynamic response models using multi-fidelity modeling techniques in combination with sparse interference aerodynamic data and dense isolated aerodynamic data. Chapter 5 summarizes the research performed within this dissertation and presents recommendations for future work that would improve upon or enhance the present research.

CHAPTER 2
BACKGROUND AND LITERATURE REVIEW

2.1 Entry, Descent, and Landing

Entry, descent, and landing (EDL) is the field which focuses on entering and transiting the atmospheres of orbital bodies while decelerating a payload safely to the body's surface. The EDL sequence comprises only a small fraction of a total mission timeline yet drives many mission constraints, including landed payload mass and target landing accuracy. Characteristic challenges of an EDL sequence include mitigating significant heating during the hypersonic flight regime, sufficiently decelerating through an atmosphere, and achieving an intact landing within a specified accuracy tolerance on location and touchdown velocity.

2.1.1 Mars EDL

The Martian atmosphere is approximately 1/100th the density of Earth's atmosphere at sea level. The tenuous Mars atmosphere makes decelerating high mass payloads difficult yet is still dense enough to cause significant aerodynamic heating during entry [5, 6, 7]. Upon entry, a descent vehicle must traverse hypersonic, supersonic, transonic, and subsonic flight regimes before finally landing on the Martian surface. A successful mission must overcome unique technical challenges in each flight regime, be they heating, stability, targeting accuracy, or deceleration. No one technology has been developed that addresses all challenges in all flight regimes. Rather, to meet these complex demands, a series of engineering technologies are used in combination to achieve successful EDL.

To-date, eight landers have successfully landed on the Martian surface: Viking 1 and 2 (1976), Mars Pathfinder (1997), Mars Exploration Rovers (MER) Opportunity and Spirit (2004), Phoenix (2008), Mars Science Laboratory (MSL) (2012), and Mars Insight Lan-

der (2018). The Viking missions were unhampered by more restricted budgets typical of recent programs and were marked by extensive technology development and flight and ground testing [5, 8, 6, 7]. The culmination of this aggressive technology development effort yielded the development and qualification of EDL systems that would benchmark all successive U.S. Mars missions over the next 40 years. The Viking EDL sequence consisted of a rigid, blunt body 70° sphere-cone aeroshell for hypersonic deceleration, a disk-gap-band parachute for supersonic and transonic deceleration, and subsonic retropropulsion for terminal descent and touchdown.

The 70° sphere-cone aeroshell (Hypersonic C_D of 1.68 [6]) dissipated the majority of the vehicle's kinetic energy. To mitigate the high heat loads and heat rates during hypersonic flight, an ablative thermal protection system was fixed to the aeroshell. The diameter of the aeroshell was too small to sufficiently decelerate the vehicle through the low density atmosphere for subsonic retropropulsion initiation. A disk-gap band parachute was deployed at Mach 1.1 to increase drag and provide stability through transonic flight. The parachute deployment Mach number was constrained by material strength, dynamic pressure, and inflation qualification. Following a subsonic vehicle reconfiguration in the form of a heatshield ejection, subsonic retropropulsion was used to decelerate to a vertical touchdown velocity of 2.4 $\pm$ 1 m/s [6].

Subsequent missions leveraged the heritage Viking technology as a baseline architecture, upon which incremental improvements were made [6]. The Mars Pathfinder mission used the Viking entry and parachute systems along with the use of solid rocket boosters just before touchdown to eliminate most of the vehicle's kinetic energy [9]. The touchdown phase was accomplished by a 4π steradian airbag system capable of handling much higher touchdown velocities than the previous Viking missions [10]. The MER missions improved on the durability of the Pathfinder airbag system and included horizontal velocity sensing and control during terminal descent [11]. The Mars Science Laboratory utilized hypersonic lifting entry guidance with RCS for control and the skycrane propulsive-hover terminal de-

Table 2.1: EDL properties of successful US Mars missions. (Adapted from [6]) [11, 17]

	Viking 1976	Pathfinder 1997	MER 2004	Phoenix 2008	MSL 2012
Lander Mass (t)	0.244	0.092	0.173	0.167	0.9
Entry Mass (t)	0.99	0.58	0.83	0.6	3.15
Ballistic Coefficient (kg/m^2)	64	63	94	70	145
Aeroshell Diameter (m)	3.5	2.65	2.65	2.65	4.5
Parachute Diameter (m)	16	12.5	14	11.7	21.3
Parachute Deploy Mach	1.1	1.57	1.77	1.65	1.75

scent system. The EDL improvements made by post-Viking missions primarily focused on modifying the terminal descent segment or, in the case of MSL, the hypersonic segment. While successive, incremental improvements have been made to supersonic decelerator systems [12, 13, 14, 15, 16], all US Mars landers have relied on the Viking-qualified disk-gap band parachutes operated within the flight regime defined by the original development program.

2.1.2 Future High Mass Mars EDL

Since the original Viking program, all subsequent successful Mars missions have followed a trend of increasing lander mass (with the exception of Mars Pathfinder) but have continued to rely largely on the original Viking EDL sequence and technologies. Table 2.1 summarizes the EDL properties of these missions. The succession from the current state of the art along NASA's goal of extending and sustaining human presence in our solar system will require landing large robotic (10 mT) and human class payloads (40-80 mT) on Mars with landed accuracies on the order of meters.

It is estimated that MSL approached the upper limit of landed mass and landed altitude capability of the heritage Viking EDL sequence and technologies. To push past this limit, the EDL sequence must be reexamined and new technologies must be developed. The use of parachutes for deceleration in the supersonic flight regime suffers from particularly poor scaling for payloads beyond MSL. As parachute diameters increase to generate the

increased drag required by larger payloads, the loading forces exerted on the parachutes may exceed the current state of art of parachute materials. Additionally, parachute inflation times scale up with parachute diameter. For human scale missions, high parachute inflation times may present an insurmountable constraint on the EDL sequencing timeline. Increasing the deployment Mach number may extend the EDL timeline, however, higher Mach deployments suffer from decreased drag performance, increased aerothermodynamic heating, and increased inflation time [3].

The ballistic coefficient, β, defined in Eq. 2.1, is an important parameter in entry, descent, and landing. It relates inertial forces to aerodynamic forces. To maintain a set ballistic coefficient, an increase in entry mass (m) must be accompanied by an increase in drag area (A_D) and/or drag coefficient (C_D). There is little design flexibility in the drag coefficient with aeroshell shape variations. The 70 deg sphere-cone aeroshell has a drag coefficient of 1.68 and has been used by all landed Mars missions. Its repeated use is primarily due to favorable stability and aerothermodynamic heating properties. Rigid aeroshells, like those used on all Mars landed missions, are constrained in diameter by the size of the Earth launch vehicle payload fairing. Therefore, an increase in landed mass typically results in an increased hypersonic ballistic coefficient as illustrated in Table 2.1.

$$\beta = \frac{m}{C_D A_D} \tag{2.1}$$

Entry vehicles with higher ballistic coefficients penetrate deeper into the atmosphere before decelerating significatnly and have a shorter EDL timeline. Altitude velocity space of entry vehicle trajectories for a range of ballistic coefficients is shown in Figure 2.1. Supersonic parachute deployment is constrained by material strength properties, inflation characteristics, and drag performance. These constraints impose limitations on deployment Mach number and dynamic pressure. As is evident in Figure 2.1, MSL (β = 145 kg/m^2) barely traverses the parachute deployment region. It is likely infeasible to utilize parachutes for supersonic deceleration for large robotic or human class missions. To extend landed

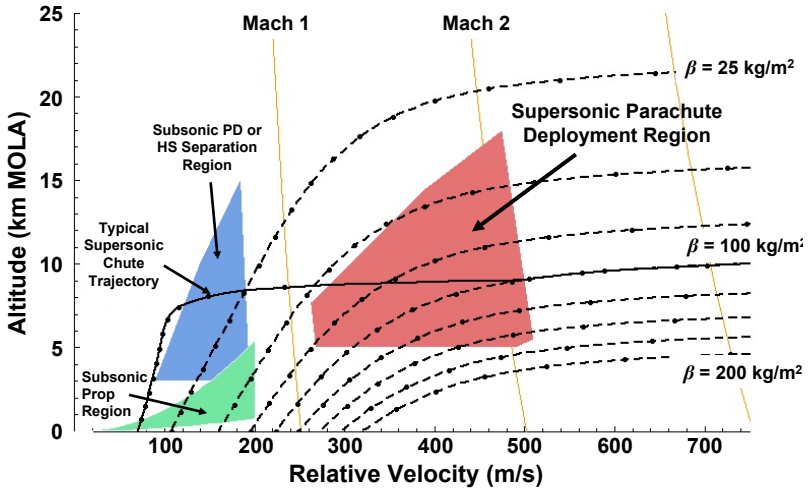

Figure 2.1: Mars entry trajectories for increasing ballistic coefficient vehicles along with feasibility regions for supersonic parachute deployment. (Image originally presented in [6], then adapted in [18])

mass capabilities significantly beyond that of MSL, new supersonic deceleration technologies must be developed.

2.2 Supersonic Retropropulsion

One candidate technology to enable high-mass Mars missions is supersonic retropropulsion (SRP), illustrated in Figure 2.2. SRP is a method of decelerating an entry vehicle in the supersonic flight regime by directing propulsive thrusters opposite to the oncoming aerodynamic flow. SRP is believed to scale well across a wide range of vehicle architectures and benefits from increasing returns for increasing missions mass.

2.2.1 Early SRP Testing Campaigns

The concept of SRP originates back to the Viking program development [20, 21, 22, 23, 24] when it was investigated for use on an early all-propulsive Viking mission design [25]. Early investigations from the 1950's through the 1970's conducted subsonic and supersonic wind tunnel tests on central nozzle SRP configurations, illustrated in Figure 2.3. The rock-

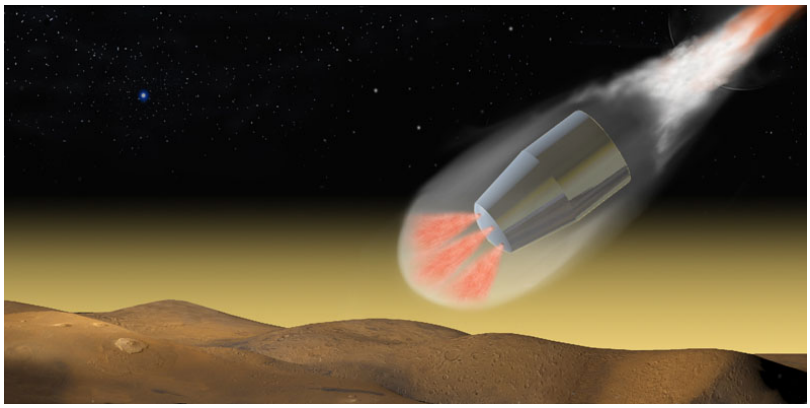

Figure 2.2: An illustration of a vehicle utilizing SRP (image credit: [19]).

ets in these wind tunnel tests exhausted air into a free stream flow of air. No attempt was made to simulate realistic rocket exhaust chemical compositions. Investigators sought to understand how a rocket jet exhausting into an opposing flow would alter blunt body aerodynamics. These early studies showed that aerodynamic drag preservation decreased with increasing jet pressure [23, 24, 20, 26].

These testing campaigns determined that characteristics of drag preservation were strongly correlated to a non-dimensional thrust coefficient, c_T, given in Eq. 2.2, where F_T is the engine thrust, q_∞ is the free-stream dynamic pressure, and A is a reference area. For $c_T < 1$ a percentage of the thrust-off aerodynamic drag was preserved. For $c_T > 1$, negligible drag was preserved and vehicle motion was dominated by the SRP engine thrust [27, 28, 29].

Additional SRP wind tunnel tests performed expanded investigations of alternative forebody nozzle configurations, including the three-nozzle peripheral configuration shown in Figure 2.3. These studies concluded peripheral configurations had improved drag preservation at low c_T values but preservation vanished at high c_T values [30]. These studies further revealed that the number of nozzles and nozzle configurations had a strong impact on the amount of drag preservation, especially at low c_T values.

$$c_T = \frac{F_T}{q_\infty A} \tag{2.2}$$

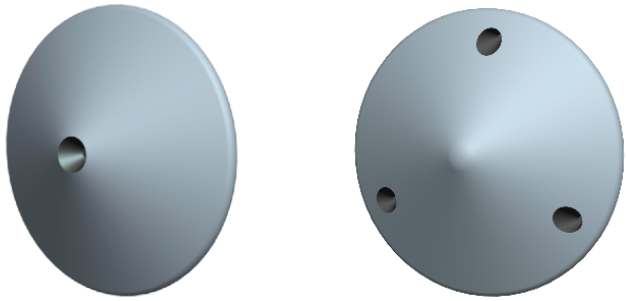

Figure 2.3: Central (left) and peripheral (right) forebody nozzle configurations (image credit: [18]).

These early investigations formed the foundational work on SRP and defined the state of the art for the next several decades. Following the Viking program's decision to utilize supersonic parachutes over SRP for supersonic deceleration, efforts to develop SRP came to an abrupt halt.

2.2.2 Recent SRP Testing Campaigns

Interest in SRP picked up again in the mid 2000's as NASA looked ahead toward manned Mars missions requiring deceleration technologies suitable for high mass missions. A new wind-tunnel test campaign sought to generate experimental data for CFD based SRP simulation validation and calibration [31, 32, 33, 34]. The test articles used both central nozzle and peripheral nozzle configurations, shown in Figure 2.4a. The models were instrumented with static pressure ports and high frequency pressure transducers. High speed schlieren images were collected to investigate flow field features as shown in Figure 2.4b.

Wind tunnel testing is not currently capable of simultaneously reproducing all flight environment properties for Mars EDL. Computational fluid dynamics (CFD) help engineers simulate flight-like environments without having to perform expensive flight tests. Recent SRP development efforts have focused on improving CFD capability to accurately simulate the flow phenomenon of an SRP rocket exhausting into an oncoming aerodynamic flow. Initial CFD simulations utilized inviscid solvers, which are computationally less expensive

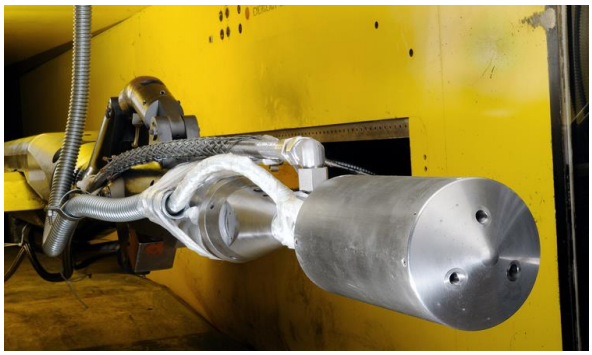

(a) SRP wind tunnel test article (image credit: [33]).

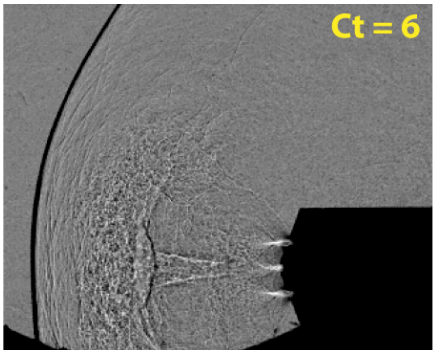

(b) High speed schlieren photography of SRP test run (image credit: [32]).

Figure 2.4: SRP experimental wind tunnel test

than viscous solvers, to model SRP physics and flow fields. These simulations successfully predicted the locations of primary flow features such as the bow and jet terminal shocks, surface distributions, and axial body force coefficients as illustrated by Figure 2.5 [35, 36, 37]. Further studies utilized higher fidelity, viscous, steady state and time accurate solvers to improve fluid structure resolution and performance predictions [38, 39, 36, 40, 41].

One recent study looked at the viability of several SRP vehicle designs utilizing novel nozzle locations and cant angles [42]. This study performed CFD analysis on SRP vehicles employing rocket nozzles with varying degrees of cant angles in both forebody and aftbody configurations. Results showed improved net drag performance for forebody configurations with moderate cant angles and thrust coefficients. Vehicles employing high thrust coefficients saw minimal forebody drag preservation and no resulting drag perfor-

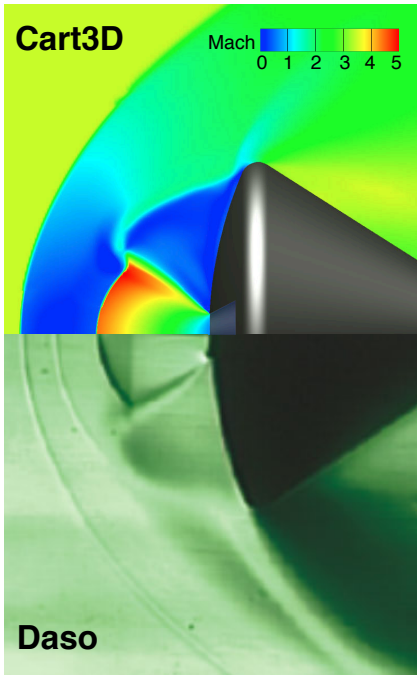

Figure 2.5: Comparison of CFD predictions versus Experimental data for a SRP flow (image credit: [35]).

mance benefit. Vehicles employing high cant angles suffered from cosine thrust losses and saw no net drag performance benefit regardless of the observed improvement in forebody drag preservation. Vehicle designs utilizing aftbody engine configurations with moderate cant angles ($30°$) showed improved vehicle stability and higher forebody drag preservation resulting in improved net drag performance [42].

The first flight test of EDL Mars relevant SRP was performed by SpaceX in September 2013. The private space company utilized SRP to assist with 1st stage recovery for their Falcon 9 rocket. After the first stage ascent separation, the main engines were reignited at supersonic conditions to slow down the vehicle and then again to execute a precision landing. SRP engine ignition conditions closely matched the Mach and dynamic pressure flight regime that would be experienced on Mars during high mass EDL. NASA formed a partnership with the private space contractor to collect and analyze data from the Falcon 9 first stage SRP descent in order to further the technology readiness of SRP for a Mars

mission [43].

2.2.3 Mars Human Exploration Mission Architectures

During the relentless technology development that accompanied the Viking program, parachutes beat out SRP to become the baseline supersonic decelerator technology. Inflatable supersonic decelerators benefit from favorable mass performance for low mass missions but the technology qualification and viability do not scale well with mission mass. For high mass Mars EDL, SRP takes the edge over inflatables due to its scalability and applicability to a wide range of mission classes.

NASA has steadily worked to define mission architectures that could enable Mars human exploration [3, 2, 44, 45]. NASA's Mars Design Reference Architecture 5.0 (DRA5) [2] study sought to determine the minimum required EDL technology capabilities to deliver a 40 mT payload to the surface of Mars. The proposed architecture employed a 10x30 meter ellipsled aeroshell with mid lift-to-drag for aerocapture and hypersonic descent. SRP initiation occurs at Mach 2 and is used all the way to touchdown. No method was proposed to transition the descent vehicle from the hypersonic aeroshell configuration to a configuration in which retro-engines are exposed to the flow and SRP may be initiated.

NASA's Entry, Descent, and Landing System Analysis (EDLSA) [3] study built upon the DRA5 efforts and investigated alternative descent strategies. Eight candidate EDL architectures put forth by the EDLSA are shown in Figure 2.6. Architectures 1 through 4 utilize supersonic retropropulsion. All eight architectures utilize retropropulsion for subsonic terminal descent. SRP was identified as a key element on the list of recommended EDL technologies due to the ability to build redundancy in to the descent architecture and to provide flexible propulsive capability for potential trajectory divert maneuvers [3].

As part of the appendix of the EDLSA study, the authors proposed several notional transition architectures to transform the hypersonic descent vehicle into a an SRP ignition-capable configuration [3]. The proposed transitions, shown in Figure 2.7 were notional

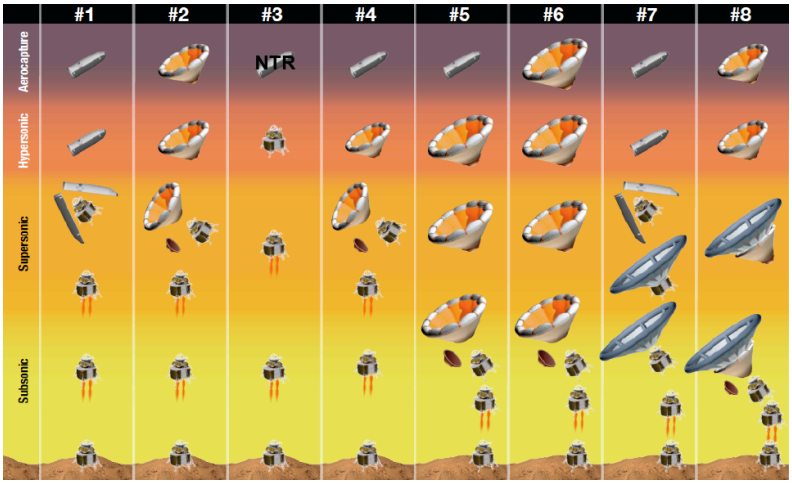

Figure 2.6: High-mass Mars mission architectures proposed by the EDLSA. All architectures utilize subsonic retropropulsion. Architectures 1 - 4 utilize SRP (image credit: [3]).

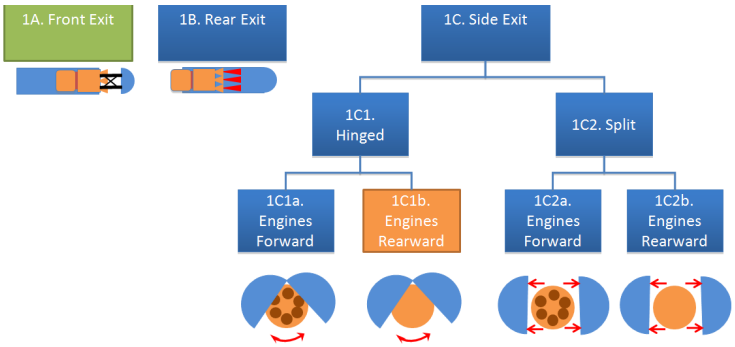

Figure 2.7: Notional transition architectures put forth by the EDLSA for the transition from a ridged hypersonic aeroshell to SRP (image credit: [3]).

only in nature and were not accompanied by any analysis. A set of generic EDL failure modes were developed for the vehicle configuration transition event. The first anticipated failure mode was descent vehicle recontact with jettisoned elements. The notional mitigation strategy for this failure mode was flight testing. The second failure mode was loss of vehicle structural integrity due to pyro shock with the proposed mitigation of using design margins. These top level, notional transition architectures along with the notional failure mode analyses represent the current state-of-the-art for human-scale, supersonic transition analysis available in the literature to date.

2.3 Atmospheric Vehicle Staging Architecture

2.3.1 Subsonic Descent Staging

Atmospheric vehicle staging is a common-place operation in EDL sequencing. Both the Viking and MSL missions utilized in-flight, subsonic vehicle configuration transition to release landers from their protective entry aeroshells prior to touch-down. The most prominent example of subsonic configuration transition is the subsonic heatshield jettison pioneered by the Viking program.

The entry descent and landing concept of operations for the Viking mission is shown in Figure 2.9. After parachute deploy and prior to lander touch down, the hypersonic heatshield is ejected from the backshell using mechanical springs to impart a separation impulse (see Figure 2.8). After the heatshield falls away from the descent vehicle, the lander is released from the backshell,which remains attached to the parachute. After backshell separation, the lander begins propulsive terminal descent to Martian surface. Mission designers were concerned about the potential for jettisoned heatshield recontact with the descent vehicle after separation. To understand these risks, wind tunnel tests were conducted at two Mach numbers to determine the aerodynamic interactions between the heatshield and the backshell during initial subsonic separation [46]. The results of these tests are shown in Figure 2.10. At both Mach 0.55 and 0.95 the drag coefficient on the heatshield remains relatively constant during the separation. The lander/backshell trails the heatshield and is effectively shielded from the free-stream flow during the beginning of the separation event. Consequently, the drag coefficient of the backshell varies significantly during separation. At Mach 0.55, the backshell approaches free-flow drag values at a separation distance of 6 aeroshell diameters. However, as Mach number increases, the interactions from the interference aerodynamics and forebody wake become more significant and the backshell does not approach free-flow drag values until well beyond 6 aeroshell diameters. The results of these wind tunnel tests were used in recontact analyses to determine spring-force require-

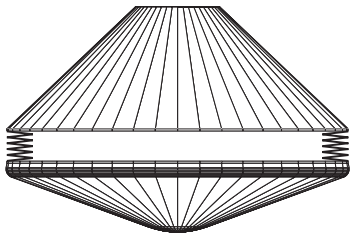

Figure 2.8: Heatshield jettison schematic utilizing mechanical springs for separation impulse (image credit: [47]).

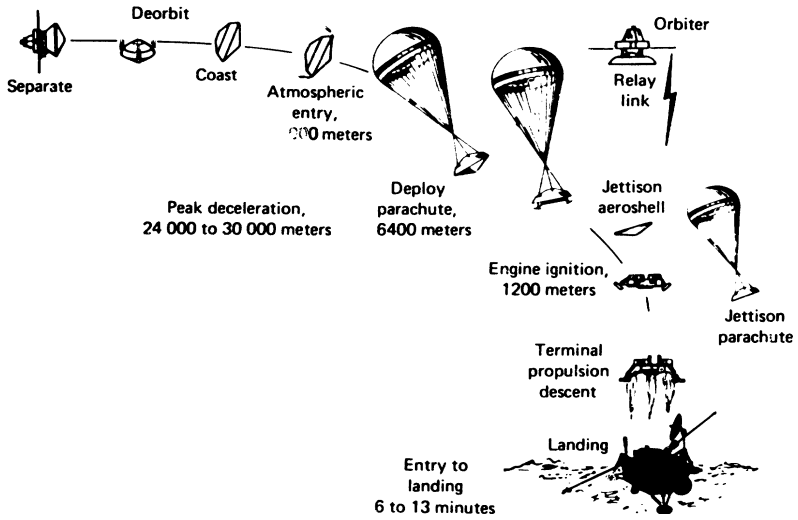

Figure 2.9: Viking EDL concept of operations (image credit: [46]).

ments for the separation systems. It is worthwhile to observe the sequence of analyses performed during the Viking program. Recontact analyses were only performed after the EDL ConOps were set, and after the heatshield and aeroshell were in the final stages of design. The separation analysis does not appear to have been a major driver of initial vehicle requirements. The Viking separation analysis primarily focused on investigating near-field recontact risks. Far-field recontact risks were assumed to be mitigated by a sufficient difference in subsonic ballistic coefficients between the heatshield and the backshell attached to the deployed parachute.

All post-Viking Mars lander missions have utilized the heritage Viking heatshield design, jettison architecture, and separation analysis methodology[47, 48, 49]. Recontact

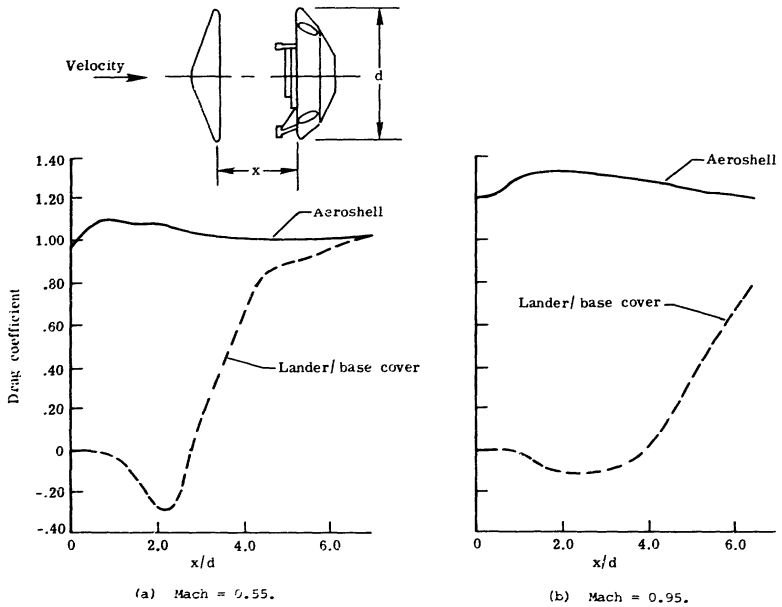

Figure 2.10: Viking wind tunnel separation aerodynamic between the heatshield and backshell (image credit: [46]).

analyses are performed late in the design cycle after many of the lander and system designs are finalized. Far-field recontact risks are assumed to be negligible given sufficient difference in subsonic ballistic coefficients. The near-field separation evaluations look at initial jettison of the heatshield and consider the kinematics of the separation springs and the aerodynamic interference suction phenomenon between the lander and the heatshield. For the MER mission, the heatshield ballast mass was the only control parameter that could be varied during analysis [47]. The MER and MSL missions relied on a brute force methodology to quantify near-field recontact risks. Using the nearly finalized vehicle design, extensive Monte Carlo trajectory simulations varied flight and atmospheric parameters to give a statistical likelihood of recontact and then optimized the ballast mass to minimize those recontact risks.

While subsonic descent vehicle reconfigurations have been flight proven, the same is not true of supersonic descent vehicle reconfigurations. There is a stark absence of research in the literature pertaining to this field. The notional pictograms put forth by the EDLSA represent what appears to be the seminal work in the area to-date for Mars-relevant EDL.

2.3.2 Supersonic Ascent Staging

Supersonic vehicle staging is a familiar operation in the world of ascent vehicles. Examples of supersonic ascent staging include spent booster separations and fairing jettisons. These cases are characterized by large pieces of debris interacting in close proximity to a primary vehicle during supersonic flight. For mission designers, it is of the utmost importance that these discarded pieces of debris do not recontact the vehicle after ejection and cause damage to the primary payload or launch vehicle. The foremost difference between ascent staging and descent staging is the direction of primary vehicle motion relative to ejected debris. In the descent case, the ejected debris falls in the same direction as the primary vehicle travels, where as in the ascent case the debris falls away from the primary vehicle's direction of travel. The difference in direction of motion has far reaching and significant consequences. In the descent scenario, debris ejection becomes a two part problem. In addition to mitigating near-field recontact risks, mission designers must also ensure that ejected pieces of debris do not threaten the primary vehicle at a later point in the descent trajectory or pose a risk to pre-deployed ground assets near the landing zone. While the analysis techniques utilized for supersonic ascent staging do not address far-field recontact risks, these techniques are currently being utilized in industry to analyze supersonic descent staging.

The 1960's and 1970's saw significant effort expended to understand the characteristics and feasibility of supersonic parallel separations of two similar size vehicles. At the time, the state of the art of supersonic separations focused on store separations from aircraft bomb bays [50]. The problem of separating two similar sized vehicles is differentiated from the problem of store separation through the effects of the aerodynamic interactions. In store separation, only the smaller store is affected by the aerodynamic interactions with the larger parent vehicle. When separating two similar sized vehicles, both the main vehicle and the expended vehicle influence each others motion.

Researchers in the 1960's and 1970's sought to understand the unique characteristics of

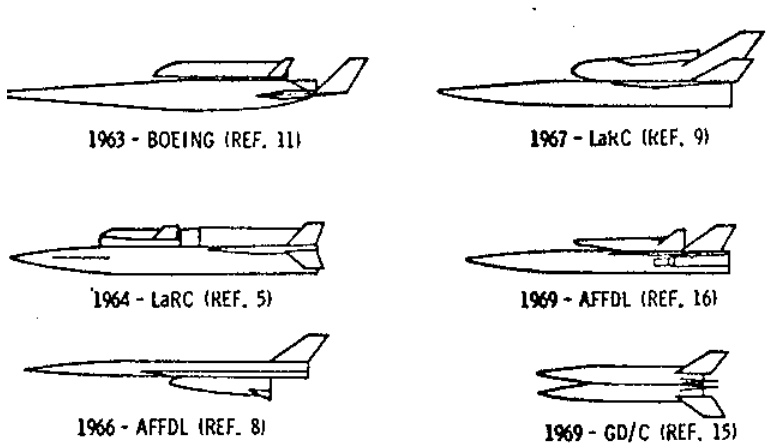

Figure 2.11: Winged body separation configurations studied during the 1960's (image credit: [50]).

separations involving two similar sized vehicles. Early work sought to establish feasibility and develop methods for executing parallel staging separations of the winged body configurations shown in Figure 2.11. Supersonic separations were successfully demonstrated in the mid 1960's when large external propellant tanks were ejected from the X-15A-2 research plane, shown in Figure 2.12. With the advent of the Space Shuttle program, the focus of separation research was redirected toward solving the case of separating spent ascent boosters [50]. Strategies and lessons learned from the X-15A-2 separation formed the foundation of later design efforts of the Space Shuttle booster separations.

The Space Shuttle solid rocket booster (SRB) separation during ascent is the most prominent example of supersonic ascent staging relevant to human Mars supersonic descent staging. Staging for STS-1 occurred at Mach 3.88 and a dynamic pressure of 612 Pa [52]. The DRA5.0 study determined that descent SRP staging would occur at Mach 3.35 and 1290 Pa [2]. The Space Shuttle SRB separation concept of operations is shown in Figure 2.13. The separation is characterized by two solid rocket boosters, of a similar size as the primary vehicle, being jettisoned off each side of the orbiter external tank (OET) via small solid rocket booster separation motors (BSM) located on each SRB.

The Shuttle booster separation was designed using a combination of trial and error and

Figure 2.12: X-15A-2 research airplane (image credit: [51]).

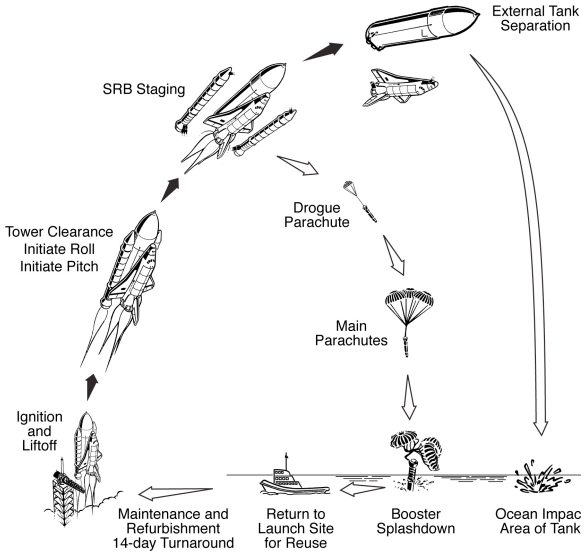

Figure 2.13: Concept of operations for the Space Shuttle SRB separation (image credit: [52]).

brute force testing and simulation. Several early vehicle configurations were tested and analyzed for separation feasibility before settling on the ubiquitous Shuttle configuration we recognize today. Designers of the Shuttle lacked modern computing power and instead utilized extensive wind tunnel testing to determine all interference aerodynamics coefficients. Early investigations were exploratory in nature. Researchers investigated several early shuttle configurations and explored whether separation was feasible, under what conditions separation was feasible, and what physical phenomena were important drivers of the separation behavior [50]. Researchers observed the necessity of using interference aerodynamics in flight simulations. In their simulations, the difference between using interference and non-interference aerodynamics was the difference between a successful separation and a failed separation. Aerodynamic control was also observed to be necessary for many of the early configurations and staging flight conditions.

Extensive wind tunnel testing was used to develop separation interference aerodynamic databases. Due to the coupled motion between the two solid rocket boosters and the orbiter, eight independent variables were considered in the development of the database. To reduce the enormity of a conventional aerodynamic database of eight independent variables, the shuttle program developed the hyper-cube method to reduce the necessary number of data points [52]. The separation system designers noted that obtaining accurate separation aerodynamics were difficult and costly, leading the designers to make simplifications at the cost of accuracy to make the problem tractable [53].

Analysis of the Shuttle separation systems utilized minimum booster separation clearances as the primary evaluation metric of separation success. Boosters were required to maintain minimum clearances from the orbiter and OET at all times during the separation. Rigorous multibody dynamics simulations were performed to look at separation clearances over a variety of worst-case simulation conditions [53]. System designers concluded that a booster separation system could adequately satisfy the minimum clearance success criteria, but possessed several vulnerabilities. Minimum separation clearances would be violated if

the dynamic pressure rose above a specific design threshold. The separation system design was also sensitive to the amount of residual thrust produced by the solid rocket booster at the start of the separation. Higher booster residual thrusts decreased the relative velocity between a booster and the orbiter, causing the objects to remain in close proximity for a longer duration, thereby increasing the recontact risk. The qualification analysis of the Shuttle solid rocket booster separation exemplified the type of rigorous detailed design analysis required for a near final design. The Shuttle separation analysis methodology set the standard for subsequent supersonic ascent separation analyses.

Recent studies have applied the separation methodologies pioneered during the Shuttle program to novel ascent vehicle concepts. Fully reusable, parallel staged, glide back boosters for ascent vehicles have received significant attention since the early 2000's when NASA's Next Generation Launch Technology program identified ascent staging as a critical technology required for development of the next-generation reusable launch vehicles [54]. The Langley Glide Back Booster (LGBB) bimese configuration, shown in Figure 2.14a, is one such concept vehicle that has been the focus of extensive research [54, 55, 56, 57]. The LGBB bimese vehicle consists of two identical vehicles arranged back-to-back. One vehicle serves as the primary ascent vehicle and the other vehicle serves as a booster that is discarded intra-atmospherically after propellant burnout.

An interference aerodynamic database of the LGBB bimese vehicle was developed using 1.75% scale models in the NASA Langley unitary plan wind tunnel (UPWT) at mach 3 and mach 6 [54]. An aerodynamic model was developed from the wind tunnel data using Response Surface Methodology [58]. Through a parallel analysis effort, the supersonic staging separation dynamics were analyzed using two different approaches. The first approach utilized NASA's POST2 trajectory software modified to include a Constraint Force Equation (CFE) methodology to model the vehicle dynamics during the physical separation as well as a short period after physical separation [55]. The second approach utilized the Automatic Dynamic Analysis of Mechanical Systems (ADAMS) solver along with an

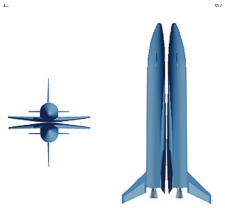

(a) Illustration of the LGBB-bimese vehicle (image credit: [54]).

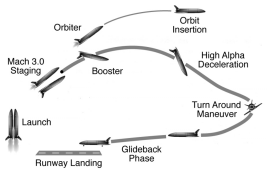

(b) Concept of Operations for the LGBB Mach 3 staging (image credit: [54]).

Figure 2.14: Langley Glide Back Booster (LGBB) bimese vehicle illustration and concept of operations.

in-house Matlab based front- and back-end tool, ConSep, to model the separation event during and for a short time after the two bodies are in contact [54].

The overarching goal of the LGBB separation analysis activity was to assess the feasibility of a pre-defined vehicle configuration to successfully separate over a variety of flight conditions without violating activity constraints. The first constraint specified that the vehicles may not recontact one another after initial mechanical separation and that the discarded booster may not enter the plume of the primary vehicle's engines. The second constraint specified that the angle of attack of both vehicles must remain within the range of the available aerodynamic database, specifically, $0 < \alpha \leq 5.0^{\circ}$ and $0 < \Delta\alpha \leq 5.0^{\circ}$, where α is the angle of attack and $\Delta\alpha$ is the difference in angle of attack between the booster and the primary vehicle.

Using the pre-defined vehicle configuration, the motion of both the primary vehicle and the booster were simulated for 3 seconds, starting from the initial release of the separation mechanism. By simply propagating the vehicles' motion under their passive aerodynamic influences, the vehicles exceeded the aerodynamic database limits on angle of attack. To mitigate this issue, a closed-loop PD controller was implemented to actively control elevon

deflections and keep both vehicles within the angle of attack limits of the aerodynamic database. It was determined that a purely aerodynamic separation was not feasible for the Mach 6 staging, therefore separation thrusters (identical to those used on Shuttle) were used. The boosters produced a combined thrust of 3.33 MN and acted for 0.5 seconds [54]. Performance and mass properties of the separation motors were taken from Space Shuttle data. The separation motors were estimated to weigh 2617 kg or 1.92% of the booster weight at separation.

While the two LGBB analysis activities used different modeling software, both analyses modeled the separation using a methodology similar to the Shuttle program methodology. The analysis methodology applied to the Space Shuttle and the LGBB exemplify the typical approach that has been used to investigate supersonic ascent separations. The analyses start with a pre-defined vehicle configuration, the develop an extensive and expensive interference aerodynamic database, and then perform an intensive investigation of the vehicle dynamics to determine if at any point during the separation the ejected mass recontacts the primary vehicle. If recontact risks exist, the separation system is enhanced with aerodynamic control or separation boosters to make the separation work. The analyses do not consider modifying the separation or vehicle configuration to enable a more favorable passive separation. The analyses are primarily focused on very short time intervals after the separation command is given. The flight dynamics during this time interval are dominated by interference aerodynamics. Because these simulations are for ascent separations, if the ejected mass falls behind the primary vehicle, the separation is considered successful and the simulation ends.

2.4 Interference Aerodynamics

Capturing and characterizing complex interference aerodynamics has proven extremely difficult, time-intensive, and expensive. These efforts have been well documented in previous ascent studies [53, 59, 54, 58].

Early efforts to characterize interference aerodynamics between the Space Shuttle solid rocket boosters (SRB) and the Orbiter and external tank during jettison represent the earliest work relevant to similar-size supersonic ejections. Development of the aerodynamic database was accomplished entirely through rigorous wind tunnel testing [53, 60]. Early investigators quickly understood that the dimensionality of a full interference aerodynamic database made the problem intractable. A schematic of the Space Launch System is shown in Figure 2.15. This vehicle utilizes the same separation architecture as the Space Shuttle. During the ascent supersonic vehicle reconfiguration, both the left and right solid rocket boosters (LSRB and RSRB, respectively) separate from the core stage and fall away from the vehicle. In order to capture the precise dynamic motion of this separation event, a comprehensive interference aerodynamic database with the following list of independent variables would need to be developed (adapted from [59]):

1. Core relative positions of RSRB / LSRB:
   - $\Delta X_{RSRB}, \Delta Y_{RSRB}, \Delta Z_{RSRB}$
   - $\Delta X_{LSRB}, \Delta Y_{LSRB}, \Delta Z_{LSRB}$
2. Core relative euler rotation angles of RSRB / LSRB:
   - $\Delta \Psi_{RSRB}, \Delta \Theta_{RSRB}, \Delta \Phi_{RSRB}$
   - $\Delta \Psi_{LSRB}, \Delta \Theta_{LSRB}, \Delta \Phi_{LSRB}$
3. Core stage orientation: $\alpha_{core}, \beta_{core}$
4. Engine thrust coefficients: $CT_{BSM}, CT_{RSRB}, CT_{LSRB}$
5. Freestream flow conditions: M_∞, q_∞

The size of an interference aerodynamic databases scales exponentially with the number of independent variables. In order to make this problem tractable, Shuttle investigators reduced this list down to eight independent variables through engineering judgment and

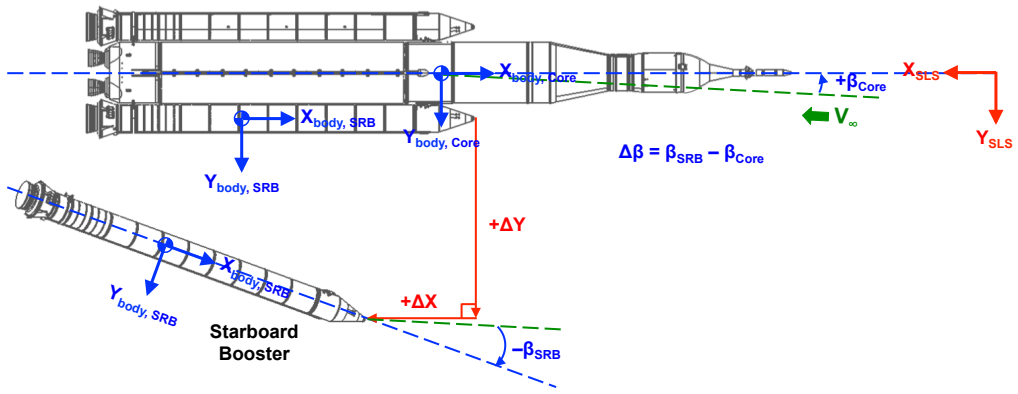

(a) Top view (X-Y plane)

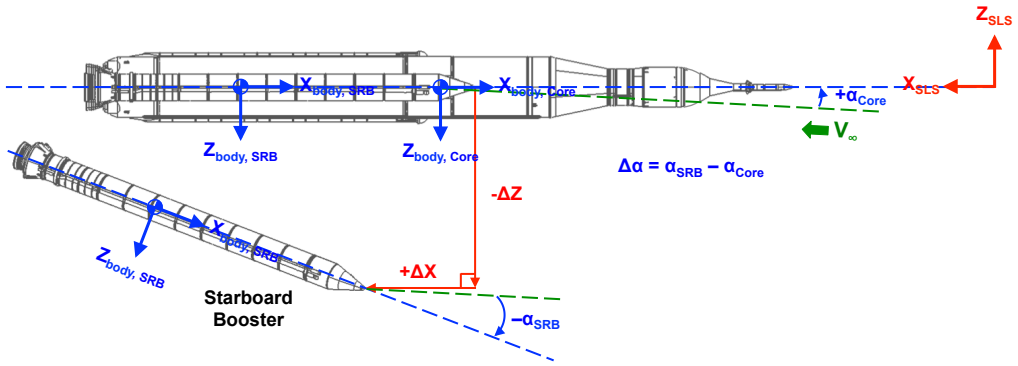

(b) Side view (X-Z plane)

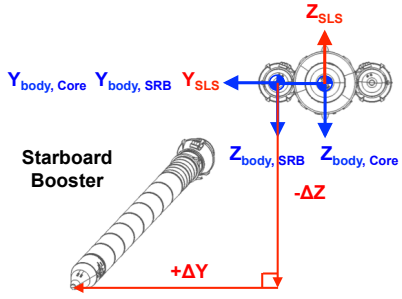

(c) Front view (Y-Z plane)

Figure 2.15: Diagram depicting the physical definition of separation variables for the SLS booster separation (image credit: [59]).

judicious assumptions. The most important of these assumptions were that the boosters separate symmetrically such that values for the independent parameters describing the position and orientation of the LSRB are equal and opposite to corresponding values for the RSRB. Additionally, due to the short time durations of separation maneuvers, Mach number and dynamic pressure were assumed to remain relatively constant.

More recent ascent separation studies have followed the example of the Shuttle program when developing interference databases [58, 54, 59, 61, 62]. The Langley Glide Back Booster (LGBB) bimese vehicle configuration shown in Figure 2.14a was the subject of an extensive interference aerodynamic investigation. The investigation utilized extensive wind tunnel testing to develop the aerodynamic database. Wind tunnel testing was conducted at Mach 3 and Mach 6 in the Langley unitary plan wind tunnel (UPWT). A schematic illustration of the spatial proximity test matrix for the Mach 3 test is shown in Figure 2.16. The test matrix covers a vast spatial area and does not attempt to reduce the size of the matrix by predicting the trajectory of the separating booster. The booster will not pass through a large portion of the spatial test matrix during its separation trajectory. These excess points in the test matrix represent a significant source of inefficient wind tunnel time and computational expense.

Sample schlieren imagery for the Mach 3 test is shown in Figure 2.17. This imagery illustrates the complex shock interactions between supersonic objects in close proximity. Shock waves are discontinuities in a flow across which pressure,temperature, and density change abruptly. When supersonic bodies are in close proximity, shock waves form and reflect back and forth between each body, as can be observed in Figure 2.17. This proximity phenomena drastically increases the complexity and difficulty of modeling the aerodynamics of each body. Investigators of the LGBB utilized Response Surface Methodologies to create analytic models of the LGBB bimese interference aerodynamics using data from the expansive wind tunnel test campaign [54, 58].

The team responsible for developing interference aerodynamic models for the SLS

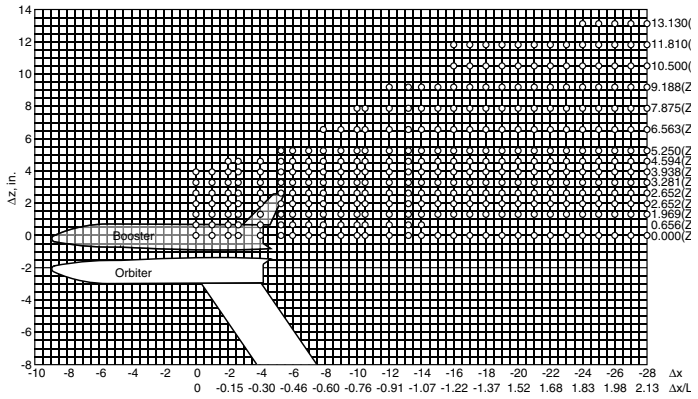

Figure 2.16: Schematic illustration of the spatial proximity test matrix for the LGBB Mach 3 test (image credit: [54]).

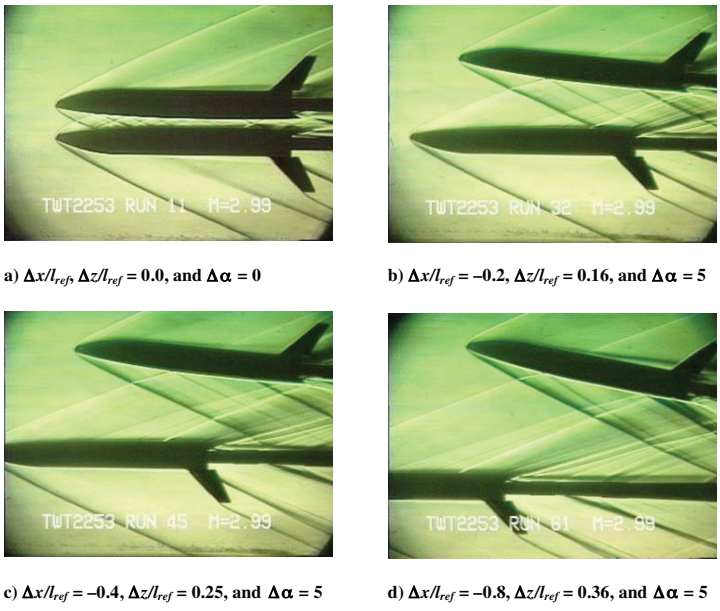

a) $\Delta x/l_{ref}$, $\Delta z/l_{ref}$ **= 0.0, and** $\Delta\alpha$ **= 0**

b) $\Delta x/l_{ref}$ **= –0.2,** $\Delta z/l_{ref}$ **= 0.16, and** $\Delta\alpha$ **= 5**

c) $\Delta x/l_{ref}$ **= –0.4,** $\Delta z/l_{ref}$ **= 0.25, and** $\Delta\alpha$ **= 5**

d) $\Delta x/l_{ref}$ **= –0.8,** $\Delta z/l_{ref}$ **= 0.36, and** $\Delta\alpha$ **= 5**

Figure 2.17: Sample schlieren imagery for the LGBB Mach 3 test illustrates the complex shock interactions between supersonic objects in close proximity (image credit: [54]).

(schematically depicted in Figure 2.15) followed in the footsteps of the Shuttle program. Investigators used a combination of wind tunnel testing, high fidelity viscous CFD, and less computationally intensive inviscid CFD. Due to the high dimensionality of the problem as well as constraints on both time and resources, investigators primarily utilized the Cart3D inviscid CFD solver as opposed to higher fidelity viscous solvers. Due to the shear expansiveness of the required aerodynamic database, it was infeasible to use a viscous solver as the primary CFD tool. As a bench mark, running a single solution with Cart3D using adaptive meshing on 20 CPU's on a single Ivy Bridge node took 1.5 hours [63]. Viscous CFD solvers take orders of magnitude more time. Due to the computational expense of viscous CFD, wind tunnel data and the OVERFLOW viscous flow solver were used in a limited investigation to study complex features inherent to interference flow field and to refine the grid adaptation methods used in the CART3D solver to improve the quality of the results.

In order to reduce the time and resource requirements for developing the aerodynamic database, a rectangular run matrix across all independent variables was not used. Instead, data point placement was guided by previous GN&C trajectory simulations that utilized an earlier version of the aerodynamic database. Data points were spaced along a nominal trajectory and within an envelope of dispersion trajectories about the nominal trajectory. The final database included approximately 2700 data points. The data placement concept is illustrated in Figure 2.18.

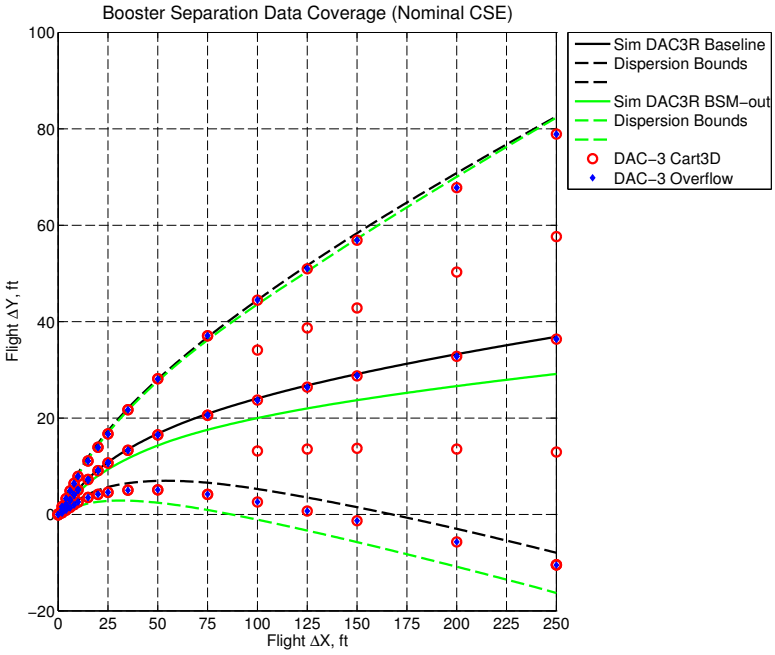

Figure 2.18: Data placement along nominal and dispersion trajectories used for development of SLS interference aerodynamic database (image credit: [59].)

CHAPTER 3
METHODOLOGY TO DETERMINE EJECTION SUBSYSTEM PERFORMANCE REQUIREMENTS TO MITIGATE DESCENT DEBRIS RECONTACT RISKS

3.1 Introduction

Descent supersonic, large-scale debris jettisons, such as aeroshell ejections, have never been performed. NASA's Entry, Descent, and Landing Systems Analysis (EDLSA) identified supersonic aeroshell and aerodynamic decelerator jettisons as potentially mission enabling for Human missions to Mars, particularly for those utilizing supersonic retropropulsion (SRP) [4]. No formalized systems analysis approaches exist to examine the feasibility or mission impacts of performing such a jettison maneuver during a human Mars entry, descent, and landing (EDL) mission. The present work puts forth a methodology to analyze supersonic jettison events during entry, descent, and landing planetary missions. The methodology provides high-level estimates of ejection sub-system performance requirements necessary to successfully achieve a safe debris (aeroshell) separation with respect to far-field recontact risks. Far-field recontact risks are catastrophic collision risks posed by an ejected piece of debris after it has initially been successfully separated. Far-field risks are posed to either the primary vehicle or pre-deployed ground assets near the primary descent vehicle landing site. Risks associated with the process of initially jettisoning debris are termed near-field recontact risks and are not addressed in this analysis.

The methodology utilizes an iterative process between three main analysis modules. Each module may be constructed according to a user-defined set of assumptions. The assumptions associated with a particular module implementation limit the applicability of methodology results in-line with the assumptions made. However, the methodology is deigned with flexibility in mind and can generate results for a variety of user-input module

assumptions. In this way, the final fidelity of the methodology outputs is, to an extent, a user input. The user is required to determine what level of fidelity to trade for ease, speed, and cost of simulation.

This methodology is developed to address a gap in current simulation capabilities to perform high-level, rapid assessment of a multitude of proposed descent vehicle and jettison architectures. It is not intended, nor designed, to perform high-fidelity, low-level, detailed analysis of a specific descent jettison architecture. Rather, it is designed to provide rapid, quantitative data to be used to down-select among many proposed architectures in order to choose a limited set of the most promising architectures on which to perform further detailed, in-depth analysis.

Methodology validation proved challenging. Due to the undeveloped state of the existing research field, there is a lack of relevant data to compare against. Notably, this lack of data stems from supersonic descent separations having never been attempted. Subsonic descent jettisons have been utilized to eject heatshields prior to propulsive terminal descent and lander separation from an aeroshell. These jettison events have primarily been used for robotic landers at Mars. In such missions, no pre-deployed ground assets existed near the landing site. As such, the landing footprint of the debris was not a concern to mission designers. Furthermore, ballistic coefficient differences between the ejected debris and primary descent vehicle were sufficient to ensure no in-flight recontacts following initial separation of the two bodies. Due to these considerations, the primary vehicle was not constrained to avoid flying through the spatial debris field of the jettisoned heatshield. Similarly, supersonic ascent jettisons, such as payload fairing jettisons and solid rocket motor jettisons on ascent vehicles, have the characteristic that the primary vehicle and the jettisoned debris are traveling in opposite directions with respect to the local gravity vector; therefore, far-field recontacts and debris landing footprint have no relevance to mission success. As such, these cases do not produce appropriate validation data for comparison against the present methodology results. In the present study, methodology validation is

addressed through a component-wise module implementation verification approach.

3.2 Separation Architecture and Vehicle Overview

This study leverages the vehicle shape and entry trajectory of Architecture 1 from NASA's Entry, Descent, and Landing Systems Analysis (EDLSA) [4]. Architecture 1 builds on the reference vehicle put forth by NASA's Design Reference Architecture 5.0 (DRA5) [64]. An EDL trajectory profile of Architecture 1 is presented in Figure 3.1 [4]. The 102 mT vehicle enters the Martian atmosphere protected by a 10x30 meter ellipsled aeroshell. It decelerates from hypersonic to supersonic speeds, at which point the aeroshell is shed to reveal the encapsulated descent vehicle. Once the aeroshell sheds, terminal descent initiation begins (see Figure 3.1); the descent vehicle ignites its retropropulsion engines to decelerate to touchdown on the Martian surface.

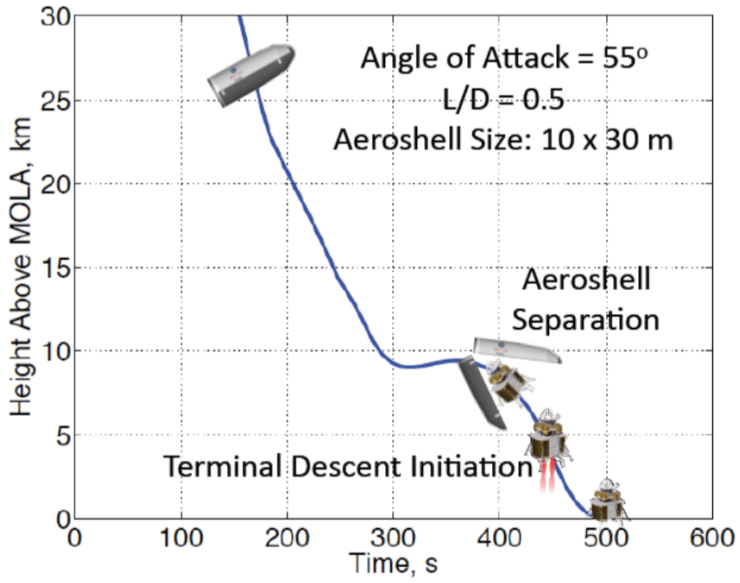

Figure 3.1: Entry, descent, and landing trajectory profile of Architecture 1 from the Entry, Descent, and Landing Systems Analysis [4] study. The entry architecture utilizes a rigid mid lift-to-drag aeroshell for entry followed by supersonic and subsonic retropropulsion to surface touchdown. Prior to supersonic retropropulsion terminal descent initiation, the aeroshell is discarded to release the encapsulated descent vehicle. Not shown is the trajectory impacts of shedding the aeroshell. Image Credit: [4]

The EDLSA proposed a number of possible aeroshell jettison architectures but offered

no supporting numerical analysis to differentiate between the proposed architectures nor did the study perform trajectory analysis to determine mission impacts resulting from performing aeroshell separations. With regard to the primary descent vehicle trajectory, a 20 second no-aerodynamics free-fall was modeled to conservatively estimate impacts of performing an aeroshell jettison. No supporting analysis was performed to validate this assumption as conservative or representative of primary vehicle performance during an aeroshell jettison event. It was chosen solely based on engineering intuition.

The present work examines the hinged-exit separation architecture illustrated in Figure 3.2. The aeroshell opens like a clamshell to reveal the encapsulated primary descent vehicle (PDV). Figure 3.3 illustrates what may happen after the aeroshell halves shed. Assuming the aeroshell halves eventually begin to tumble after jettison, the trajectory of either aeroshell half may follow a multitude of possible trajectories depending on time-of-flight uncertainties in atmospheric properties and the aeroshell flight state immediately following the jettison event. The bounds of the statistical distribution of possible debris trajectories is illustrated by trajectories 2 and 3 in the Figure 3.3. The region between these bounding trajectories is termed the debris field in the present work and identifies a spacial region that is hazardous for the PDV (trajectory 1) to fly through. If the span of the debris field encapsulates any portion of the PDV trajectory, then the debris may pose far-field recontact risks to the PDV. In this situation, a divert maneuver can be used such that the PDV flies entirely outside the debris field. Figure 3.4 illustrates this concept. An offset distance Δ is achieved between the PDV and the debris field. Practically this offset distance is achieved by the debris and/or the PDV performing an active divert maneuver after the aeroshell jettison event such that a safe separation distance is achieved between the PDV and the debris at the point it begins to tumble.

The present study utilizes jettison event initiation flight conditions consistent with the EDLSA [4] stated 3-sigma bounds on altitude, velocity, and flight path angle at jettison. These conditions are reported in Table 3.1. The mass break down of the primary descent

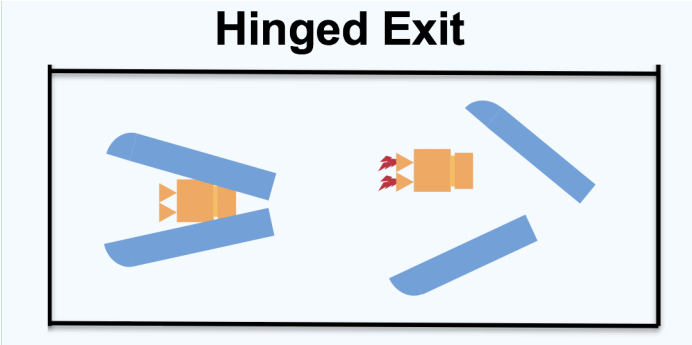

Figure 3.2: Notional illustration of the hinged-exit transition architecture. The aeroshell (blue) is shed to expose the primary descent vehicle (orange) prior to supersonic retro-propulsion initiation.

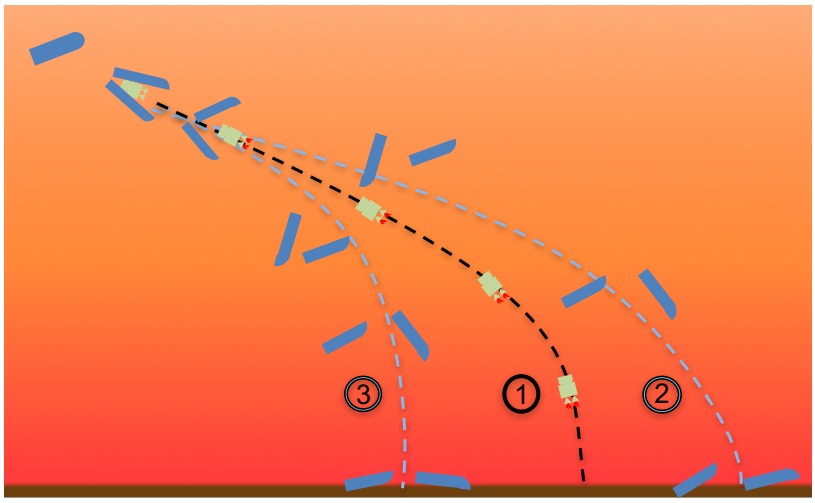

Figure 3.3: Illustration of flight trajectories of debris and a descent vehicle utilizing SRP. The flight envelope of discarded debris may overlap with the primary vehicle trajectory, thus posing recontact risks.

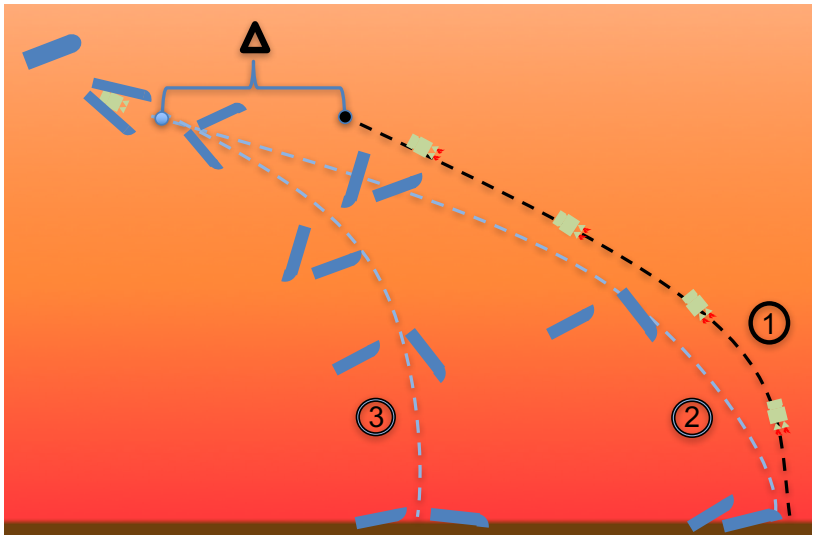

Figure 3.4: Illustration of the concept of initially offsetting (Δ) debris and descent vehicle trajectories such that the descent vehicle does not enter the debris field at any time.

vehicle and the aeroshell is given in Table 3.2. Values are calculated based on data reported in [4]. Inertia properties are calculated based on data from Table 3.2 and approximate CAD models of the descent vehicle and half-aeroshell geometries. Inertia values about body center of gravity are reported in Table 3.3.

Table 3.1: Flight Conditions at Specified Events for 5 Second Transit Trajectory

Event	Velocity, m/s	Flight Path Angle, deg	Altitude, km
EDLSA Transition Initiation	680.0	-10.0	8.8
PDV Propulsive Descent Initiation	675.3	-11.5	8.1

3.3 Methodology Overview

A methodology is presented to analyze supersonic jettison events during entry, descent, and landing planetary missions. Several foundational assumptions are made about the problem structure and its solution during the methodology development and the present example methodology application to the hinged-exit transition architecture. It is assumed that, immediately following separation, the debris will be actively controlled for a short duration of time, after which, the active control will be disabled and the debris will to tumble to

Table 3.2: Vehicle Mass Properties Based on NASA's EDLSA Study [4]

Component	Mass (mT)
Aeroshell, AS	**34.1**
Structure	18.3
TPS	10.6
Entry RCS Dry Mass	5.2
Descent Vehicle, DV	**68.5**
Dry Mass	12.3
Descent Propellant	16.2
Payload	40.0
Total	**102.6**

Table 3.3: Vehicle Inertias about Center of Gravity

Inertia ($kg \cdot m^2$)	Descent Vehicle	Half Aeroshell
I_{xx}	0.8364e6	0.1519e6
I_{yy}	3.9393e6	0.9407e6
I_{zz}	3.9393e6	1.0629e6
I_{xy}	0	0
I_{xz}	0	0.0763e6
I_{yz}	0	0

the surface. The assumption that the debris tumbles is not critical to the structure or function of the methodology. Alternative assumptions could include, but are not limited to, the debris being spin-stabilized or stabilized by a trailing aerodynamic decelerator. The present implementation assumes the debris undergoes six-degree-of-freedom, uncontrolled tumbling.

The span of possible tumbling trajectories forms a debris field. Within this debris field, hazardous recontact risks exist. The methodology assumes the primary vehicle shall be prohibited from flying through this debris field and instead must fly entirely outside of it. This assumption is made for two key reasons. First, a human-mission to Mars will likely have strict safety limits imposed such that there is a high probability of mission success. As such, it assumed that catastrophic far-field recontact risks resulting from the human-payload vehicle flying through an ejected debris field will not be tolerated. Second, human missions will likely required pre-deployed ground assets such as habitats or power-

generation systems near the primary vehicle landing zone. It is assumed catastrophic risks to these assets resulting from falling aeroshell debris will not be tolerated. A possible modification to this assumption, not presently implemented, would instead require the primary vehicle land outside the debris landing footprint. This assumption would minimize risks to pre-deployed ground assets but far-field recontact risks to the primary vehicle would still exist. Far-field recontact risks could then be assessed probabilistically by comparing debris altitude versus time with the primary vehicles altitude versus time to assess the probability of the two bodies being collocated in time and space. This approach would reduce the requirements on the primary vehicle to fly around the entire debris field, possibly resulting in mass or time savings at the expense of increased recontact risks.

The primary vehicle is assumed to fly entirely outside the debris field to avoid possible far-field recontact risks. Two options exist for achieving this offset between the debris field and the primary vehicle. First, the primary vehicle could perform an active divert maneuver. Second, the debris could perform an active divert maneuver. The present implementation of the methodology assumes the latter. The debris is assumed to be actively trimmed at a desired constant angle of attack. Furthermore, thrust can be applied at the center of gravity of the debris if pure aerodynamic control is insufficient to achieve a safe separation distance from the primary vehicle before the debris active control is turned off and it begins to tumble. This choice was made for two reasons. First, active divert maneuvers of a primary vehicle are well studied. As such, their study in the present work would not significantly extend the state of the art of the field. Second, due to the chaotic nature of the interference aerodynamics between the debris and primary vehicle during initial separation, some level of debris active control will likely be required to initially stabilize the debris during near-field separation to prevent catastrophic recontacts. Additionally, active debris control is less well studied than primary vehicle diverts. The present work implements active debris control to perform divert maneuvers in order to advance the state of the art of the field and lay the foundation for future work that optimally combines both divert approaches. It

is worth noting the safe offset distance requirements between the primary vehicle and the debris are identical regardless of which vehicle performs the active divert. If a user chose to implement primary vehicle divert maneuvers, the changes would be contained to a single module of the methodology. The methodology would otherwise continue to function as normal.

The choice of angle of attack and thrust control on the debris is chosen to represent a broad range of possible control strategies. The method of angle of attack control is not specified. It is left to the user to create a model that correlates trim angle of attack with subsystem mass. Such control systems might include aerodynamic flaps or reaction control moment thrusters. The option to have thrust applied at the center of gravity of the debris captures the effects of initial separation subsystems such as separation springs or jettison motors. Additionally, it servers as a slack variable to close the gap on any required offset distance not achieved through pure aerodynamic control. The optimization of the active debris divert maneuver biases toward no thrust solutions and only applies thrust when angle of attack control is insufficient. In this manner, a mission designer is able to see the required supplemental thrust or impulse needed to achieve a safe vehicle reconfiguration using a proposed transition architecture.

Figure 3.5 illustrates the methodology with a flow diagram. Before the methodology can be applied, a full optimized EDL trajectory profile must be provided. A full EDL trajectory is taken to mean an optimized flight trajectory from atmospheric entry all the way to surface touch down. Such a trajectory should indicate the conditions for aeroshell jettison. The present discussion utilized the EDLSA [4] Architecture 1 EDL trajectory depicted in Figure 3.1 with transition initiation conditions reported in Table 3.1. The EDLSA Architecture 1 study assumed a conservative 20 second transition time to allow for aeroshell jettison. The transition event was modeled as an aerodynamics-off free-fall. The study design choice was made to conservatively estimate altitude-velocity performance at the end of the transition event without a complete knowledge or detailed analysis of the transition

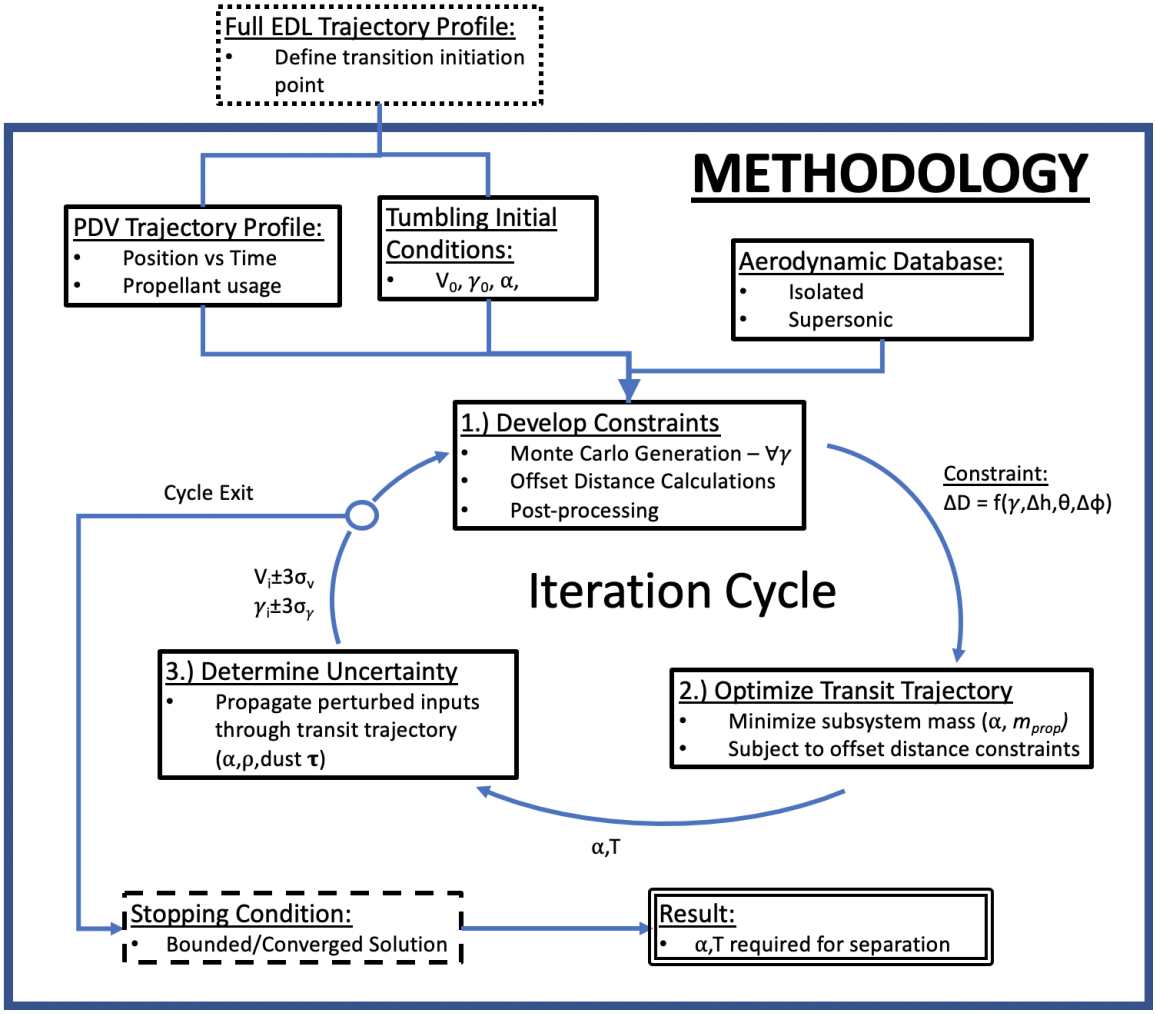

Figure 3.5: Flow chart diagram of major components of methodology.

event. At the time the EDLSA study was performed, this assumption represented the current state-of-the-art in supersonic descent jettison-event flight dynamics analysis. Trajectories are generated using NASA's Program to Optimize Simulated Trajectories (POST2) [65].

3.3.1 Initialization Phase

Before application of the methodology can proceed, the user must have a conceptually well-defined vehicle and transition architecture. Furthermore, vehicle properties defining the transition architecture must be input in a POST2 input deck. These properties include

vehicle masses, inertias, thruster locations, fuel tank locations and masses, and spatial measurements of each solid-mass body and their relative location and orientation among one another. The present work considers the hinged-exit transition architecture shown in Figure 3.2; two aeroshell halves and the primary descent vehicle must be spatially defined with respect to each other at the start of the separation event.

The methodology begins with an initialization phase before the main iteration cycles. Flight conditions for the start of the transition event are taken from the full EDL trajectory previously described. Figure 3.5 identifies this component in the dotted-line box titled "Full EDL Trajectory Profile". The conditions used in the present study are reported in Table 3.1.

Reference primary vehicle terminal descent trajectory profiles must be generated as indicated in Figure 3.5 by the solid-line box titled "PDV Trajectory Profile." In line with the assumptions of the EDLSA study, these are generated by simulating the primary vehicle in no-propulsion, aerodynamic free-fall from the transition initiation start conditions through the full transition time (e.g. 5 s), followed by a propulsion-on terminal descent to the surface. In the present study, propulsive terminal descent follows a pseudo-gravity-turn law in which the applied thrust vector is directed anti-parallel to the vehicle velocity vector and the thrust magnitude is sized to deliver the vehicle 50 meters above the ground with 0 m/s relative velocity. Section 3.4.1 presents terminal descent flight implementation details.

Initial flight state estimates at the start of debris tumbling must be supplied. Figure 3.5 identifies this component in the solid-line box titled "Tumbling Initial Conditions." In the present work, these conditions are roughly approximated to be the same as the flight conditions of the PDV following the no-propulsion, aerodynamic free-fall over the duration of the transition event. Table 3.1 identifies these conditions in the row labeled "PDV Propulsive Descent Initiation". This provides a rough estimate which will be refined by the methodology through successive iteration cycles.

The user must generate or provide aerodynamic databases for the primary vehicle geometry and each debris geometry. In the present implementation, the methodology utilizes

isolated aerodynamics as opposed to interference aerodynamics in order to increase the speed of data acquisition. During the initial jettison of debris, when both bodies are within a spatial proximity on the same order of magnitude as the length of the primary vehicle, interference aerodynamics will likely have a non-negligible effect on debris and primary vehicle dynamics. These effects are not investigated in the present body of work but are mentioned as an item for future development in Section 5.2. The methodology is designed to be flexible to user assumptions and only requires raw aerodynamic coefficient data that spans the flight regimes being investigated. It is left up to the user to determine what assumptions will be made, which aerodynamics tool will be used, and how much fidelity will be sacrificed for speed of acquisition.

In the present work, aerodynamics database are generated using NASA's Cart3D inviscid, Euler solver. Flight regimes encountered in this work range between Mach 2 to 4. During these flight regimes, the slender bodies being investigated can experience both purely isolated flows and near proximity flows with another body. Viscous aerodynamic effects can be important for bodies in near-proximity flows at supersonic speeds. While Cart3D is an inviscid, Euler solver, it has built-in functionality to approximate viscous effects. The task of determining the accuracy and validity of Cart3D aerodynamics over the mid-supersonic flight regime is left to other bodies of work and Cart3D tool developers. Numerous studies provide precedent for utilizing inviscid, Euler solvers (specifically Cart3D) for supersonic ascent booster separation at Earth [66, 59, 67] and supersonic descent at Mars [4]. These studies encounter similar flight regimes as the present work and evaluate the efficacy of utilizing inviscid aerodynamics where viscous aerodynamics might be more appropriate. The present study makes no attempt to quantify the error or effect of this assumption.

3.3.2 Develop Constraints

With the initialization phase complete, the main iteration cycle begins. The first module of the methodology iteration cycle, titled "Develop Constraints" (Figure 3.5), produces a database of required offset distances as a function of debris flight parameters for use in subsequent debris-divert trajectory optimization modules. The database is a function of instantaneous altitude separation distance between the primary vehicle and debris, difference in azimuth angles, the flight path angle of the debris, and a clock angle (defined in Section 3.4.3). The details of generating the offset distance constraint databases are presented in Section 3.4.3.

3.3.3 Optimize Transit Trajectory

The next module, Optimize Transit Trajectory, takes in the offset distance constraint databases from the previous module and produces an optimized debris transit trajectory. Trajectory optimization modulates both debris angle of attack and thrust applied through the center of gravity. The optimization algorithm first attempts to determine a debris angle of attack such that the debris satisfies minimum offset distance constraints at the end of the transit trajectory duration. If aerodynamic control alone is insufficient to achieve required offset separation distances, the optimization algorithm applies thrust at the center of gravity of the debris to provide enough delta-V to meet offset distance requirements. The thrust is applied in the vehicle pitching plane such that it is normal to the velocity vector and drives the debris away from the primary descent vehicle. Details pertaining to this module are presented in Section 3.5.

3.3.4 Determine Uncertainty

The final analysis module in the methodology iteration cycle, Determine Uncertainty, applies perturbations to the initial state of the optimized transit trajectory from the previous module to produce dispersions on the trajectory end-state. Three-sigma input dispersions

are applied to angle of attack, atmospheric density profile, and atmospheric dust content. It is assumed 3-sigma dispersions on input parameters produce 3-sigma dispersions on trajectory end-states. Nominal and 3-sigma distributions of end-state velocity and flight path angle feed back into the first module, Develop Constraints, to start the next iteration cycle in which new offset distance constraint databases are generated and a new transit trajectory is optimized. Details pertaining to this module are presented in Section 3.6.

3.3.5 Stopping Condition and Outputs

The methodology iteration cycles terminate when the stopping condition is met. The stopping condition dictates that successive iteration solutions for minimum required angle of attack, terminal transit trajectory velocity, and flight path are either asymptotically converged or bounded. In the present work, the optimization space proved too non-linear and stiff to produce asymptotically converged solutions, so iteration cycles terminate when solutions become bounded converged. Primary results of this methodology are the debris angle of attack and center of gravity thrust required to achieve minimum offset distances such that debris recontact risk with the primary vehicle is reduced to the user-defined confidence level. It is assumed these parameters correlate to ejection subsystem mass and thereby provide a relative estimate of ejection subsystem mass requirements. Each result is specific to the vehicle architecture and separation architecture studied and limited by the assumptions made by the user within each module.

3.4 Determination of Required Offset Distances

The first module in the methodology iteration cycle depicted in Figure 3.5 is the development of minimum offset distance constraint databases. Constraints specify minimum altitude-normal-planar offset distances between the PDV and the ejected debris at the end of a specified transition time such that the trajectories of the PDV and the debris do not intersect (see Figure 3.4). See Section 3.3 for the rational behind this requirement. Trajec-

tories are generated using NASA's Program to Optimize Simulated Trajectories (POST2) [65]. Offset distances are computed in the cross-track plane where the plane normal vector is aligned with the altitude dimension. The no-overlap requirement ensures the ejected aeroshell does not pose catastrophic recontact risks to the PDV or pre-deployed ground assets at the PDV landing site.

3.4.1 Simulation of Primary Vehicle Propulsive Descent Trajectory

The primary vehicle propulsive descent trajectory is modeled consistent with NASA's Entry, Descent, and Landing Systems Analysis (EDLSA) study. The initial flight conditions at the start of the transition event are taken from the EDLSA study and reported in Table 3.1. Descent propulsion initiation begins after a pre-specified duration, called the transition time, following the onset of the transition event (see Figure 3.1). During the transition time, the primary vehicle and ejected debris are separated from one another and actively maneuvered away from each other to avoid recontact risks. The EDLSA study used a conservative 20 second transition time due to lack of knowledge of the transition event and its impacts on the overall mission trajectory. For the purposes of this discussion, a transition time of 5 seconds is used. Flight conditions at the start of propulsion initiation are determined by simulating the motion of the PDV from the start of the transition event through the duration of the transition time. These flight conditions are reported in Table 3.1. The propulsive descent phase of flight is modeled using a gravity turn inspired propulsive control scheme. The thrust vector is required to be anti-parallel to the descent vehicle planet-relative velocity vector. The thrust magnitude is sized such that the PDV arrives at 50 meters altitude with zero relative velocity. Alternative control schemes could be implemented within the methodology without compromising the methodology structure or functionality.

Table 3.4: Propulsive Descent Parameters

Parameter	Value
Transit Time, s	5
Terminal Altitude, m	50
Terminal Velocity, m/s	0
Thrust Magnitude, MN	1.047
Thrust Duration, s	44.6
Propellant Used, mT	13.4

3.4.2 Development of Debris Field

A debris field is defined as the cumulative spatial volume through which multiple, simulated debris trajectories may pass for a specified distribution of initial trajectory parameters and randomized perturbations during flight. In the present implementation, debris is assumed to undergo six degree-off-freedom tumbling within the debris field. The methodology can accommodate a wide-variety of user assumptions about the motion of the debris within the debris field. Examples of alternative debris motion assumptions include spin-stabilization or trailing inflatable aerodynamic decelerator stabilization.

In the present study, debris fields are generated through Monte Carlo simulations of a jettisoned semi-aeroshell during a controls-off terminal flight segment. The discarded debris is assumed to be actively controlled immediately following separation from the primary body until a safe relative proximity distance is achieved, at which point active controls are turned off and the debris tumbles to the planet surface. Active controls are assumed to include some combination of aerodynamic trim flaps, reaction control system attitude thrusters, or thrust applied through the center of gravity of the debris. Monte Carlo simulations of the debris field focus on the tumbling segment of flight. Figure 3.6 depicts 20 tumbling trajectories sampled from a full Monte Carlo simulation of 8001 cases. These trajectories span a range of altitude-downrange-crossrange space. The combined span of all Monte Carlo trajectories constitutes the debris field.

Initial parameters perturbed within the tumbling debris Monte Carlo simulation are

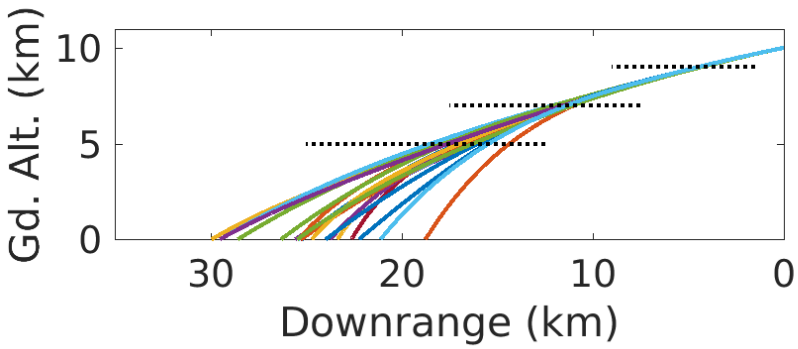

Figure 3.6: A collection of 20 tumbling trajectories from a Monte Carlo run of 8000 trajectories. The constant-altitude lines (dotted) indicate how a constant altitude slice is taken across all tumbling trajectories in a Monte Carlo run.

listed in Table 3.5. These parameters were chosen based on recommendations from NASA Langley engineers who have performed Monte Carlo analysis for robotic Mars lander flight missions. This list of parameters, though not exhaustive, is believed to capture most of variability of the debris initial state at the onset of tumbling. The effects of initial parameters not included in Table 3.5 could increase the scatter of tumbling trajectories, though these uncertainties are assumed to be negligible.

Table 3.5: Parameters Perturbed During Monte Carlo Simulations

Parameter
Velocity, m/s
Flight Path Angle, deg
Azimuth Angle, deg
Angle of Attack, deg
Sideslip Angle, deg
Bank Angle, deg
Pitch Rate, deg/s
Roll Rate, deg/s
Yaw Rate, deg/s
Mass Multiplier
Drag Coefficient
Lift Coefficient
Atmospheric Density Profile

The flight conditions at the beginning of the Monte Carlo simulation depend on the transit trajectory profile of the debris during the transition time window. Nominal flight

conditions used in the present discussion and their associated 3-sigma normal dispersions are presented in Table 3.6. Within the context of the methodology, nominal values and associated dispersions are determined from the previous modules within the Iteration Cycle: Optimize Transit Trajectory and Determine Uncertainty. The present discussion uses approximate values well suited for exposition of the underlying processes and analysis.

Two Monte-Carlo simulations were run for the purposes of this discussion: a reference simulation and a comparison simulation with a modified nominal initial flight path angle to be used to illuminate the effects of changing parameters. The Monte Carlo simulations are run from an initial altitude of 10km. This is notably higher than the altitude at the start of the transition event reported in Table 3.1. The motivation for this higher altitude stems from post-processing considerations and is discussed in Section 3.4.3.

Table 3.6: Flight Conditions at Monte Carlo Origin with 3-Sigma State Dispersions

Simulation	Flight Path Angle, $\deg$	Velocity, m/s	Altitude, km
Reference	-17.0 +/- 2.0	635.0 +/- 5.0	10 +/- 0
Modified Flight Path Angle	-10.0 +/- 2.0	635.0 +/- 5.0	10 +/- 0

A number of modeling assumptions are made in order to represent the collection of tumbling trajectories as a structure in space with defined bounds in latitude and longitude as a function of altitude. The following discussion provides details of the approach used to achieve this representation. A discussion of the assumptions inherent to this approach follows the overview.

The horizontal dotted lines in Figure 3.6 identify constant-altitude slices that intersect all Monte Carlo trajectories at a given altitude. The intersection between a constant-altitude slice and all Monte Carlo trajectories forms a constant-altitude point cloud, depicted in Figure 3.7. Constant-altitude slices are taken at increments of 10% of the initial tumbling altitude to form 10 constant-altitude point clouds as shown in Figure 3.8. A bounding ellipse is fit around each constant-altitude point cloud such that the ellipse is centered at the mean of all points in the point cloud and sized such that 95% of all points are contained within the

ellipse. This bounding ellipse determination approach is not guaranteed to produce a minimum size ellipse containing the desired percentage of points. The user is free to implement any algorithm of choice to determine ellipses. Figure 3.7 shows a 95% bounding ellipse fit to one point cloud. Bounding ellipses are fit to all constant-altitude point clouds. Together, the ellipses define the spacial structure of the debris field as shown in Figure 3.9. The coordinate system shown in Figure 3.9 is a Cartesian Mars-centered-rotating frame where the altitude dimension is identified by the normal vector to the set of altitude ellipses.

There are perhaps better techniques for representing the debris field structure in longitude and latitude space as a function of altitude. The approach used here was determined through repeated experimentation and found to be relatively computationally inexpensive. The present implementation suffers from discretization of the altitude space as well as non-minimum size bounding ellipses. Better approaches might consider a more rigorous mathematical approach to represent a smooth and continuous three-dimensional structure that minimally bounds the debris field trajectories.

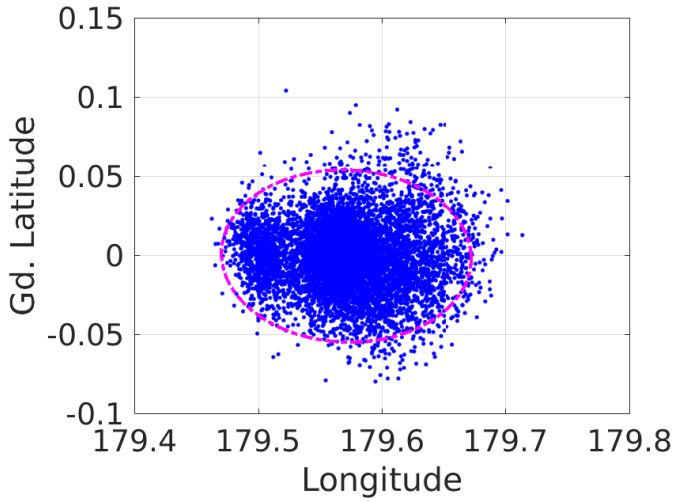

Figure 3.7: A single altitude-slice point cloud is encircled by a 95% bounding ellipse. The ellipse is centered at the mean of the point cloud and sized to encapsulate 95% of points. The figure view is aligned with the altitude dimension.

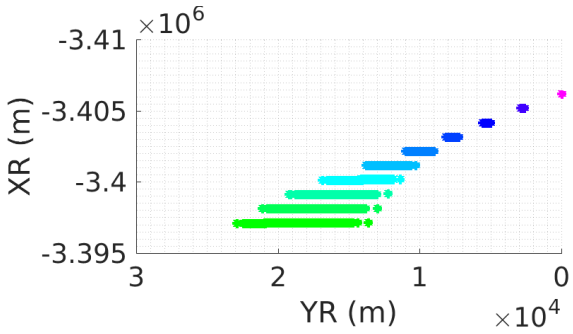

(a) View aligned with crossrange dimension showing altitude and downrange in Cartesian Mars-Centered Rotating frame.

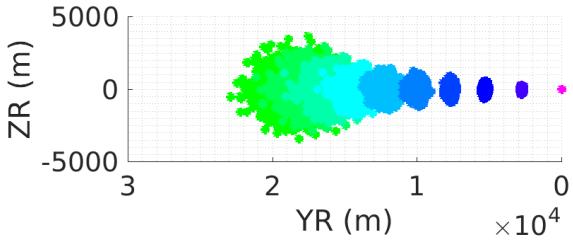

(b) View aligned with altitude dimension showing crossrange and downrange in Cartesian Mars-Centered Rotating frame.

Figure 3.8: Constant altitude slices of all trajectories from a Monte Carlo simulation of tumbling debris. Each point represents the intersection of a single trajectory with a specific altitude. Each trajectory will have a point plotted for each altitude slice.

3.4.3 Computation of Offset Distance

Required altitude-normal-planar offset distances are determined by comparing the bounding-ellipse structure that defines the spatial location of the hazardous debris field with the spatial location of the PDV propulsive descent trajectory (solid black line in Figure 3.9). Offset distances between the origins of both the PDV and debris tumbling trajectories are computed such that the PDV trajectory does not intersect the debris field at any location in space. The computation routines that compute offset distance require both structures initially be co-located in latitude and longitude space to establish a reference position from which minimum required offset distances are reported. The computation of offset distances inherently assumes the PDV is prohibited from flying through the debris field and instead must fly around it. See the discussion in Section 3.3 for more details regarding this assumption.

Overshoot and undershoot offset distances are signified in Figure 3.9 by black dashed and dotted lines, respectively. Overshoot is defined as an offset in which the PDV trajectory flies in front of the debris field; the forward direction is defined to be aligned with the azimuth direction of the initial PDV velocity vector. Similarly, an undershoot offset results in the PDV flying behind the debris field. Offset distances are calculated as the minimum altitude-normal-planar translation required such that the PDV does not pass within any altitude bounding ellipse. Required offset distances are highly dependent on the geometry of the PDV trajectory and the size and orientation of each altitude ellipse in the the debris field. The initial flight parameters used to generate Figure 3.9 are reported in Table 3.7. In this example, an overshoot offset of 4.65 km and undershoot of -4.39 km is required to avoid intersection between the PDV and debris field. The undershoot offset in Figure 3.9c is driven by the PDV intersection with the ground-level bounding ellipse where as the overshoot is driven by the highest bounding ellipse. The specific bounding ellipse driving an offset distance may change with changes in the structure or azimuth angle of the PDV trajectory (or debris field).

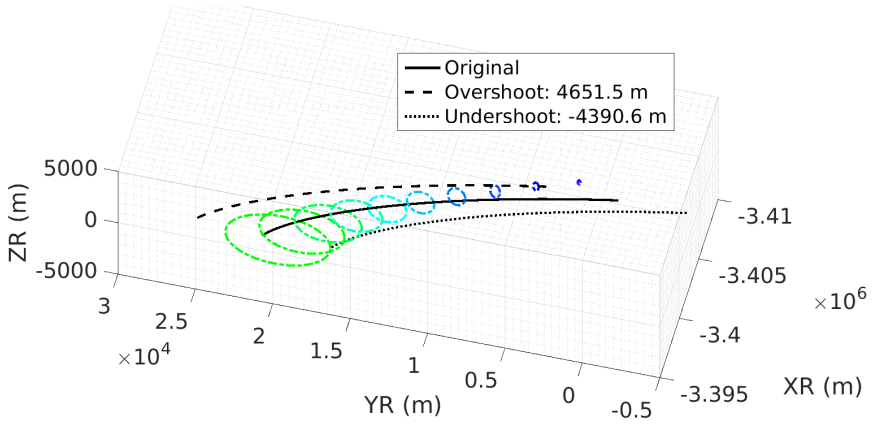

(a) Isometric view showing altitude, crossrange, and downrange in Cartesian Mars-Centered Rotating frame.

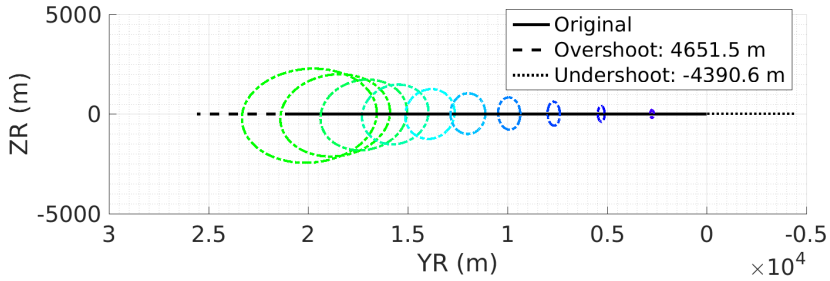

(b) View aligned with altitude dimension showing crossrange and downrange in Cartesian Mars-Centered Rotating frame.

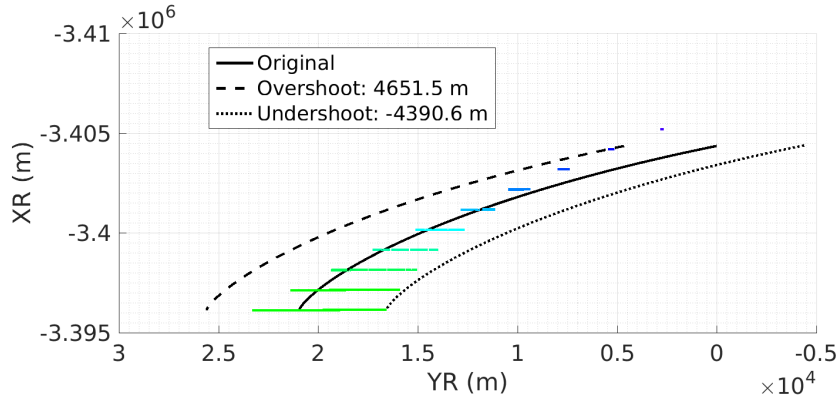

(c) View aligned with crossrange dimension showing altitude and downrange in Cartesian Mars-Centered Rotating frame.

Figure 3.9: Illustration of the intersection between the debris field (stacked ellipses) and PDV propulsive descent trajectory (solid). Overshoot (dashed) and undershoot (dotted) PDV trajectories are also depicted.

Table 3.7: Initial Conditions at the Beginning of Flight

Parameter	Debris Field	PDV Propulsive Descent Trajectory
Initial Altitude, km	10	8.1
Latitude, deg	0	0
Longitude, deg	180	180
Azimuth, deg	270	270

Offset distances are measured relative to the initial latitude and longitude of the debris field origin. Databases of required offset distances are generated for variations in nominal initial flight path angle (gamma) of the tumbling debris, initial altitude difference, and mean initial azimuth angle difference between the PDV and the debris field origins. The fourth dimension of the constraint databases is a clock angle (theta) about the altitude spatial dimension that modifies the reference overshoot direction. These four parameters were determined through investigation to be the key driving parameters in capturing the variability of offset distance as a function of the relative states between the debris and PDV. Initial velocity of the tumbling debris is not included in the database in order to reduce the number of Monte Carlo simulations that must be performed for each iteration of the methodology. Instead, initial debris velocity is handled as an iteration hand-off variable that is only updated once per methodology iteration. The methodology can accommodate additional parameters in the database as long as the end result is a database that can be queried for required offset distance. The addition of extra database parameters will result in increased simulation times.

Figure 3.10 illustrates a 45° theta angle modifying the overshoot reference direction as compared to Figure 3.9. Figure 3.9 illustrates a planar-downrange offset maneuver. The inclusion of a theta angle in the simulation enables analysis of crossrange offset maneuvers. As seen in Figure 3.10, overshoot and undershoot offsets translate the PDV trajectory out of the original PDV plane-of-motion due to the theta angle. In this example, required overshoot and undershoot offsets for a 45° theta angle are 2.34 km and -3.07 km, respectively. Initial conditions for this simulation are identical to those of Figure 3.9 and reported

in Table 3.7.

Figure 3.11 shows offset distances calculated for a 3° difference in azimuth angle between the PDV trajectory and debris field nominal initial velocity vector. Initial conditions for this simulation are reported in Table 3.7. In this example, applying an angle Phi (azimuth angle difference) affects a reduction in the magnitude of required overshoot and undershoot offset distances to 4.54 km and -3.85 km, respectively.

The offset distance database incorporates a range of Monte Carlo debris field nominal initial flight path angles. The previous dimensions of the database (altitude difference, theta, phi) are populated using post-processing analysis of the debris field and the PDV trajectory. Populating the database with a range of initial flight path angles requires generating a new debris field for each flight path angle. Figure 3.12 shows required offset distances for a debris field with a -10° nominal flight path angle. Initial conditions for this modified simulation are reported in Table 3.6 beneath nominal simulation conditions. The effect of the smaller flight path angle on the volume of the debris field is an overall expansion and stretch in the downrange and crossrange directions resulting in an enlarged ground footprint. This expansion is further visible in the difference between required overshoot and undershoot offset distances of 12.9 km and -10.1 km, respectively.

For all variations in clock angle, azimuth angle, and flight path angle, offset distances are calculated across a range of debris field origin altitudes. All previous debris fields presented in this discussion are displayed starting from an altitude of 10km, including Figures 3.6, 3.8, 3.9, 3.10, 3.11, and 3.12. Each debris field Monte Carlo is simulated from an initial altitude of 10km and recursively translated downward in post-processing. At each altitude translation increment, overshoot and undershoot offsets are recalculated.

The collection of offset distances versus altitude for a single setting of azimuth angle, clock angle, and flight path angle is shown in Figure 3.13. Two subplots are shown, each with trend lines for overshoot and undershoot offset distances. The top subplot shows the initial altitude at the onset of debris tumbling along the dependent axis. The nominal alti-

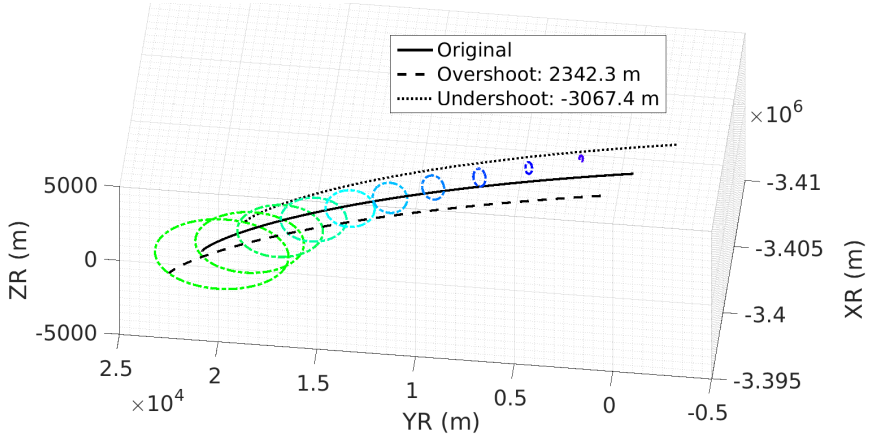

(a) Isometric view showing altitude, crossrange, and downrange in Cartesian Mars-Centered Rotating frame.

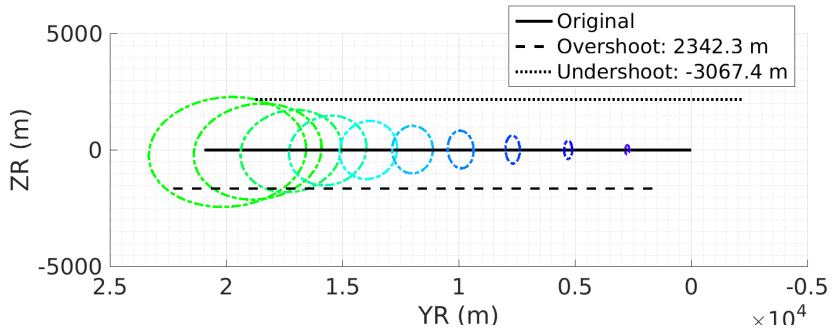

(b) View aligned with altitude dimension showing crossrange and downrange in Cartesian Mars-Centered Rotating frame.

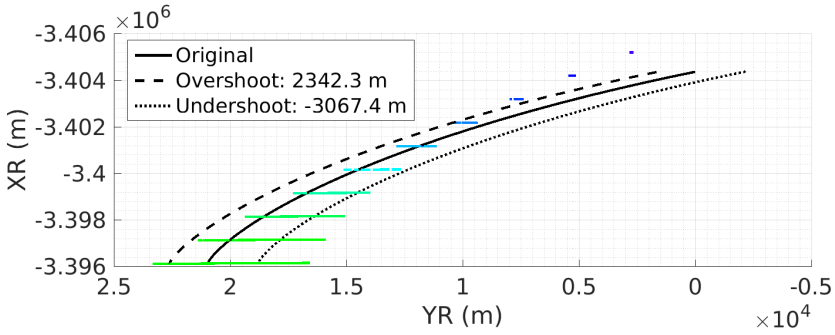

(c) View aligned with crossrange dimension showing altitude and downrange in Cartesian Mars-Centered Rotating frame.

Figure 3.10: This Figure is analogous to Figure 3.9 except a clock angle (theta) modifies the overshoot and undershoot reference directions. The debris field (stacked ellipses), PDV propulsive descent trajectory (solid line), PDV Overshoot (dashed line), and PDV undershoot (dotted line) trajectories are depicted. Figure 3.10b shows a top-down view of the debris field. In this example, a 45° theta angle modifies the overshoot direction as shown.

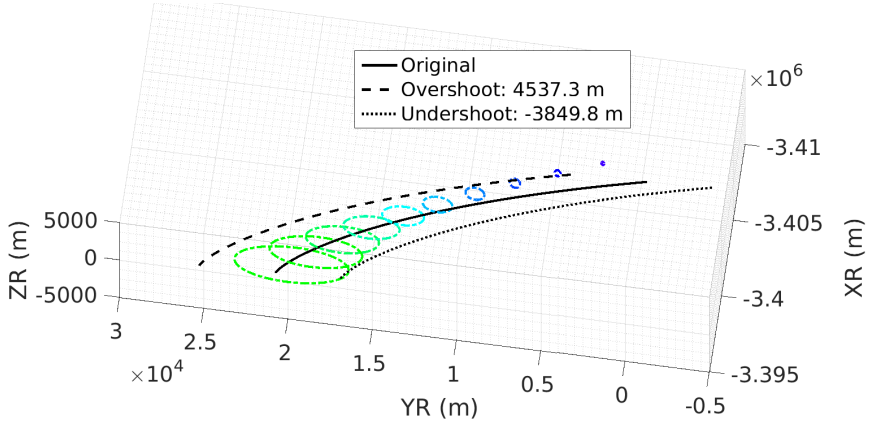

(a) Isometric view showing altitude, crossrange, and downrange in Cartesian Mars-Centered Rotating frame.

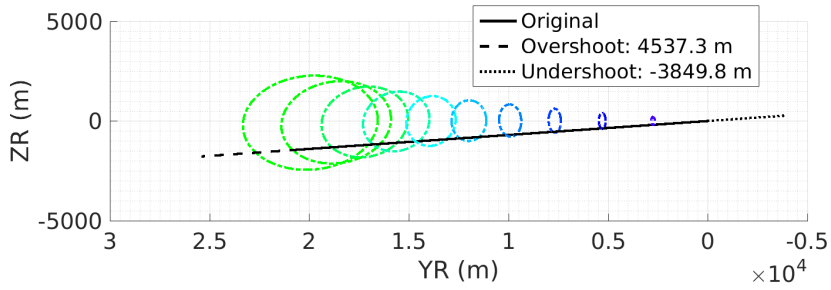

(b) View aligned with altitude dimension showing crossrange and downrange in Cartesian Mars-Centered Rotating frame.

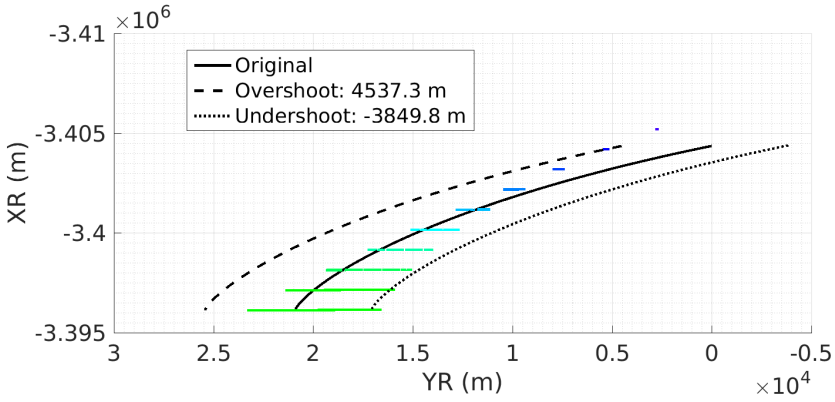

(c) View aligned with crossrange dimension showing altitude and downrange in Cartesian Mars-Centered Rotating frame.

Figure 3.11: Illustration of an applied 3° azimuth angle difference (phi) applied between the debris field and the PDV trajectory. The debris field (stacked ellipses), PDV propulsive descent trajectory (solid line), PDV Overshoot (dashed line), and PDV undershoot (dotted line) trajectories are depicted.

tude identified in the figure is defined as the origin altitude of the PDV propulsive descent trajectory; in this example, that altitude is 8.17 km. The bottom subplot mirrors the top subplot but references the delta altitude increment along the dependent axis. The delta altitude increment is defined as the nominal PDV origin altitude less the post-processed debris field origin altitude.

The process of translating the debris field origin altitude lower results in the sequential elimination of the lowest constant-altitude bounding ellipses from the computation of offset distance when the translated altitude of an ellipse falls below the lowest altitude of the PDV trajectory profile (0 km). Once a constant altitude ellipse falls below this threshold, the post-processing routines no longer consider potential interactions between the PDV trajectory and this cropped debris field volume. This process affects a reduction in the ground footprint and volume of the debris field as the entire debris field is translated downward in altitude. Section 3.10.3 details an activity that explores the validity of this assumption. Namely, that the debris field can be recursively translated lower in altitude in post-processing to accurately represent the debris field of debris that begins tumbling at lower altitudes. When the required overshoot offset distance is less than 0, there is no risk of recontact between the ejected debris and the PDV or any pre-deployed ground assets. Similarly, there is no risk of recontact when the required undershoot distance is greater than 0.

3.5 Transit Trajectory Optimization

The second module in Figure 3.5 is Optimize Transit Trajectory. Trajectory optimization is performed with NASA's POST2 using Standford's NPSOL optimization algorithm [68]. In the present study, optimization routines minimize angle of attack and center of gravity thrust such that minimum offset distance constraints are satisfied to ensure debris does not pose far-field recontact risks to the primary vehicle or pre-deployed ground assets. For explanation on the modeling assumptions and choices that go into transit trajectory

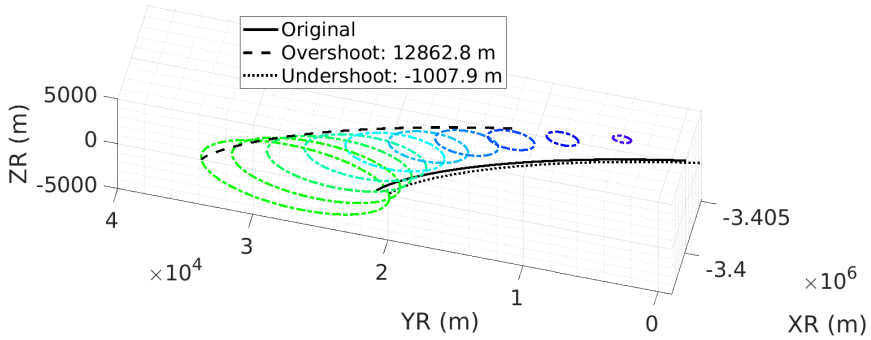

(a) Isometric view showing altitude, crossrange, and downrange in Cartesian Mars-Centered Rotating frame.

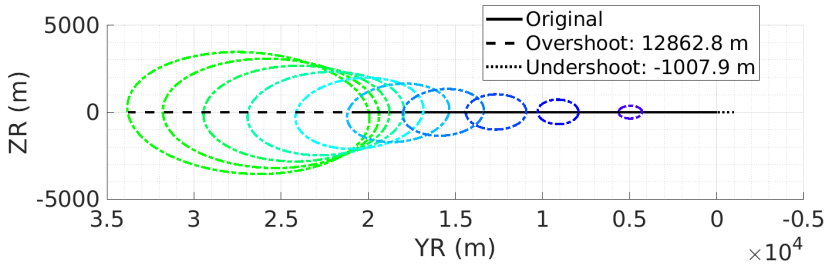

(b) View aligned with altitude dimension showing crossrange and downrange in Cartesian Mars-Centered Rotating frame.

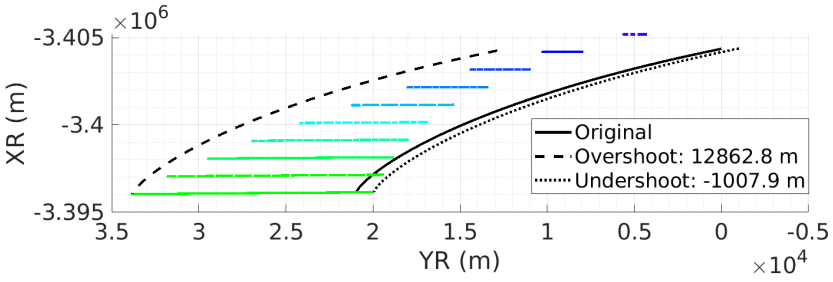

(c) View aligned with crossrange dimension showing altitude and downrange in Cartesian Mars-Centered Rotating frame.

Figure 3.12: Illustration of a modified Monte Carlo nominal flight path angle (gamma). As compared to the simulation depicted in Figure 3.9, the ground footprint size of the debris field has increased and shifted out in the downrange direction. This shift resulted in an increased required overshoot offset distance. The debris field (stacked ellipses), PDV propulsive descent trajectory (solid line), PDV Overshoot (dashed line), and PDV undershoot (dotted line) trajectories are depicted.

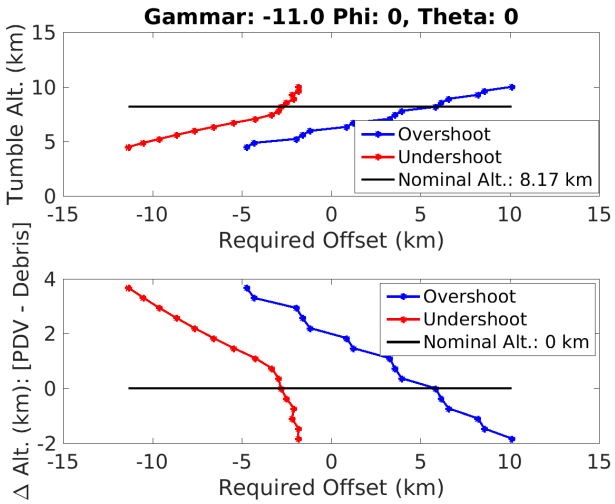

Figure 3.13: Overshoot and undershoot offset distances versus altitude for a single setting of azimuth angle, clock angle, and flight path angle. The top subplot shows the initial altitude at the onset of debris tumbling along the vertical axis. The bottom subplot mirrors the top subplot but references the delta altitude increment along the vertical axis. The delta altitude increment is defined as the nominal PDV origin altitude less the post-processed debris field origin altitude.

optimization, see Section 3.3.

The relative motion between a jettisoned aeroshell debris (red line) and the primary descent vehicle (blue line) of an optimized transit trajectory is shown in Figure 3.14. This transit trajectory has a duration of 5 seconds, a separation bank angle of 135 degrees, and is optimized to an angle of attack of 31.1 degrees. Use of the methodology showed pure angle of attack modulation for control is sufficient to satisfy minimum offset distance constraints and center of gravity thrust is not necessary. The solid blue line is the PDV trajectory. The solid red line is the optimized debris transit trajectory. The solid black line shows the reference downrange direction, which is defined as positive and increasing in the direction of travel of the PDV trajectory. Note, this simulation assumes the motion of the PDV is constrained to altitude-downrange space; therefore, the PDV heading and reference downrange direction are always aligned.

Parameters used to query constraint databases to determine required offset distances at any instantaneous flight condition are illustrated in Figure 3.14. The short-dashed black

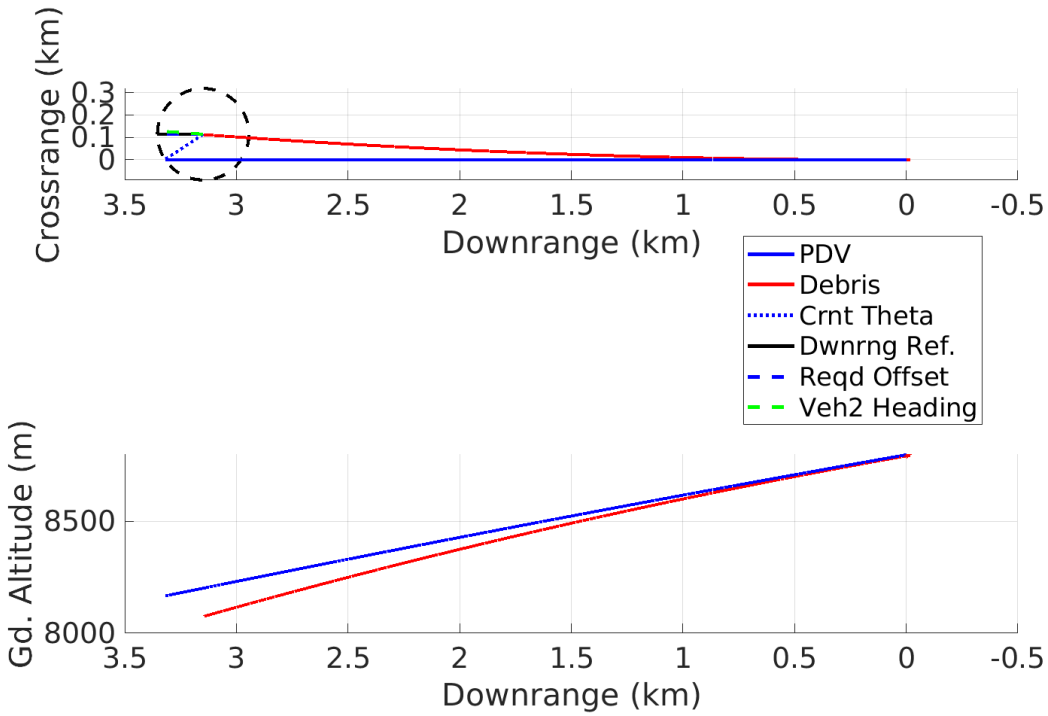

Figure 3.14: Overview of an optimized 5 second transit trajectory. Parameters relevant to the optimization process are shown, including the terminal clock angle, theta, and terminal required offset distance.

line connects the debris and PDV terminal trajectory points; the angle this line makes with the reference downrange direction is the clock angle, theta. The clock angle indicates the heading toward the PDV as viewed by the debris. The dashed green line shows the terminal azimuth heading of the debris. The angle between this line and the reference downrange direction gives the terminal azimuth angle difference between the debris and PDV. The altitude difference and debris terminal flight path angle complete the set of look up parameters used to determine instantaneous required offset distances. The long-dashed black circle is centered at the debris terminal state and visualizes the required offset distance between the PDV and debris. The offset distance constraint is satisfied when the terminal PDV state is on or outside of the long-dashed black circle. Note, the radius of the circle is sized to be the required offset distance at the specific simulation terminal conditions of both the debris and PDV. If any of the offset distance database lookup parameters change (e.g. clock angle, relative azimuth angle) then the radius of the circle will change.

Figure 3.15 shows time histories for required offset distance (top plot) and constraint lookup parameters (bottom plot) over the 5 second transit trajectory shown in Figure 3.14. The instantaneous separation distance between the PDV and the debris (solid blue line) is 0 km at the start of the trajectory. Required altitude-planar separation distance (solid red line) at the start of the transition is 6.8 km. This large value stems from both the PDV and debris having the same flight state at 0 seconds. The black dashed line shows the difference between required and instantaneous separation distances. As the transit trajectory progresses, instantaneous flight states of the PDV and debris diverge from one another and the required offset distance decreases. After 5 seconds, instantaneous offset distance increases to 0.2 km where it exceeds required offset distance; the constraint is satisfied.

The bottom plot in Figure 3.15 shows time histories of constraint lookup parameters. Angle of attack is determined by the optimizer to satisfy required offset distances at transit trajectory termination; the optimized fixed angle is 31.1 degrees. Flight path angle becomes increasingly negative as the simulation progresses. The difference in velocity azimuth an-

gle, Phi, increases as the debris lift vector navigates the body away from the PDV. Clock angle, theta, increases as the debris navigates in the starboard, crossrange direction and aft, downrange direction relative to the PDV. Simulation conditions and optimized terminal values of database lookup parameters are reported in Table 3.8.

Transit Trajectory module hand-off parameters include required debris angle of attack, center of gravity thrust magnitude, and nominal trajectory flight end-state. The parameters are passed to the next module, Transit Trajectory Uncertainties, where they are used as inputs.

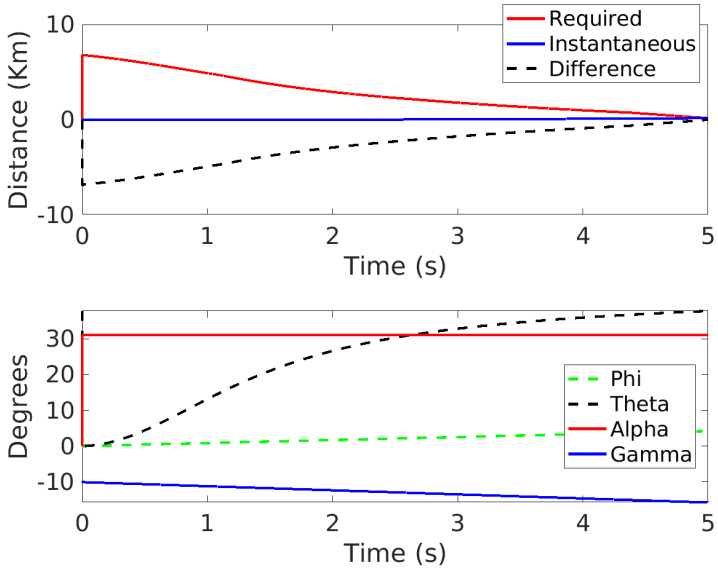

Figure 3.15: Time histories of dependent offset distance constraint and independent look-up parameters for the 5 second transit trajectory shown in Figure 3.14.

Table 3.8: Simulation Parameters for 5 Second Transit Trajectory

Parameter	value
Transit Duration	5 s
Bank Angle	135 deg
Optimal. Angle of Attack	31.1 deg
Theta	37.8 deg
Phi	4.2 deg
Terminal Flight Path Angle	-15.7 deg
Terminal Altitude	8.08 km
Req'd Theta Offset Distance	0.20 km

3.6 Transit Trajectory Uncertainties

Following optimization of the transit trajectory, dispersions on the end-state are estimated in the third module in Figure 3.5, Transit Trajectory Uncertainties. Three-sigma distributions on inputs feed through the previously-optimized transit trajectory simulation. Outputs corresponding to three-sigma input variations are assumed to represent three-sigma output variations on the transit trajectory end-state.

The end-state flight parameters of interest are those that will feed back into the first module, Determination of Required Offset Distance. Of the parameters listed in Table 3.5, tumbling flight path angle and velocity uncertainties due to transit trajectory uncertainties are assumed to have the largest effect on the debris field structure. All other parameters listed in Table 3.5 are not updated between methodology iterations.

Angle of attack, atmospheric density, and atmospheric dust content are assumed to be the only parameters that have uncertainty at transit trajectory initiation and also affect end-state parameters of interest. Other initial parameters (e.g. altitude) may have associated uncertainties but do not affect the end-state parameters of interest. Conversely, some initial parameters may affect end-state parameters of interest but do not have associated uncertainty. As an example, the transit trajectory is assumed to be initiated by a velocity trigger condition. As such, even though variations in initial transit trajectory velocity would affect the end-state velocity, it is assumed to be well-known and have no associated uncertainty. Additionally, initial velocity and flight path angle at transit trajectory initiation are assumed to be determined in the initialization phase of the methodology and are taken from a supplied full EDL trajectory profile as described in Section 3.3.1. Therefore, uncertainties on these two parameters are not handled internally in the methodology. To determine the effect of uncertainty in these two parameters, a study would have to be performed external to the methodology.

Table 3.9 summarizes the input distributions used to determine uncertainty end-state

conditions. The magnitudes of these distributions were chosen based on engineering judgment and input from senior engineers at NASA Langley's Atmospheric Flight and Entry Systems Branch. A 3-degree angle of attack variation is used to account for uncertainty in prescribed flight angle of attack and uncertainty in the ratio of lift-to-drag. Three-sigma atmospheric variations are accounted for using POST2 built-in Mars Global Reference Atmosphere Model 2010 (MarsGRAM) [69] functionality and data that modulates the 3-sigma high and low density while holding temperature and pressure at mean values. The nominal density is based on the MarsGRAM model. A variation of 0.2 is assumed to approximate the three-sigma distribution of atmospheric dust content as measured by the visual optical depth of the background dust level. The default MarsGRAM dust level of 0.3 is used as the simulation nominal value.

Table 3.9: Transit Trajectory 3-Sigma Uncertainty Input Parameters

Parameter	value
Angle of Attack	± 3 deg
Atmosphere Variations	$\pm 3\sigma$
Dust Variations	± 0.2

Figure 3.16 shows the spatial distribution of transit trajectory end-state uncertainties. The three plots have the same independent and dependent axes and show the same data. Each plot color-coordinates the data to show the effects of individual parameter uncertainties. Perturbations that increase an input parameter are shown as blue stars while perturbations that decrease an input parameter are depicted as red crosses. The nominal parameter values are shown as black squares. The red, solid line shows the terminal portion of the nominal transit trajectory without any uncertainties applied to the input parameters. To get an idea of the scale of the uncertainty spread, note that the nominal transit trajectory originates at 0 km downrange and 0 km crossrange while it terminates at approximately 3.15 km downrange and 0.11 km crossrange. The span of the end-state distribution covers approximately 3% of the transit trajectory path length.

The top plot color-codes high, low, and nominal dispersions on angle of attack. Each

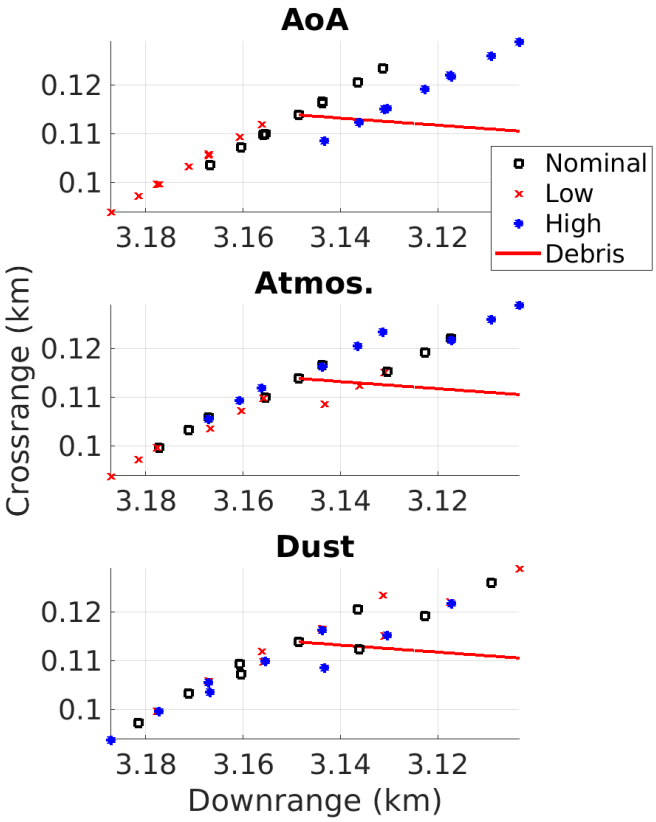

Figure 3.16: Distribution of transit trajectory end-states for variations in flight angle of attack, atmospheric density, and dust content. Simulation duration is 5 seconds.

angle of attack setting results in a distinct band of end-state spatial distributions. Increasing the angle of attack results in a decreased terminal downrange distance and an increased crossrange distance. Decreasing angle of attack increases downrange and decreases crossrange distance. These trends fit trajectory expectations for effectively modulating the lift-to-drag ratio of the debris.

The middle and bottom plots follow similar color-coding schemes for atmospheric variations and atmospheric dust content, respectively. Increasing atmospheric density results in decreased downrange and increased crossrange. The converse is true for decreasing density. Intuitively, this fits expectations. Increasing density increases drag resulting in shorter downrange distances. Increased density also increases lift, enabling larger crossrange distances. Lowering dust content decreases downrange distance and increases crossrange distance. Increasing dust content has the opposite effect.

Nominal and 3-sigma transit trajectory end-state dispersions feed into the offset distance constraint and Monte Carlo generation step to start the next iteration cycle of the methodology as illustrated in Figure 3.5.

3.7 Methodology Iteration Cycle Histories

Figure 3.17 shows iteration histories of key flight dynamics metrics for a 5 second transit trajectory and a debris separation bank angle of 135 degrees. The metrics are normalized by their value after the first iteration of the methodology; therefore, all metrics have a value of 1 at Run 1. Dimensional parameter values for Run 1 are reported in the figure legend. Run 1 uses estimates to initialize tumbling velocity and flight path angle when generating initial offset distance databases for the first iteration cycle of the methodology. The largest jump in parameter values is expected between Runs 1 and 2 as the methodology tunes the inputs to the offset distance constraint database generation to the specific problem rather than the initialization values. This jump is visible in Figure 3.17 for angle of attack, velocity, and flight path angle. After Run 2, successive iteration jumps are not as

significant and parameters oscillate around a mean value. Terminal azimuth angle sees minuscule parameter oscillations between successive iterations. Bank angle is fixed for this simulation and changes in angle of attack between iterations are not appreciable enough to affect significant changes in azimuth angle. The last four data points in Figure 3.17, which are circled in magenta, are generated using human-in-the-loop decision making at the end of the methodology iteration and are therefore not considered part of the automated methodology data set. These points are discussed later.

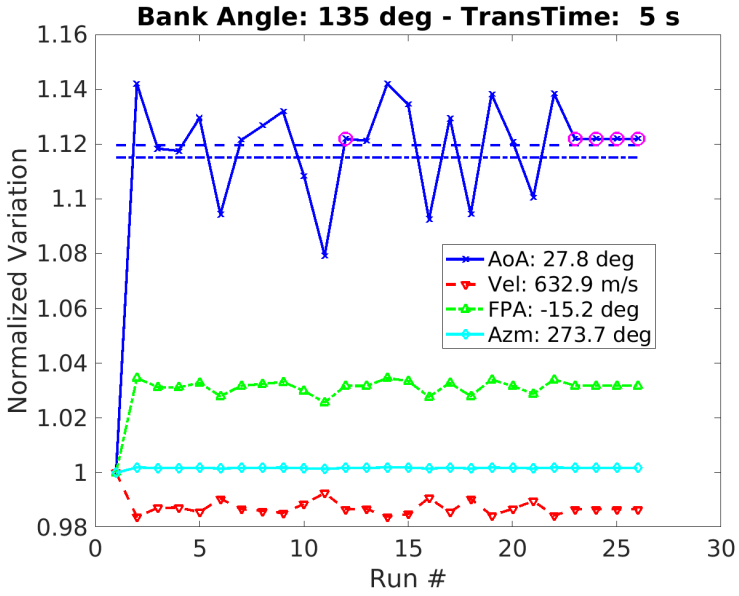

Figure 3.17: Methodology iteration histories for key flight dynamic parameters during a 5 second transit trajectory with a 135 degree jettison bank angle . Parameters include debris angle of attack, terminal planet-relative velocity, terminal flight path angle, and terminal azimuth angle. Each parameter history is normalized to its value at Run 1, which is reported in the figure legend. The four data points circled in magenta are generated with human-in-the-loop decision making at the end of the automated methodology iterations. The dot-dashed and dashed blue lines show the average angle of attack and average angle of attack excluding the first run value, respectively

The dashed and dashed-dotted blue lines in Figure 3.17 show two different mean angle of attack values across iteration cycles. The dashed-dotted blue line shows the total mean value, where as the dashed blue line shows the mean value not including the initialization run, Run 1. The iterations history appears to oscillate about these mean lines. Although they show no sign of asymptotic convergence, they do appear to be roughly bounded-

converged over the 20 iterations performed. See Section 3.7.1 for specific iteration stopping condition convergence criteria. The dashed-line provides a better estimate of the expected converged solution as it is not skewed by the somewhat arbitrary initialization run. Note, runs 23-26 (circled in magenta) are not part of the automated methodology iteration data set.

The optimization space for a single iteration of the methodology is highly nonlinear and stiff with many local optima. The constraint space is volatile and subject to proportionally large changes with small variations in input parameters such as debris flight path angle and velocity. Constraint databases suffer from high dimensionality with large feasible region spans across dimensions. To reduce dimensionality challenges, the methodology iteratively updates dependent parameters through sequential optimization cycles. This procedure results in successive solutions that oscillate about a mean objective value with deviations in the range of 3% the mean value. This oscillation is believed to be due to the stiff, nonlinear, and rough discretization of the constraint space.

For each angle of attack optimization within an iteration cycle, choice of initial guess for the optimization variable proved important. Two options were evaluated. The first option uses the previous iteration solution as the initial guess for the next iteration optimization problem. The optimization space can have several local optima and this option often struggled to arrive at the minimum angle of attack optima. Option two uses an initial guess that is smaller than the expected optimized value. The value is chosen through examination of the problem and experience. This option exhibited more stable behavior across various transition times and bank angles and is the primary option used in the present work.

Iterations 1 through 22 in Figure 3.17 are generated using a small-value initial guess rather than feeding the previous iteration solution into the next iteration. Inspection of these histories reveal relatively small solution changes between iterations 3 and 4 as well as 12 and 13. These small changes between iterations indicate the iteration solutions are near a converged solution. The small value initial guess approach used in the original

generation of Runs 12 through 14 ultimately resulted in divergence from the suspected converged solution in the vicinity of Runs 2, 4, 12, and 13. Five angle of attack iteration data points in Figure 3.17 are encircled in magenta. The solution at Run 12 is copied over and rerun as Run 23 and then iterated on using previous iteration solutions as initial guesses to successive iterations. This iteration solution is recognized as a converged solution when using previous iteration solutions as the next iteration initial value. The main trend line (dashed blue) approximates this converged solution very well, as previously posited.

3.7.1 Iteration Convergence Criteria

The methodology convergence criteria is designed to identify when the methodology is iterating around a mean value. When this condition is met, subsequent methodology iterations do not move the iteration mean significantly. A 4-point trailing average of angle of attack iteration history from Figure 3.17 is displayed in Figure 3.18. The 4-point trailing average shows how the mean value of the localized angle of attack iteration history in Figure 3.17 develops as methodology iterations progress. Data in Figure 3.18 is normalized by the same value as the angle of attack iteration history in Figure 3.17. A 4-point bin size was selected for the trailing average computation in order to keep the bin size small enough such that individual point contributions to the mean are not too diluted but large enough so that the mean is not too heavily influenced by a single point. The bin size was chosen to be an even number because iterations tend to continuously overshoot a mean value, so an even bin size would in theory replace a high value with a high value in the bin and a low value with a low value as the bin moves forward. In Figure 3.18, the 4-point trailing mean increases until iteration 6 at which point it approximately plateaus.

The convergence criteria used in the present implementation of the methodology is a follows: convergence is achieved when the maximum difference between a trailing average point and its three previous points is less than 2% of the normalization value. For example, at iteration 7 in Figure 3.18, differences are take between iteration 7 and 6, 7 and 5, and

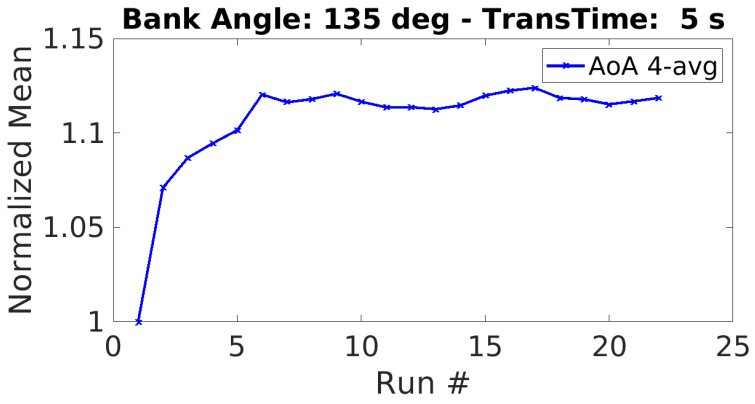

Figure 3.18

7 and 4. The maximum of those differences becomes the convergence metric at iteration 7 and is plotted in Figure 3.19. This approach was chosen to ensure convergence is not falsely declared if two adjacent points happen to be close in value. Requiring a group of four points to be close in value reduces the likelihood of false convergence criteria positives. Convergence criteria calculations are shown in Figure 3.19. Iteration 8 satisfies the convergence criteria and would stop the methodology iteration cycle. Additional iterations were run in the present case for purposes of exposition. It is worth noting, based on Figure 3.18, the mean appears to be fully established by iteration 6, however the convergence criteria is not satisfied until iteration 8 due to the formulation of the convergence criteria differencing scheme.

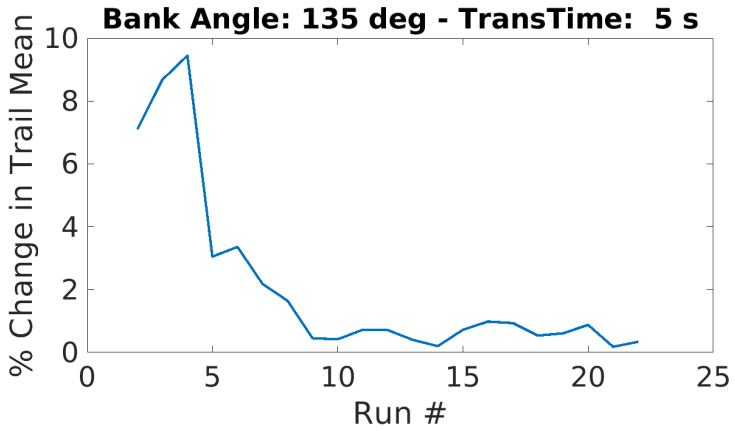

Figure 3.19

3.8 Trends Across Bank Angles and Transition Times

Figure 3.20 presents iteration histories of angles of attack for bank angles between 90 and 225 degrees during a 5 second transit trajectory. For each bank angle, the figure accumulates data analogous to that displayed in Figure 3.17 and collapses it into a point cloud at a single bank angle so that data for several bank angles can be viewed at once. Average iteration values are identified by green circles. Blue stars show all iteration values.

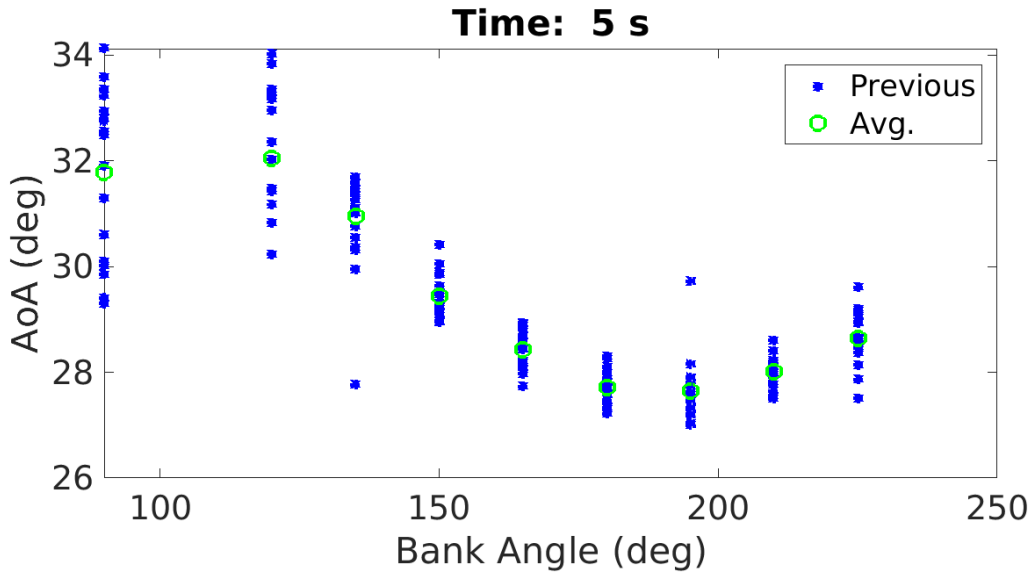

Figure 3.20: Angle of attack convergence scatters for bank angles between 90 and 225 degrees for a 5 second transition time. For each bank angle, average angle of attack is identified by green circles. Previous iteration solutions are indicated by blue stars.

The span of iteration values for each bank angle gives a sense of the variability of the solution. Data spread is largest for bank angles less than 135 degrees and smallest for bank angles around 180 degrees. Figure 3.17 shows solutions tend to vary around a mean value. The trend of mean angle of attack data (green circles) in Figure 3.20 is relatively smooth with a minimum between 180 and 195 degrees. Note, the total variation between mean angles of attack versus bank angle is roughly 4 degrees. This variation is on the same order of magnitude as the variation applied to the transit trajectory input parameters to generate the transit trajectory end-state uncertainties in the methodology iteration cycle.

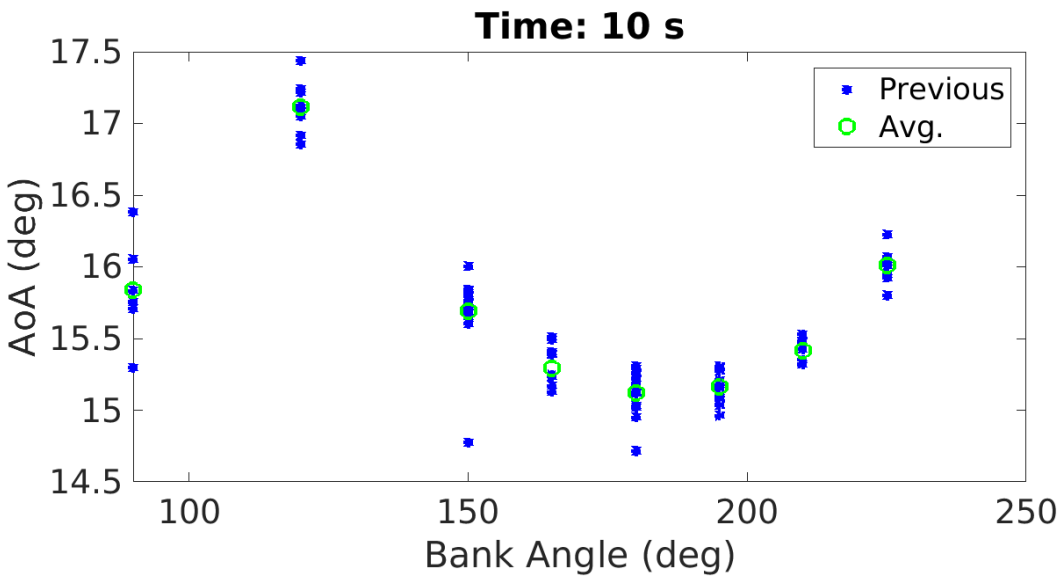

Figure 3.21: Angle of attack convergence scatters for bank angles between 90 and 225 degrees for a 10 second transition time. For each bank angle, average angle of attack is identified by green circles. Previous iteration solutions are indicated by blue stars.

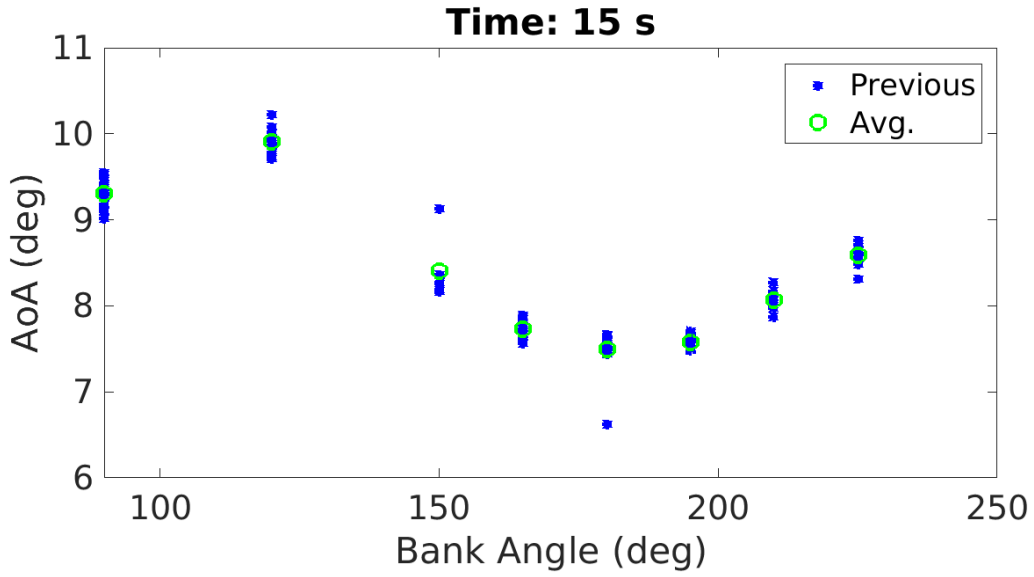

Figure 3.22: Angle of attack convergence scatters for bank angles between 90 and 225 degrees for a 15 second transition time. For each bank angle, average angle of attack is identified by green circles. Previous iteration solutions are indicated by blue stars.

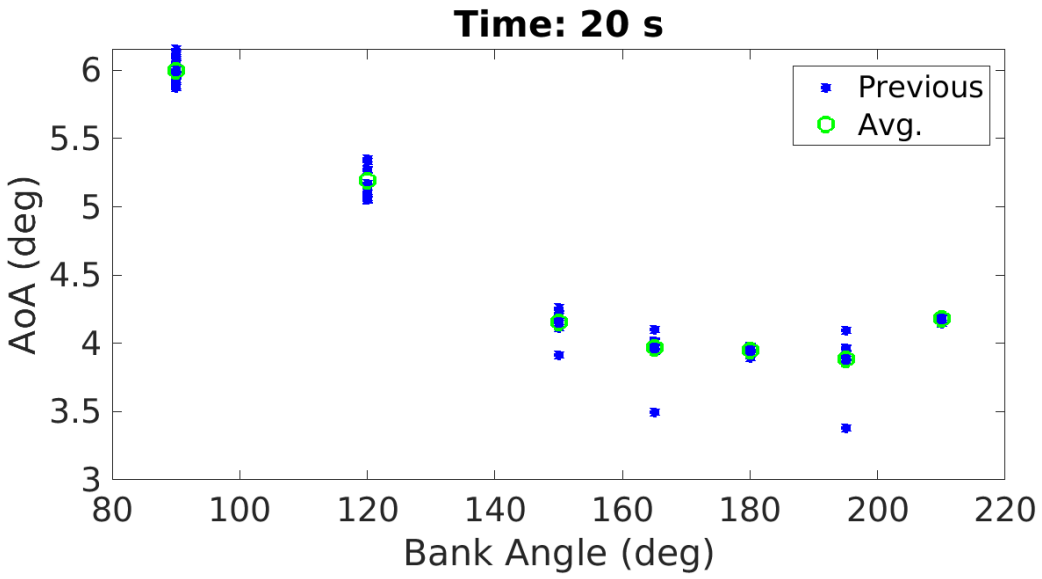

Figure 3.23: Angle of attack convergence scatters for bank angles between 90 and 225 degrees for a 20 second transition time. For each bank angle, average angle of attack is identified by green circles. Previous iteration solutions are indicated by blue stars.

Figure 3.20 presented optimized angles of attack for a range of bank angle separations for a 5 second transit trajectory. Based on this data, an angle of attack of 28 degrees is the minimum trim angle that will satisfy offset distance constraints for a 5 second transit trajectory. This angle of attack occurs at a debris separation bank angle of 180 degrees.

Data for transit trajectories of durations 10, 15, and 20 seconds are presented in Figures 3.21, 3.22, and 3.23. Figure 3.24 shows a phase diagram of transition time versus minimum and maximum required angle of attack to satisfy minimum offset distance constraints for transition times of 5, 10, 15, and 20 seconds. As transition time increases, there is a decrease in the angle of attack required to satisfy minimum offset distance constraints. Note, the variation of required angle of attack versus transition time is an order of magnitude higher than the angle of attack sensitivity to bank angle for a given fixed transition time.

3.9 Perspective on Methodology Use

The present methodology addresses a gap in current analysis capability. Previous human Mars descent architecture studies neglected to perform trajectory and risk analysis of post-

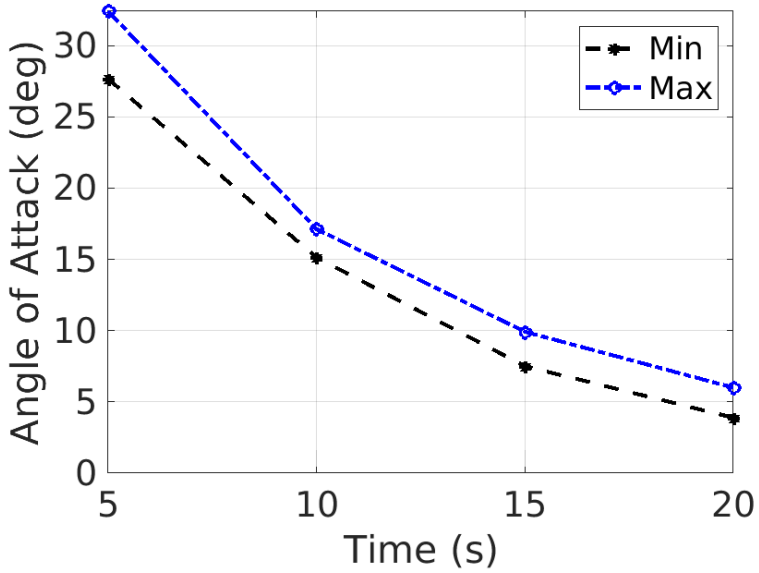

Figure 3.24: Optimal debris angle of attack for transition times between 5 and 20 seconds. For a 5 second transition time, the optimal transition angle of attack is taken to be the minimum of Figure 3.20. Optima for transition times between 10-20 seconds are calculated from data analogous to that presented in Figure 3.20. Maximum angle of attack solutions for transition times between 5 and 20 seconds are shown in blue.

separated debris resulting from supersonic jettison events. This neglect stems from an absence of formalized approaches for evaluating risk posed to a descent mission by supersonically ejected debris.

3.9.1 Archaic Approach to Separation Analysis

In the absence of prescribed approaches for quantifying debris risk and subsystem requirements necessary to mitigate risk, a jettisoned debris flight dynamics analysis might look as follows. The goal of the separation systems analyst is to determine settings of angle of attack, transition time, and jettison bank angle such that the debris is safely discarded from the primary descent vehicle.

Figure 3.25 shows the debris aerodynamic moment coefficient versus angle of attack for the semi-aeroshell geometry from the clamshell jettison studied throughout the present work. The debris is nearly naturally stable at 15 degrees angle of attack, so an analyst might

decide the debris will trim at 15 degrees after separation. Because the clamshell jettison ejects two symmetric aeroshell halves, the analyst might choose a separation bank angle of 90 degrees to complement the natural symmetry of the jettison architecture. A 5 second transition time is selected to preserve altitude-velocity performance of the primary vehicle. At this point, the analyst would simulate the flight dynamics of the debris relative to the primary descent vehicle using the selected simulation parameters and determine the relative proximity of the two bodies at the end of the transition time. Then a tumbling debris field would be generated based on the debris transition time end-state. At this point the analyst would discover that a 15 degree angle of attack at a 90 degree bank angle for a 5 second transition time has the primary vehicle flying through the aeroshell debris field. Now the analyst has more choices to make: do they increase the transition time thereby sacrificing landed mass? Do they perform a more complicated jettison maneuver at a different bank angle? Do they increase the trim angle of attack by incorporating flight control subsystems on the jettisoned debris? At the end of their work, they have an infeasible design and are no closer to a solution than when they began. Once a solution is achieved, it will be a point design and invalidated by any changes in the mission or separation architecture.

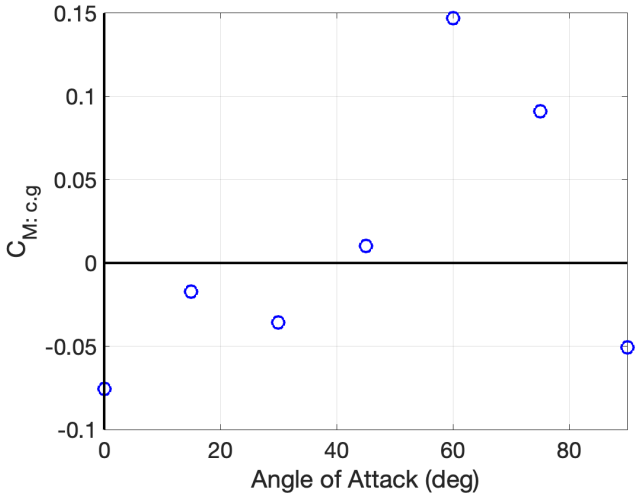

Figure 3.25: Aerodynamic moment coefficient versus angle of attack for the semi-aeroshell debris geometry used throughout the present work.

3.9.2 Methodology Results and Analysis

As currently implemented, the present methodology is highly automated. For a single setting of transition time and bank angle, the methodology yields a solution within a few percent of the converged optima in as few as 2 iterations in many cases (see Figure 3.17). A mean solution is identified in less than 10 iterations. For the same effort a user would expend running a single case independently, a full database of converged angle of attack and thrust solutions may be generated across various bank angles and transition times. Generating a full database of solutions only increases computational resource requirements rather than personnel time. By using the methodology to analyze a separation architecture, an analyst will generate results similar to those displayed in Figures 3.20, 3.21, 3.22, 3.23, and 3.24. Rather than ending up with a single, infeasible point design when using the archaic approach, the user generates a set of feasible designs that can be evaluated for suitability to meet a wide variety of mission design considerations.

Based on Figure 3.20, a 5 second transit trajectory with a 90 degree bank angle jettison requires a 32 degree debris trim angle of attack. A 180 degree bank angle jettison allows for a more efficient 28 degree angle of attack; a 4 degree improvement over the 90 degree bank angle separation. Assuming mass penalties for aerodynamically trimming debris consist of a fixed bias mass penalty for trimming away from the natural stability angle of attack and a small proportional penalty for trimming at increasingly larger angles of attack, a designer may determine a 90 degree bank angle is worth the increased trim angle of attack over the 180 degree bank angle separation due to the inherently reduced complexity of the separation. The present methodology considers the motion of a single piece of debris relative to the primary descent vehicle. For jettison architectures ejecting multiple pieces of debris, like the clamshell exit (in this case two symmetric pieces of debris), the motion of both pieces must be considered. If one aeroshell half is ejected at 180 degrees, the other half would be ejected at 0 degrees and initially deposited at an altitude above the PDV. In this case, the two aeroshell halves would have different offset distance requirements and

separation system performance requirements. A designer might decide a 4 degree trim angle of attack savings is not worth increasing the complexity of the separation and would instead opt for a symmetric 90 degree bank angle separation.

Alternatively, perhaps the designer wishes to use a symmetric 90 degree bank angle separation but wants the debris to trim at its natural 15 degree angle of attack stability point. Based on Figure 3.24, a transition time around 11 seconds would be required.

The present methodology delivers sufficient data to make informed design decisions for a variety of jettison architecture conditions. The data allows for a designer to estimate required system performance as well as specify the desired level of tolerated far-field recontact risk. The present study utilizes 95% bounds on tumbling debris flight span correlating to a maximum 5% far-field recontact risk. The methodology identifies whether a jettison architecture is achievable using aerodynamic debris control alone or if thruster impulse is required to satisfy far-field recontact risk requirements.

The archaic method gives a single design point that provides no insight beyond the exact conditions for the design point.

A primary assumption of this analysis is that separation subsystem mass is correlated with debris trim angle of attack. Figure 3.24 indicates that a 20 second transit time is the most mass efficient from a separation subsystem perspective. However, longer transition times result in significant mass penalties from the perspective of the full EDL timeline. Increased transition times result in significant loss of altitude with minimal loss in velocity resulting in heavier descent systems or less landed payload mass. A trade-off between separation subsystem mass and total EDL system mass must be performed. This analysis was notably missing from the EDLSA work. It is the intention that the present work can assist in performing future trade studies in this regard.

3.9.3 Implication of Results to the Broader Field

The EDLSA did not perform any detailed flight dynamic analysis of supersonic descent vehicle transitions despite their inclusion in several proposed descent mission architectures. At the time the study was performed, an attempt to conservatively estimate the loss in altitude and velocity performance due to the transition event was made. A 20 second duration segment of flight was built into the simulation during which propulsion and aerodynamics were turned off. A 20 second duration was selected based solely on engineering gut instinct that this would provide a conservative estimate. No hard analysis reinforced the selection. The results of the present analysis show the required transition duration is about half of the EDLSA estimate of 20 seconds; the hinged-exit architecture only requires an 11 second transition duration to mitigate far-field recontact risks using the natural passive stability of the debris. Furthermore, at the end of 11 seconds, the hinged-exit debris is approximately 200 meters away from the primary vehicle; this large distance indicates that it may be possible to safely turn on the primary vehicle's propulsive descent engines before the full 11 second duration has expired without the risk of engine plume interaction with the ejected debris. The ability to save 9 of the previously assumed 20 seconds, can have significant impacts on the overall mission design, including but not limited to vehicle entry mass, payload landed mass, required descent engine thrust magnitude, and required lift-to-drag performance of the entry vehicle. The applicability of these implications must be considered within the context of the underlying assumptions that went into the methodology analysis. Primary methodology assumptions include consideration of only far-field recontact risks, no consideration of near-field separation mechanisms, the debris is fully responsible for the transition divert maneuver, and interference aerodynamic effects are not presently considered.

3.9.4 Extensibility of Methodology

The methodology was developed to address a gap in analysis capability to investigate performance requirements of supersonic descent vehicle transitions for human Mars missions. However, the methodology is much more generally applicable than that. The methodology structure enables it to be used for any problem that requires the primary descent vehicle fly around, and not through, the debris field of an ejected piece of solid mass. This includes hypersonic and supersonic jettisons. This includes descent missions to any planet or celestial body with or without an atmosphere. This includes mission masses ranging from small robotic missions to large human landed mass missions. Finally, this includes a wide variety of entry vehicle types, including but not limited to slender lifting bodies, entry capsules, and hypersonic inflatable devices. The choice of developing the methodology around a large mass, slender lifting body, human Mars mission was made because these types of mission likely require performing an aeroshell jettison to enable the mission and as such are topical and presently impactful.

3.10 Verification and Validation

Validation of this methodology proved challenging. Ideally, the results of the methodology could be validated using typical approaches of comparing against existing simulation or experimental data in literature. However, these approaches proved infeasible. Due to the undeveloped state of this research field, there is a lack of relevant data to compare against. Notably, this lack of data results from supersonic descent separations never having been attempted. Subsonic descent jettisons have been utilized to eject heatshields prior to propulsive terminal descent and lander separation from an aeroshell. However, these jettison events have primarily been used for robotic landers at Mars. In such missions, there were no pre-deployed ground assets near the landing site meaning the landing footprint of the debris was not a concern to mission designers. Furthermore, ballistic coefficient differ-

ences between the ejected debris and primary descent vehicle were sufficient to ensure no in-flight recontacts once the two bodies were initially separated. These characteristics of previous subsonic decent jettisons meant there was no need to constrain the primary vehicle to not fly through the jettisoned heatshield spatial debris field. Similarly, supersonic ascent jettisons, such as payload fairing jettisons and solid rocket motor jettisons on ascent vehicles, are characterized by the primary vehicle and the jettisoned debris traveling in opposite directions with respect to the local gravity vector; therefore, far-field recontacts and debris landing footprint have no relevance to mission success. As such, these cases do not produce appropriate validation data for comparison against the present methodology results.

Since existing flight separation data was not applicable to methodology validation, an experimental test campaign was evaluated for suitability and applicability to methodology validation. As part of a NASA design campaign for a mid L/D human Mars decent vehicle, a ballistic range experiment was designed and performed by NASA. The ballistic range test sought to evaluate dynamic stability for the mid L/D vehicle at supersonic speeds. To perform this test, models of the test vehicle were encase in a shroud such that the test article could be launched from a powerful artillery weapon much like an artillery shell. After exiting the gun barrel, sabots shed off like flower petals to reveal the test model inside. The dynamic event of shedding the sabots and evaluating their jettisoned motion bore similarity in both flight conditions and vehicle architecture to the jettison of an aeroshell during supersonic descent. However, under further investigation the experiment was determined to not produce usable methodology validation data. Three primary deficiencies were identified. First, the geometry of the shedding sabots was very angular. Such shapes are not well suited for analysis by NASA's Cart3D inviscid Euler solver - the aerodynamics tool used in the present research. Second, test engineers were not able to capture key angular state time histories that would enable detailed dynamic analysis of the motion of the sabots during and after separation.

Finally, the ballistic range sabot separation was a passive separation - the jettisoned

debris was neither designed to trim at an angle of attack nor was an impulse applied to the debris to augment the separation. Additionally, the time scale of the experimental flight was short enough that concerns of far-field debris recontact risks or debris landing footprint were non-existent. The ballistic range test did not share key characteristic similarities with the present methodology. Namely, the methodology seeks to prescribe requirements for mitigating hazardous debris landing footprints and far-field recontact risks. In the absence of those threats within the experiment, the core component of the methodology can not be validated. The only similarity that is left is the motion of jettisoned debris under the influence of interference aerodynamics. Indeed, the accuracy of the CFD tool chosen for use in the methodology is a key assumption that underpins the accuracy of any results that are generated. However, the methodology is designed to be modular in nature. As such, it contains the ramifications of CFD selection to an individual module that is dependent on the user to motivate the validity of. In the present study, NASA's Cart3D is used to generate isolated aerodynamic databases for both the debris and primary descent vehicle at supersonic flight conditions during Martian descent. Precedent exists in the literature for using Cart3D for such applications[61, 4, 63, 67] but there are existing concerns about the tool's accuracy when two bodies are in near proximity. Such concerns are beyond the scope of the present research and left up to the developers of the CFD tool to accomplish. The implementation of the methodology only assumes the users has selected and generated representative aerodynamics database and that the results of the methodology will be limited in accuracy by the underlying assumptions of the individual module. The methodology can accommodate aerodynamics databases generated by any CFD tool and is not limited to Cart3D.

The methodology was designed from first principals. The methodology utilizes Monte Carlo analysis to determine debris fields. Monte Carlo analysis has been validated across numerous applications to predict behavior of a vehicle due to statistically distributed perturbations about nominal initial states. The determination of initial states and perturbation

distributions requires validation. In the present study, these values are taken from literature where applicable or determined iteratively within the Methodology. The validity of Monte Carlo analysis comes down to the implementation of the analysis and the accuracy of the underlying user models. As previously stated, the methodology is modular and robust to different user assumptions. Validation and accuracy of the Monte Carlo component comes down to the module assumptions and desired level of analysis fidelity. The present study assumes the debris tumbles without the use of flight control systems after termination of the transit trajectory phase of flight. The motion of the tumbling debris is determined by integrating the translational and rotational equations of motion given models for aerodynamics and vehicle inertias. Inertias are generated using CAD software and compared against component approximations. Aerodynamics are generated using Cart3D. Intuition validity checks are performed from expectations of lift and drag trends versus body orientation as well as on the location of zero angular moment body orientations. In the present work, POST2 flight dynamics equations of motion and atmospheric models are assumed to be accurate. In the absence of a dedicated experimental validation campaign, the present work focuses on verification of model implementations.

3.10.1 Transit Trajectory

Verification of the transit trajectory is approached as a verification of the model implementation of the transit trajectory within POST2. The goal of the validation exercise is to externally compute vehicle accelerations and compare them with the internally calculated POST2 accelerations at every simulation time-step. Vehicle acceleration is computed from Equation 3.1, where a is the total vehicle acceleration, g is the local gravitational acceleration, F_A is the aerodynamic force acting on the vehicle, and m is the vehicle mass.

$$a = g + F_A/m \tag{3.1}$$

Acceleration due to gravity is approximated as a constant $3.71 m/s^2$. Angle of attack,

sideslip, and Mach number are read out of the POST2 simulation and used to perform an independent database lookup of aerodynamic coefficients. These coefficients are used to determine the aerodynamic forces acting on the vehicle. Figure 3.26 shows the results of this validation exercise. Accelerations are shown in the planet-centered inertial frame. POST2 values are displayed with dotted lines. Verification values are displayed with dashed lines. Verification and POST2 accelerations closely agree in all three orthogonal inertial coordinates directions.

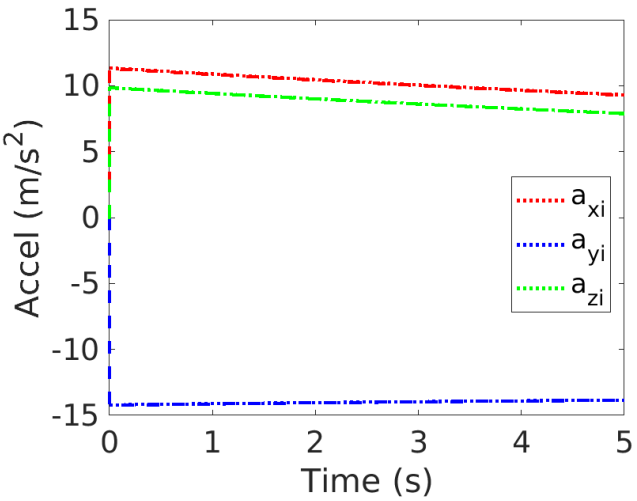

Figure 3.26: Verification of debris accelerations during a 5 second transit trajectory. Accelerations are in a planet-centered inertial frame. Accerations calculated by POST2 are displayed with dotted lines. Accelerations externally calculated as part of the verification activity are displayed with dashed lines. Line colors identify component accelerations along the reference frame coordinate axes.

3.10.2 Propulsive Descent

Verification of propulsive descent simulations is approached through checks on expected versus measured velocity change, ΔV. Thrust and gravitational external forces act on the vehicle to produce a change in vehicle velocity. Verification checks are performed to ensure the simulation model and setup produce velocity changes in line with theoretical calculations. Equation 3.2 gives the theoretical change in velocity due to a thrusting engine. ΔV_{Thrust} is the change in vehicle velocity due to thrust, I_{sp} is the specific impulse of the

rocket engine, g_{E0} is the standard surface gravity of Earth, m_i is the initial mass of the vehicle, and m_f is the final mass of the vehicle after the thruster burn. Equation 3.3 gives the change in velocity due to gravity acting on the vehicle. Vehicle flight path is γ_r, local Martian gravity is g_M, and the calculation is performed from initial time t_i until final time t_f. The velocity change due to external forces is given by Equation 3.4 as the difference between ΔV_{Thrust} and ΔV_{Grav}. The actual velocity change experienced by the vehicle is given by Equation 3.5 as the difference between the initial and final vehicle velocities.

$$\Delta V_{Thrust} = I_{sp} g_{E0} \ln \frac{m_f}{m_i} \tag{3.2}$$

$$\Delta V_{Grav} = \int_{t_i}^{t_f} -\sin(\gamma_r) g_M dt \tag{3.3}$$

$$\Delta V_{External} = \Delta V_{Thrust} - \Delta V_{Grav} \tag{3.4}$$

$$\Delta V_{Actual} = V_i - V_f \tag{3.5}$$

Parameters used in the verification activity are reported in Table 3.10. Calculated and measured ΔV's are reported in Table 3.11. The actual ΔV experience by the vehicle is 675.3 m/s. The calculated ΔV due to external forces is 681.4 m/s. The difference between these two metrics is 6.1 m/s, or 0.9%. The difference is in-line with errors due to Euler integration and a constant Martian gravity assumption used in analytical ΔV computations.

3.10.3 Debris Field

Altitude Translation

Offset distance constraint databases are formed assuming debris fields can be generated originating from a single high altitude (e.g 10 km) and then shifted down in altitude in post-

Table 3.10: Propulsive Descent Validation Parameters

Parameter	value
Duration	67.6 s
h_i	8168 m
h_f	50 m
V_i	675 m/s
V_f	0 m/s
m_i	68500 kg
m_f	55267 kg

Table 3.11: Propulsive Descent Validation Results

Parameter	value
ΔV_{Thrust}	820.9 m/s
ΔV_{Grav}	139.4 m/s
$\Delta V_{External}$	681.4 m/s
ΔV_{Actual}	675.3 m/s

processing to determine required offset distance for debris that begin tumbling at lower altitudes (e.g. 8 and 6 km). This assumption is made to reduce the number of tumbling Monte Carlo simulations that must be generated. Adding an altitude dimension to the test matrix of Monte Carlos that must be run can increase run times by a full order of magnitude. The goal of the present section is to quantify and bound the error induced by this assumption.

The assumption suffers from the shortcoming that initiating tumbling at a lower altitude results in the debris flying through higher atmospheric densities at higher velocities compared to a piece of debris that begins tumbling at higher altitudes with all other initial state properties being equal (e.g. velocity and flight path angle). The effect of flying through higher densities at higher velocities results in a increased scatter of possible debris trajectories and a subsequent enlarging of the debris field. Figure 3.27 shows two debris fields overlaid. The blue debris field is generated from an initial tumbling altitude of 8 km. The magenta debris field is generated at 10 km initial tumbling altitude and then shifted down 2 km in post-processing to approximate a 8 km tumbling origin. Both debris fields have the same initial flight path angle and velocity. The blue debris field that actually originated at 8

km altitude has a larger debris envelop as compared to the 10 km shifted debris field. The larger flight envelop requires larger offset distances between the debris and primary descent vehicle to avoid far-field recontact risks. The current validation activity seeks to determine what increase in transit trajectory performance metrics (i.e angle of attack) is required to overcome these increased offset distances as compared to databases generated using the assumption that debris fields can be shifted downward in altitude in post-processing.

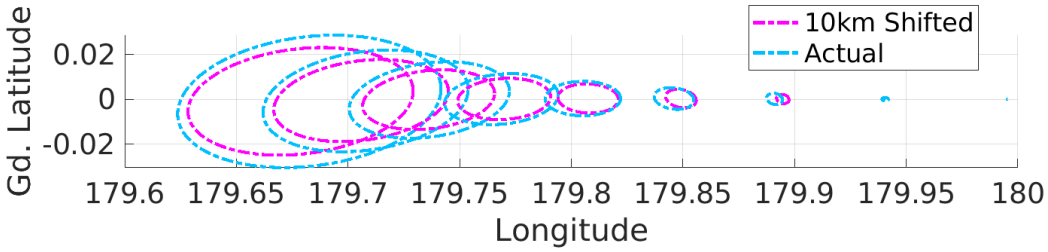

Figure 3.27: Two debris fields overlaid on one another. The blue debris field is generated from an initial tumbling altitude of 8 km. The magenta debris field is generated at 10 km initial tumbling altitude and then shifted down 2 km in post-processing to have the same 8 km origin as the blue debris field. Both debris fields have the same initial flight path angle and velocity.

Figures 3.28, 3.29, 3.30, and 3.31 include identical data as Figures 3.20, 3.21, 3.22, and 3.23 with the addition of red data points showing mean validation solutions at specified separation bank angles. Validation solutions are generated by not assuming debris fields can be translated downward in post-processing to approximate debris fields that begin tumbling at lower altitudes. The red data points are analogous to the green data points but represent the average of validation data that generates new Monte Carlos for each altitude in the offset distance database. Under normal operation, the methodology generates 7 Monte Carlos each time an offset distance database is generated - once per methodology iteration cycle. Under the validation implementation of the constraint database generation, more than 80 Monte Carlos are generated to account for the extra altitude dimension of the test data matrix.

Figures 3.28, 3.29, 3.30, and 3.31 show the validation mean data is very much in line with the assumption data sets used in the methodology. In all cases the validation data

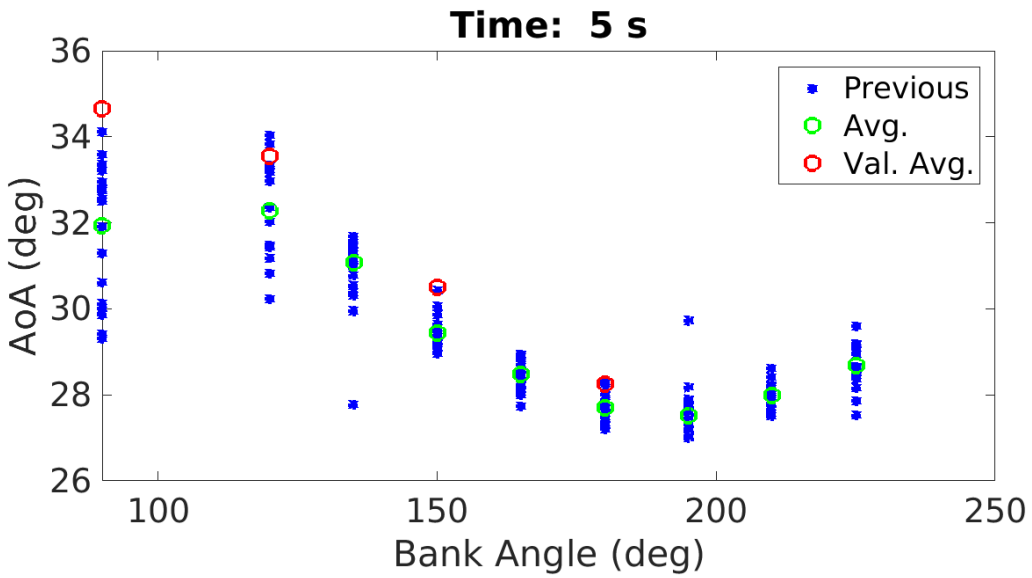

Figure 3.28: Angle of attack convergence scatters for bank angles between 90 and 225 degrees for a 5 second transition time. For each bank angle, average angle of attack is identified by green circles. Previous iteration solutions are indicated by blue stars. Red circles are analogous to green circles but are the average of validation runs that generate new Monte Carlo for each altitude in the offset distance database rather than shifting a single altitude Monte Carlo.

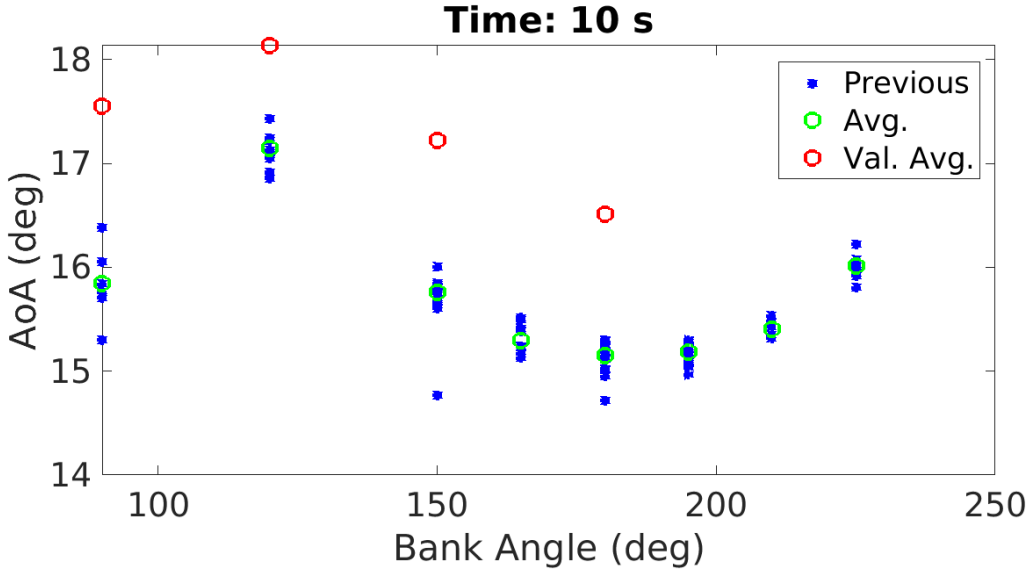

Figure 3.29: Angle of attack convergence scatters for bank angles between 90 and 225 degrees for a 10 second transition time. For each bank angle, average angle of attack is identified by green circles. Previous iteration solutions are indicated by blue stars. Red circles are analogous to green circles but are the average of validation runs that generate new Monte Carlo for each altitude in the offset distance database rather than shifting a single altitude Monte Carlo.

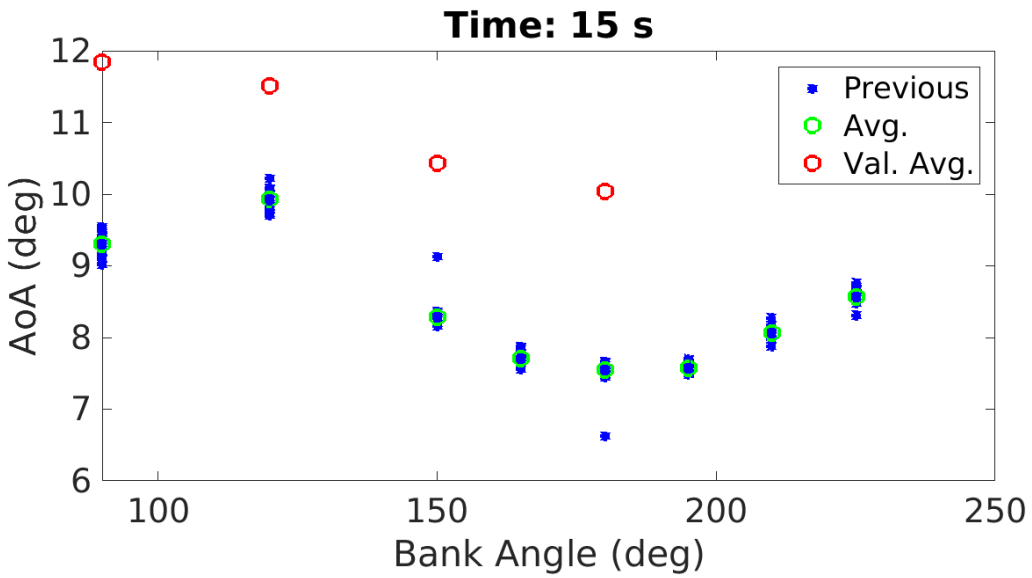

Figure 3.30: Angle of attack convergence scatters for bank angles between 90 and 225 degrees for a 15 second transition time. For each bank angle, average angle of attack is identified by green circles. Previous iteration solutions are indicated by blue stars. Red circles are analogous to green circles but are the average of validation runs that generate new Monte Carlo for each altitude in the offset distance database rather than shifting a single altitude Monte Carlo.

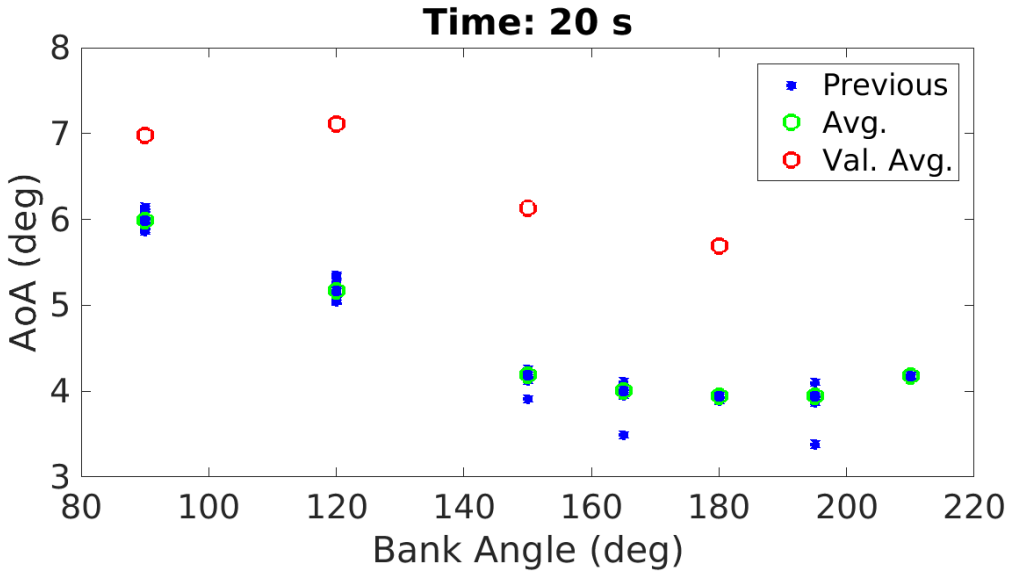

Figure 3.31: Angle of attack convergence scatters for bank angles between 90 and 225 degrees for a 20 second transition time. For each bank angle, average angle of attack is identified by green circles. Previous iteration solutions are indicated by blue stars. Red circles are analogous to green circles but are the average of validation runs that generate new Monte Carlo for each altitude in the offset distance database rather than shifting a single altitude Monte Carlo.

requires a higher angle of attack than the assumption data. This trend fits expectations; for the same initial velocity and flight path angle, debris that begins tumbling at a lower altitude will fly through denser atmosphere at higher velocities resulting in increased spread of tumbling trajectories. The increased spread of trajectories results in larger debris field volumes and larger required offset distances (See Figure 3.27). Larger offset distances require larger trim angles of attack to meet offset distance constraints.

Figure 3.32 shows the difference in required trim angle of attack between the validation data set and assumption data set versus initial debris tumble altitude. Initial tumble altitude corresponds to transit trajectory terminal altitude and varies with transit trajectory duration; longer transit times result in lower initial tumbling altitudes while shorter transit times result in higher initial tumble altitudes. The general data trend shows the angle difference increasing as initial tumble altitude decreases. Stated another way, the error of the assumption increases as the true initial tumbling altitude diverges from the approximated 10 km altitude of the underlying assumption. Over the range of simulation conditions in the present study, the angle error is bounded at 2.75 degrees. For perspective, the difference between minimum and maximum bank angle solutions at a given transit time is on the order of 4 degrees in Figure 3.24. The angle of attack uncertainty applied to the transit trajectory initial state to produce uncertainty distributions on transit trajectory end-state is ± 3 degrees.

3.10.4 Trend Validation

The methodology was designed with inherent self-validation in mind. Different phases of analysis use statistical variation sampling to obtain state distributions and demonstrate trend validation. Figure 3.16 shows spatial distributions of transit trajectory end-states for a range of perturbed initiation conditions. The optimized transit trajectory is run for estimated three sigma perturbations on angle of attack, atmospheric density, and atmospheric dust content. The resulting transit trajectory end-states feed into the next step of offset dis-

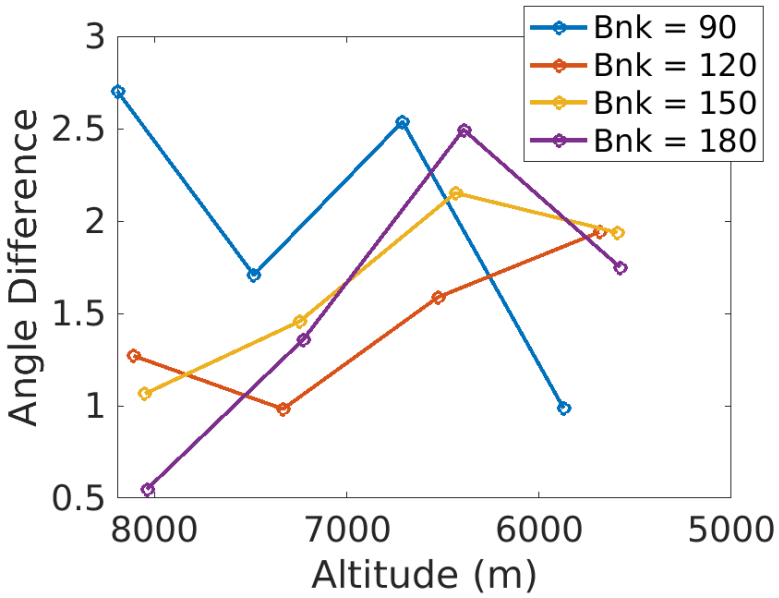

Figure 3.32: Trend lines for required trim angle of attack at four different separation bank angle plotted versus tumbling initial altitude. Tumbling initial altitude is directly correlated to transition time. Smaller transition times results in debris tumbling at higher altitudes. Longer transition times result in debris tumbling at lower altitudes. Data is collected for simulations with transition time of 5, 10, 15, and 20 seconds.

tance constraint database generation through Monte Carlo analysis. However, this step is also serves to validate the implementation of the transit trajectory simulation. By perturbing the inputs and observing the outputs, the transit trajectory is considered trend validated if a small input perturbation results in a small output perturbation.This is indeed the observed trend. For perturbations of ± 3 degrees angle of attack, a spatial variation on the trajectory end-state of 51 meters or 1.5% of the path length of the trajectory is observed. Furthermore, flight dynamics intuitions for modulating the lift-to-drag ratio of the debris are satisfied by the observed trends. Increasing the angle of attack results in a decreased terminal downrange distance and an increased crossrange distance. Decreasing angle of attack increases downrange and decreases crossrange distance.

Perturbations of atmospheric density by MarsGRAM three sigma values result in 25 meters of spatial variation or 0.7% of the transit trajectory path length. Variations in dust visual optical depth of 0.2 off a nominal of 0.3 result in 14.5 meters or 0.4% of the trajectory

path length. Realistic changes in the simulation inputs do not cause drastic changes in outputs.

The iteration histories of the methodology also support trend validation of the methodology outputs. Each methodology iteration cycle uses the outputs of the methodology as the inputs of the next iteration cycle. In effect, this process demonstrates the continuity of the methodology outputs to perturbations on the methodology inputs. Figure 3.17 presents iteration histories of key simulation inputs and outputs. For any given run, the simulation outputs are used as the nominal inputs for the next simulation run. Likewise, the outputs for a given run may be compared to the run nominal inputs which are identical to the outputs for the previous iteration. Iteration histories for three-sigma variations on the nominal parameters are not shown in the figure. The iteration histories demonstrate similar validation results as the previous discussion on transit trajectory end-state distributions. Bounded perturbations on input values produce bounded output values that align with expectations based on flight dynamic intuition.

Previous discussion identified that transit trajectory optimization is sensitive to choice of initial value. A chaotic sensitivity to initial value choice would indicate potential problems with the simulation and results. Figure 3.17 shows iteration histories generated using a conservatively low initial value approximation for angle of attack. The same simulation was run using the alternative approach to choosing initial values whereby the previous iteration run serves as the initial value for the next iteration optimization. The iteration histories of this alternative approach are displayed in Figure 3.33. Both Figure 3.17 and 3.33 use a conservatively low initial value estimate for the Run 1. Starting at Run 2 the initial value approaches differ from one another. Runs 1 through 6 generally agree with each other between simulations. As the run number increases beyond Run 6 the history patterns diverge. Both approaches produce patterns that oscillate around a similar mean value with similar bounds on the iteration distribution around that mean value. While the two approaches diverge in exact value as a function of iteration number, both approaches

share similar cyclical iteration histories about similar means with similar upper and lower bounds on the iteration oscillation. The similarity of the results between the two approaches reinforces the implementation fidelity of the optimization approach.

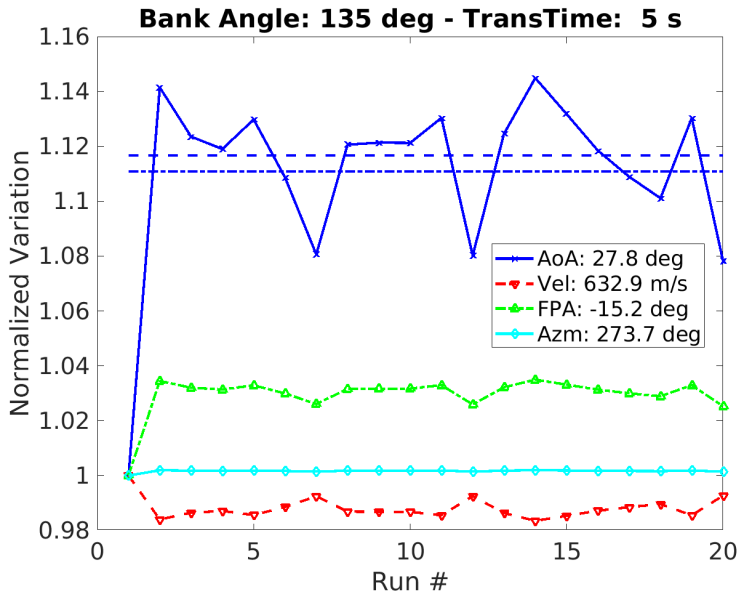

Figure 3.33: Methodology iteration histories for key flight dynamics parameters during a simulation of a 5 second transit trajectory with a 135 degree jettison bank angle . Parameters include debris angle of attack, terminal velocity, terminal flight path angle, and terminal azimuth angle. Each parameter history is normalized to its value at Run 1, which is reported in the figure legend. The outputs of one iteration are input as the initial guess for the next iteration.

The end-state uncertainty distribution trends validate the implementation of the transit trajectory simulation. The stable, bounded nature of the methodology iteration histories trend validates the implementation of the methodology cycle. The methodology results displayed in Figure 3.20 show minimum required angle of attack as a function of separation bank angle. The smooth trend between bank angles in the mean iteration history values further validates the implementation of the methodology. A smooth trend is established between variations in the input separation bank angle and the output required angle of attack to achieve minimum safe offset distance at the end of the transit trajectory duration.

Figure 3.24 displays the minimum required debris angle of attack as a function of transit trajectory duration. The established trend between simulation time and required angle

of attack further establishes trend validation of the methodology. As an additional check on the implementation of the methodology and the generated results, the trend shown in Figure 3.24 aligns with expectations based on intuition. As transit trajectory duration increases, more time is available to exert flight dynamic control over the debris using L/D and bank angle modulation and affect a difference in state between the debris and the PDV. Conversely, shorter transit times require achieving similar disparity between vehicle states with less time and therefore are expected to require higher flight dynamic performance to achieve this disparity.

3.10.5 Validation Conclusion

All verification activities indicate the model implementations are correct. Analytic calculations show that simulation outputs are in-line with expected outputs. The assumption that debris fields can be simulated from a high altitude and shifted lower in altitude in post-processing to approximate debris fields simulated from lower altitudes is shown to underestimate required debris trim angle of attack by a maximum of 3 degrees for the range of altitudes relevant to the present study. The 3 degree underestimate is on same order of magnitude as angle of attack variations between bank angle solutions for fixed transit times. Required debris trim angle of attack is considerably more sensitive to variations in transit time where a difference of 25 degree between transit times of 5 and 20 seconds is observed. Performance trends across bank angle variations and transit time variations are preserved. The assumption is deemed to make an acceptable trade between result fidelity and increased simulation speed.

3.11 Conclusions

From a high-level perspective, the methodology seeks to provide mission designers quantitative data about a proposed debris separation architecture to can be used to inform further mission architecture design and analysis, including competitively comparing a collection of

proposed separation architectures. The methodology meets this goal by establishing trends in required separation system performance across a range of representative flight conditions such that far-field recontact risk is constrained to a desired confidence level. The statistical and iterative approach to establishing these trends inherently assists in the self-validation of the methodology and the implementation of vehicle and flight models. Chaotic trends resulting from reasonable or expected variation on nominal input parameters would indicate errors in the module implementations. The trends presented in this body of work indicate smooth and intuitive responses to input perturbations and give evidence toward a trend validated methodology design and implementation.

CHAPTER 4
MULTI-FIDELITY MODELING OF INTERFERENCE AERODYNAMIC RESPONSES

4.1 Motivation

The present work is performed within the context of simulating the flight dynamics and performance of jettison architectures used for vehicle configuration transitions immediately prior to supersonic retropropulsion (SRP) initiation during human-scale Mars entry, descent, and landing sequences. More specifically this work focuses on jettisoning a 34 mT aeroshell from an 85 mT vehicle during descent to the Martian surface. Supersonic debris jettisons such as this are extremely computationally expensive to analyze due to the need for expansive interference aerodynamics databases. A single interference aerodynamic computational fluid dynamics (CFD) solution may require an order of magnitude more computation time than an equivalent isolated aerodynamic solution due to the increased grid size as well as the increased flow complexity. A full interference aerodynamic database may have upwards of 8 additional degrees of freedom as compared to an isolated database and therefore can require enormous quantities of data to fully populated a database needed for flight dynamic analysis.

The present study fits within the context of a larger study that develops a methodology for determining ejection subsystem performance requirements and approximate relative flight trajectories between ejected debris and a primary body by utilizing isolated aerodynamic data for initial approximations. As part of future improvements, the methodology will use a 1-dimensional interference aerodynamic database to update performance estimates along relative flight trajectories that were generated using isolated aerodynamics. In this modeling scenario, full isolated aerodynamic databases are available at the time inter-

Table 4.1: Flight Conditions at Separation

Event	Velocity, m/s	Flight Path Angle, $\deg$	Altitude, km
Transition Initiation	680	-10	8.8

ference aerodynamics data is being generated and modeled. Similarly, in many industry applications it is common to have access to isolated data prior to the development of interference aerodynamic data. The goal of the present study is to determine if interference aerodynamic model accuracy can be improved by incorporating isolated aerodynamic data into the interference modeling techniques.

4.2 Approach

4.2.1 Vehicle Jettison Architecture

This study adopts the entry vehicle architecture, jettison architecture, and entry trajectory put forth by NASA's Entry, Descent, and Landing Systems Analysis (EDLSA) study [4]. During descent, the hypersonic aeroshell is shed prior to SRP initiation. The jettison event is modeled as a clamshell separation, as depicted in Figure 3.2. The flight conditions at jettison initiation are reported in Table 4.1.

4.2.2 Aerodynamic Data Generation

NASA's Cart3D [70, 71] inviscid, Euler solver is used to generate isolated and interference aerodynamic data. Refer to Section 3.3.1 for discussion on the selection of this aerodynamics tool as well as assumptions made during its use. The data presented in this study is collected at Mach 3 at a ratio of specific heats, γ, of 1.285. Interference aerodynamics are generated with a fixed spacing between the primary vehicle and the two pieces of ejected debris. The primary vehicle is held constant at 0 degrees angle of attack while the symmetric debris are rotated through angles of attack 0 to 360 degrees in 15 degree increments. Sideslip angle is held constant at 0 degrees. The debris are located downstream of

the primary vehicle at an axial distance of 35 meters and a radial distance of 25 meters. Positioning and debris rotations are symmetric and mirrored.

In order to decrease the CFD simulation complexity and computation time, significant simplifications are made to the database geometry models. These simplifications allow more effort and time to be directed toward the multi-fidelity modeling aspect of the study rather than the data generation. CFD simulations are run with the same geometry representing the primary vehicle and the debris. This geometry is a 10x30 meter ellipsled. Figure 4.1 shows an example flow solution run for this study. The flow solution is composed of three bodies (all modeled by the 10x30 meter ellipsled) in proximity - the forward body represents the primary descent vehicle and the two aft bodies represent debris from the clam-shell jettison. Interference aerodynamic data referenced in this study is for one of two downstream debris bodies.

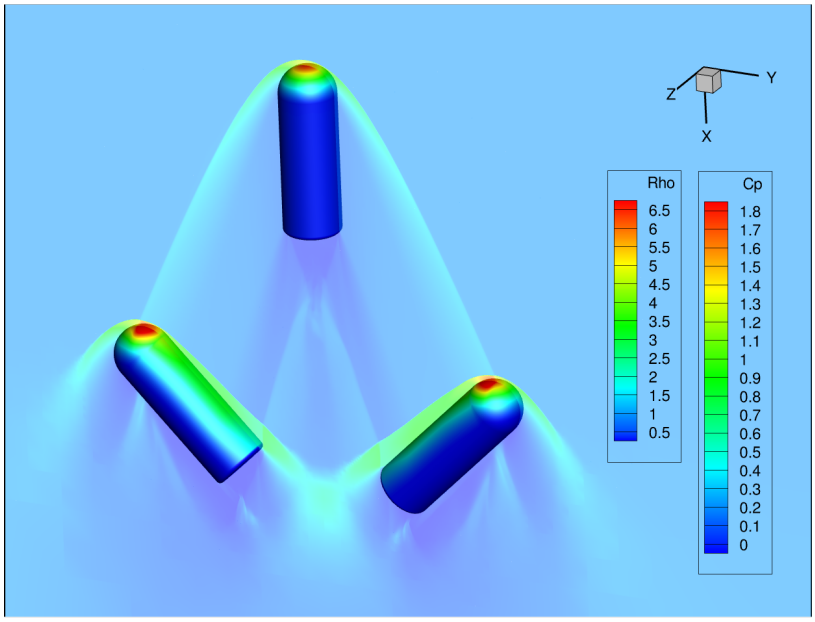

Figure 4.1: Example CFD solution of the hinged-exit transition architecture. One forward body represents the primary descent vehicle and two aft bodies represent the symmetric halves of the shed aeroshell. The flow color shows density variations. Body surface colors show pressure coefficient variations.

4.2.3 Multi-Fidelity Modeling

Background

As used in the present work, the term ”model” describes a mathematical or empirical relationship between one or more input parameters and a desired output parameter. A model allows an investigator to determine a phenomena response solely based on knowledge of input parameter values and tuned model settings.

Multi-fidelity models leverage abundant inexpensive, or cheap, low-fidelity simulation data and sparse expensive high-fidelity data to achieve a desired level of high-fidelity model accuracy while reducing the overall experimental or computational expense. Fernández-Totalino et al. [72] provides a comprehensive survey of multi-fidelity modeling and its application to science and engineering surrogate modeling tasks. Multi-fidelity models (MFM) excel when applied to problems where a high-fidelity surrogate model is required but high-fidelity simulations or experiments are too expensive to generate enough data to properly train a surrogate model.

Multi-fidelity models have been applied to a wide range of engineering applications. Fernández-totalino et al. [72] categorizes multi-fidelity applications according to the type of fundamental difference between the high-fidelity and low-fidelity simulations used. Three broad categories of fidelity difference include differences in mathematical model or physical reality, simulation resolution (e.g. discretization, convergence level), and simulation vs experimental data.

Many examples of multi-fidelity models may be found in computational fluid dynamics research. MFMs have been successfully applied to differences in discretization, convergence level, physics assumptions (e.g. Reynolds-averaged Navier-Stokes equations vs Euler inviscid equations), and experimentation versus simulation data. The applicability of MFM is highly problem dependent and the usefulness must be determined based on the specific problem, dimensionality, and fidelity differences. The goal of the present

study is to determine the applicability and usefulness of multi-fidelity modeling techniques to model expensive interference aerodynamic response by leveraging lower-cost isolated aerodynamic response data as lower-fidelity approximations.

Types of Multi-Fidelity Models

Three types of multi-fidelity model structures are widely used. Additive models generate HFM as the sum of a LFM and an additive correction term. The additive model may be expressed as,

$$\hat{f}_e = f_c(\boldsymbol{x}) + \delta(\boldsymbol{x}), \tag{4.1}$$

where $\hat{f}_e$ is an estimator of a surrogate model trained on expensive data, $f_c(\boldsymbol{x})$ is a surrogate model trained on cheap data, and $\delta(\boldsymbol{x})$ is an additive correction surrogate model trained on the difference data, δ, between the high-fidelity (expensive) data, y_e, and the low-fidelity (cheap) data, y_c, as define in Eq. 4.2.

$$\delta = y_e - y_c \tag{4.2}$$

Similarly, multiplicative models given by Eq 4.3 generate the HFM as the product of the LFM and a multiplicative correction term, $\rho(\boldsymbol{x})$.

$$\hat{f}_e = \rho(\boldsymbol{x}) \cdot f_c(\boldsymbol{x}). \tag{4.3}$$

$\rho(\boldsymbol{x})$ is a surrogate model trained on multiplicative data, ρ, of the form,

$$\rho = \frac{y_e}{y_c} \tag{4.4}$$

Comprehensive models combine features of both additive and multiplicative models

and are expressed as,

$$\hat{f}_e = \rho(\boldsymbol{x}) \cdot f_c(\boldsymbol{x}) + \delta(\boldsymbol{x}). \tag{4.5}$$

Study Implementation

The present study utilizes additive models as described by Equation 4.1. The modeling process for both single and multi-fidelity models is diagrammed in Figure 4.2. As a note, both single- and multi-fidelity models are modeling the same interference aerodynamic response - the goal of the study is to determine if the multi-fidelity modeling process produces a better model than the single-fidelity modeling process. A diagram of the single-fidelity modeling process is illustrated along the right-side of Figure 4.2. Expensive data, D_e is fit by a Gaussian Process Regression (GPR) function to generate a surrogate model of the interference aerodynamic response. This surrogate model serves as the single-fidelity model of the interference aerodynamics. The multi-fidelity model is illustrated along the left-side of Figure 4.2. Two types of data are used in the modeling process, cheap data (D_c) and difference data (D_δ). Difference data is taken to be the difference between cheap and expensive data. Each data set, D_c and D_δ, is fit with a GPR model to create surrogate models of the cheap and difference data. The multi-fidelity model of the expensive data is taken to be the sum of the cheap and difference surrogate models.

This study uses Gaussian Process Regression functions to fit data. In practice, any type of function can be used to fit the data. Gaussian Process Regression functions are described in Section 4.2.4.

4.2.4 Gaussian Processes

This study constructs surrogate models using Gaussian Process Regression (GPR) models. Model generation utilizes Matlab's built-in implementation of Gaussian Process Regression models [73] which follows the ubiquitous treatment by Rasmussen [74]. GPR models are implemented with standardized input data. A squared exponential covariance kernel is

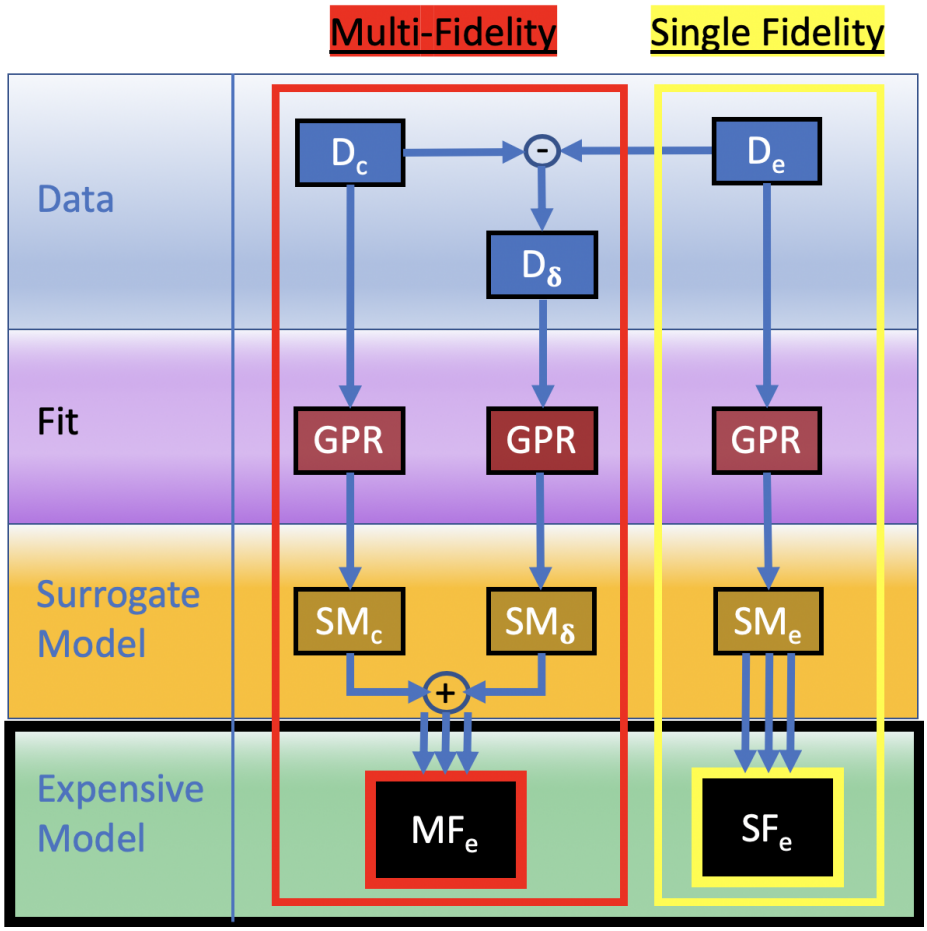

Figure 4.2: Diagram showing the flow of data through single- and multi-fidelity modeling processes.

used. Hyperparameters σ_L and σ_F are optimized through a maximum likelihood process. σ_L is the characteristic length scale of the 2-norm distance between design points. Initial guesses for σ_L and σ_F are determined based on the the spacing between between the design points and the response data, respectively. The formula for the initial guess of σ_L is given by Eq. 4.6.

$$\sigma_L = \frac{\max(diff(x_{in}))}{\frac{(\max(x_{in}) - \min(x_{in}))}{length(x_{in})}} \tag{4.6}$$

x_{in} is a 1-dimensional input array of design points. σ_F is tuned in the same manner as σ_L, with the exception that σ_L operates on the vector of design points, x_{in}, while σ_F

operates on the responses, $y(x_{in})$.

4.2.5 Design of Experiments

A non-conventional, randomized, Monte Carlo style design of experiments is used for selecting training data for individual designs. An individual design is defined to be a unique set of training data for which a GPR model is built upon. The present study considers a 1-dimensional design space between 0 and 360 degrees angle of attack. The number of points to include in a training data set for an individual design is governed by an inclusion ratio, r, defined as the ratio of selected training points, n_T, to total points available from the full set, N_F. This study looks at designs with inclusion ratios between 0.2 and 1. The full data set in this study consists of 25 interference aerodynamic data points distributed in 15 degree increments.

At each inclusion ratio, N_S designs are generated by randomly selecting $n_T = r \cdot N_F$ points for each design according to the following heuristic. The two data points at the boundary of the feasible design space (0 and 360 degrees) are always selected for inclusion in the training set. Then, $(n_T - 2)$ points are randomly selected from the remaining full set of data for inclusion in the training set. For example, at an inclusion ratio of 0.6, the two data points at 0 and 360 degrees are automatically added to the training set. Then, 13 additional data points are randomly selected for inclusion in the training set, bringing the total number of training points to 15. This process would be repeated N_S times to generate a set of N_S designs at an inclusion ratio of 0.6. The theoretical total possible number of designs, n_D, is given by,

$$n_D = \frac{(N_F - 2)!}{(N_F - r \cdot N_F)!\,(r \cdot N_F - 2)!} \tag{4.7}$$

A quality control measure is implemented to ensure reasonable spacing between design points and throw out designs with large point concentrations in one area and large point voids in other areas. The maximum spacing between any two adjacent design points is

not permitted to be larger than 1.75 times the average spacing between all adjacent design points. Similarly, the minimum spacing is constrained to be no less than 0.35 times the average spacing between all adjacent design points. The maximum and minimum multipliers are chosen based on investigating which values produce suitable point distributions. The number of studies, N_S, run at each inclusion ratio is selected to be large enough as to capture the distribution of validation metrics for the span of possible designs. In the present study, this number is set to 200.

4.2.6 Validation

K-fold cross-validation is used to determine the root-mean-squared-error (RMSE) fitness of models. K-fold validation randomly distributes p points into k bins. In turn, a specific bin of points is selected as "in-fold" points while all other points are grouped into "out-of-fold" points. A transient model is generated based on the out-of-fold training points, from which the RMSE is calculated as Equation 4.8 using the in-fold validation points. The term "transient model" is used to signify that a model is generated for a subset of training data but that model is only used behind the scenes for validation purposes. This process is repeated k times such that each bin in turn becomes the in-fold points. The k bin RMSE values are then averaged to determine the k-fold cross-validation error, CVE, according to Equation 4.9. K-fold cross-validation is widely used in literature [75, 76] to evaluate the fitness of a model. Fit models are defined as those with the lowest cross-validation error.

$$RMSE_{(j)} = \sqrt{\frac{1}{n}\sum_{i=0}^{n} e_{(i)}^2} \quad \text{, where} \quad e = (y^{(i)} - \hat{y}^{(i)}) \tag{4.8}$$

$$CVE = \frac{1}{k}\sum_{j=0}^{k} RMSE_{(j)} \tag{4.9}$$

In addition to k-fold cross-validation, total validation is reported throughout this study for comparison purposes and to obtain greater insight into modeling errors. Total validation

uses the response data not included in the design training set to generate a RMSE validation metric. If response data is assumed to represent the ”truth” of a process, then given enough data, total validation is the best approximation of the model error in the absence of true knowledge of the underlying process. In practice, total validation is not possible, as its calculation requires either exact prior knowledge of the underlying phenomena or extra data points not available to the modeling process. In practical scenarios, the functional form of the underlying phenomena is not known a priori and any available data is used to train and validate a model.

Cross-validation is shown to be a reasonable predictor of total validation under certain conditions [77]. However, cross-validation is more directly a measure of model susceptibility to error when data is removed. Conceptually, it is an approximate measure of the derivative, or rate-of-change, of model error as data is added or removed. A model with an over-saturation of data relative to the true variability of the underlying phenomena is resilient to data reduction and therefore has a low cross-validation error. A model with a sparse set of data is very sensitive to data reduction and therefore has a high cross-validation error.

This metric serves as a reasonable model error estimate as the rate of change in the model error correlates with total error in many instances [77]. A model that is well defined due to high data saturation is resilient to data reduction (low cross-validation error) but also accurately captures the underlying phenomena and has a low total error. A model that is sparsely populated has a susceptibility to data reduction (high cross-validation error) but likely lacks sufficient information to capture the underlying phenomena trends and therefore has higher total error. This argument assumes the training data is error free. The idea of sparseness and data saturation is a relative concept dependent on the natural variability of the underlying process or phenomena.

4.3 Results

Designs are evaluated across 7 inclusion ratios, r, ranging from 1 to 0.24. At each inclusion ratio, 200 designs are evaluated to capture the distribution of validation error across the set of possible designs.

4.3.1 Analysis of a Single Design

An example of a single design is shown in three plots in Figure 4.3. The first plot shows the GPR surrogate model of the delta data given by Eq. 4.2. The second plot shows the isolated aerodynamics and multi-fidelity interference aerodynamics GPR models. The third plot shows the single-fidelity interference GPR model. On all plots, the training data is signified by square data points, the full set of available data is signified by star data points, GPR fit models are signified by solid blue lines, cross-validation predictions at training points are illustrated by magenta upright triangles and connected by magenta dashed lines, and isolated GRP models (only shown in the second plot) are signified by dot-dashed green lines. Magenta dashed lines do not indicate any assumptions about cross-validation predictions between data points and are only used to aid visualization of the validation data points themselves. Validation metrics are shown in the titles of the top and bottom plots. It should be noted that the validation metrics for the delta GRP model are also the validation metrics for the MF GPR model as the isolated GPR model is assumed to have no associated error contributions to the multi-fidelity model. Due to this assumption, the total validation error of the MF model is absorbed into the delta GPR model.

A design consisting of 11 training data points spaced between 0 and 360 degrees angle of attack is shown in Figure 4.3. The delta GPR model (Plot 1) does a reasonable, though imperfect, job of capturing the drag coefficient difference-data trend. The multi-fidelity cross-validation error is 0.07 compared to a drag coefficient range between 1.0 and 4.5. The single-fidelity GPR model (Plot 3) also does a reasonable job of capturing the inter-

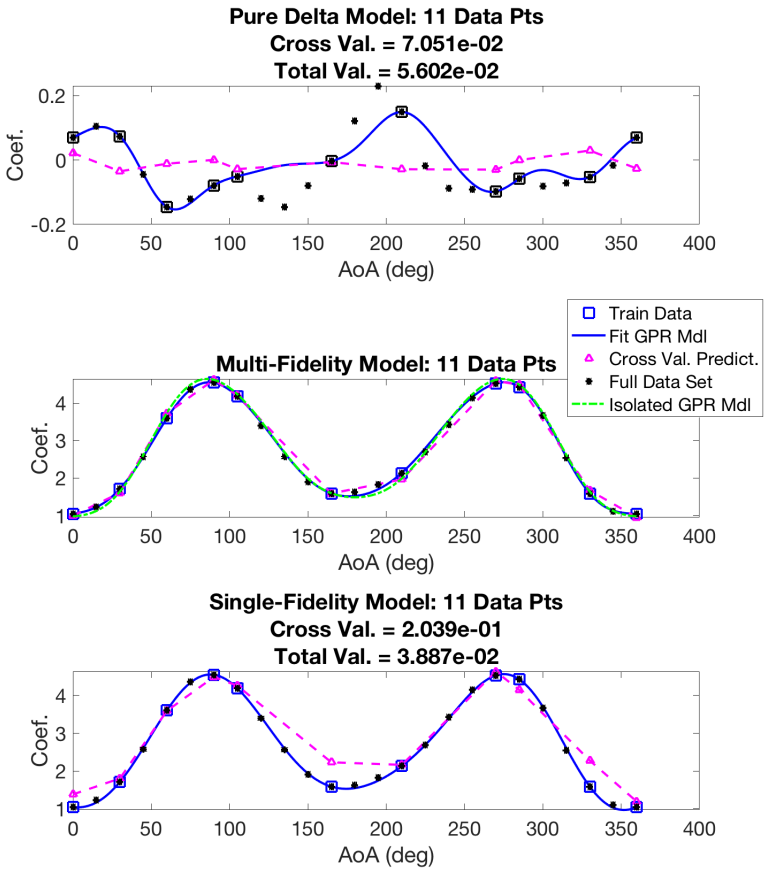

Figure 4.3: Analysis of an 11-point design. Plot 1 shows the delta GPR model. Plot 2 shows the multi-fidelity interference aerodynamic GPR model and isolated aerodynamic GPR model. Plot 3 shows the single-fidelity interference aerodynamic model.

ference aerodynamics trend with a cross-validation error of 0.2. The cross-validation error shows that the multi-fidelity model is more resilient to error-due-to-data-reduction than the single-fidelity model. The total validation shows the single-fidelity model slightly outperforms the multi-fidelity model for this design; however, the difference in total RMSE is approximately 0.017, which is negligible compared to the drag coefficient range.

4.3.2 Comparison of Multiple Designs at a Single Inclusion Ratio

Three different designs each consisting of 6 training data points are shown in Figures 4.4, 4.5, and 4.6. A design is shown in Figure 4.4 for which both the multi-fidelity and single-

fidelity models predict the true response fairly well. In Plot 1, the delta GPR model predicts the general trends of the delta data but fails to capture all peaks and valleys. In Plot 2, the multi-fidelity model predicts the interference aerodynamics well. The isolated aerodynamics track the interference aerodynamics very closely, indicating they are a reasonable predictor of bulk interference aerodynamic trends. Comparison of validation metrics show the multi-fidelity model performs an order of magnitude better in cross-validation and a factor of 3 better in total validation. Even though the delta GPR model misses much of the curvature of the true difference response, it still outperforms the single-fidelity model.

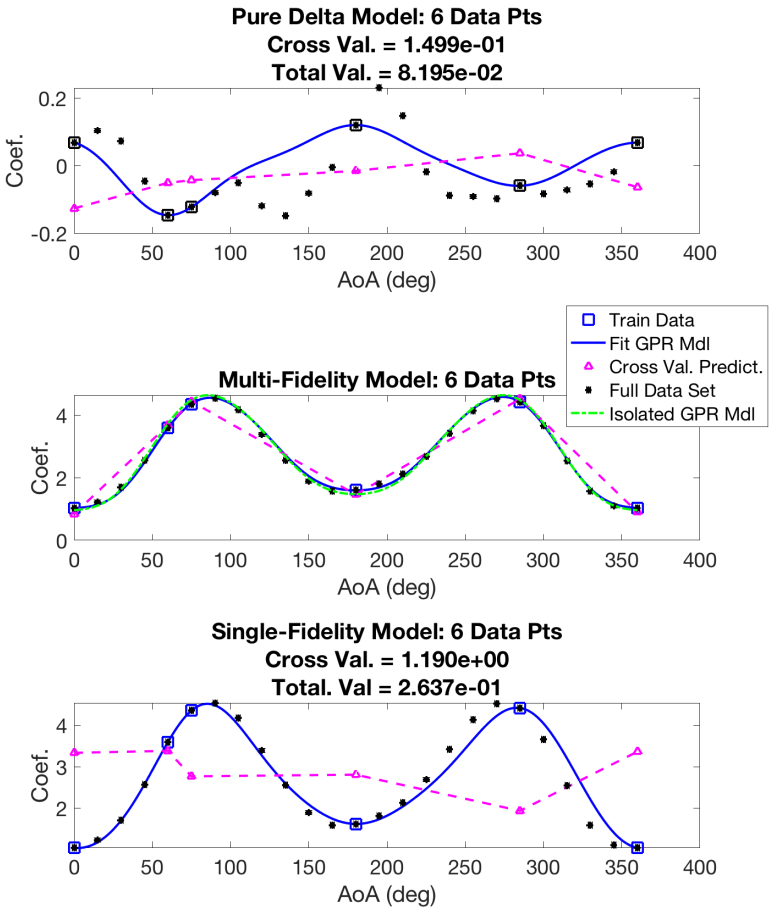

Figure 4.4: Comparison of multi-fidelity modeling technique against single-fidelity surrogate modeling technique. Six data points are used to train the surrogate models in this Example Design 1.

A 6-point design is shown in Figure 4.5 with a different distribution of training data than the design in Figure 4.4. The delta model again misses to capture all of the natural curvature of the full set of difference data but captures different peaks and valleys than the design in Figure 4.4. Compared to the previous design, the delta model outperforms in both total and cross-validation metrics. While the difference in multi-fidelity model performance between Figures 4.4 and 4.5 is mostly benign, the difference in single-fidelity model performance is significant. The total validation error jumps by 500% versus the 12% increase in the multi-fidelity error. This design demonstrates the single-fidelity modeling approach is significantly more sensitive to changes in training data distribution than the multi-fidelity approach.

A third 6-point design is shown in Figure 4.6 on which the the multi-fidelity model performs the worst out of the three designs discussed. The delta model misses most of the curvature of the full set of data. The single-fidelity model captures the inflections of the full data set but misses the peaks and valleys. The MF model out-performs the SF model by a factor of 5 in total validation error and a factor of 15 in cross-validation error.

Three designs are shown in Figures 4.4, 4.5, and 4.6 with varying levels of success for each of the multi-fidelity and single-fidelity models. The least successful multi-fidelity model performs better than the most successful single-fidelity model with a total validation error difference of 1.6e-1. The range of total validation error between the best and worst multi-fidelity model is 2.3e-2. The total validation error range for the single-fidelity models is 7.6e-1. For designs with sparse amounts of expensive training, single-fidelity models perform worse than multi-fidelity models and have greater variability in validation error performance.

Isolated aerodynamic GPR models (dot-dash green line) track interference aerodynamic data very closely in Plot 2 of Figures 4.3, 4.4, 4.5, and 4.6. In Plot 1, delta data magnitude is on the order of 5-10% of the interference data. At the flight conditions over which the study data was generated, isolated aerodynamic drag coefficient data approximates interference

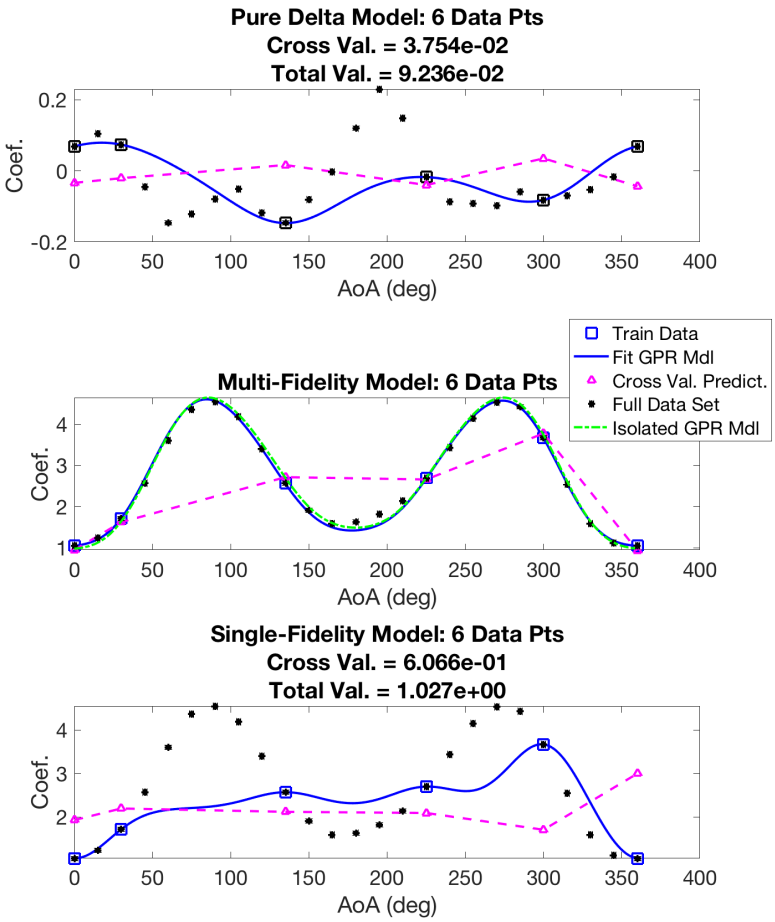

Figure 4.5: Comparison of multi-fidelity modeling technique against single-fidelity surrogate modeling technique. Six data points are used to train the surrogate models in this Example Design 2.

data by 95%.

In the framework of multi-fidelity modeling, cheap data (isolated aerodynamics) is assumed to significantly outnumber expensive data (interference data). As a consequence, the cheap surrogate model is typically very well defined. If the difference in response between the cheap data and the expensive data is very small, it follows that a multi-fidelity model would perform much better than a single-fidelity model for small amounts of available expensive data. For the design in Figure 4.3, any errors in the delta model are only propagated on a scale of 5-10% in the mulit-fidelity interference GPR model, whereas er-

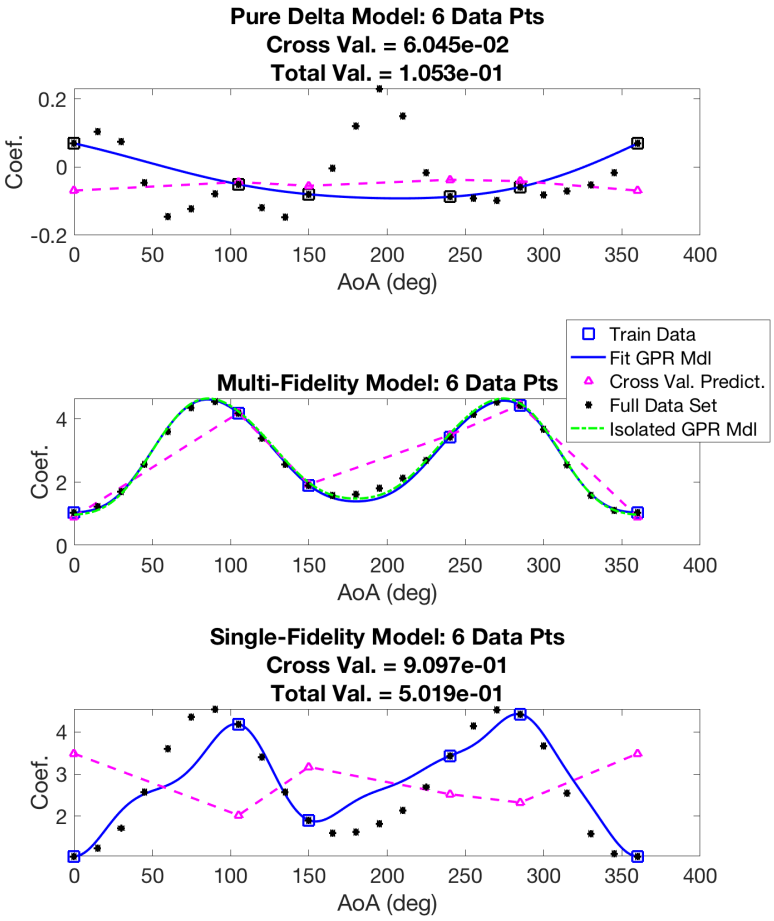

Figure 4.6: Comparison of multi-fidelity modeling technique against single-fidelity surrogate modeling technique. Six data points are used to train the surrogate models in this Example Design 3.

rors in the single-fidelity model are directly realized at 100%. Intuitively, as the number of expensive points decreases, the accuracy of multi-fidelity model approaches the cheap model accuracy, whereas the single-fidelity model accuracy approaches zero. The trends in Figure 4.7 confirm this intuition.

4.3.3 Validation Error Trends in Single- Vs. Multi-Fidelity Models

Validation error versus the number of expensive points in the model is presented in Figure 4.7 over four plots for 1400 designs. An example of a single design is shown in Figure 4.3.

Inclusion ratio, r, is displayed along the x-axis of Plots 1-4 in Figure 4.7. Cross-validation error is shown on the y-axis in Plots 1-2. Cross-validation data variance is shown in Plot 3. Total validation error is shown in Plot 4. For reference, all designs in this study utilize 25 cheap points (isolated aerodynamics) spaced in 15 degree increments across the design space and select expensive training data from a pool of 25 possible expensive points. Multi-fidelity cross-validation error trends shown in Plot 1 are isolated in Plot 2 in order to provide a clearer view. Each inclusion ratio is sampled at 200 randomized designs. Multi-fidelity data is indicated by a blue diamond. Single-fidelity data is indicated by a red plus-sign. The dashed lines connect the mean values across inclusion ratios for their color-respective models; the lines do not convey any assumptions about predictions between data points and are for enhancing visualization of data points only.

In Plot 1 of Figure 4.7, the single-fidelity cross-validation error is approximately an order of magnitude larger than multi-fidelity cross-validation error at low inclusion ratios, $r < 0.52$ (13 expensive points). For $r > 0.52$, the performance difference between single- and multi-fidelity models becomes negligible. The variances in Plot 3 show multi-fidelity models have more consistent performance than single-fidelity models at low inclusion ratios. The total validation metrics in Plot 4 are consistent with the trends in Plots 1-3.

It must be noted across all inclusion ratios there are specific designs for which single-fidelity models perform within the performance range of multi-fidelity models. These designs represent outliers of the population of feasible designs as seen from the mean trend lines in Plots 1-2 and the variances in Plot 3. Additionally, these individual designs benefit from luck that the data points randomly included in the designs are well placed to capture the trends. Without a priori knowledge of a phenomena, such data placement within a design can not be guaranteed. The mean and variances of the populations at each inclusion ratio are much better predictors of expected performance.

The trends in Figure 4.7 have several dependencies worthy of discussion. In constructing a multi-fidelity model, it is assumed no more can be learned from cheap data at a point

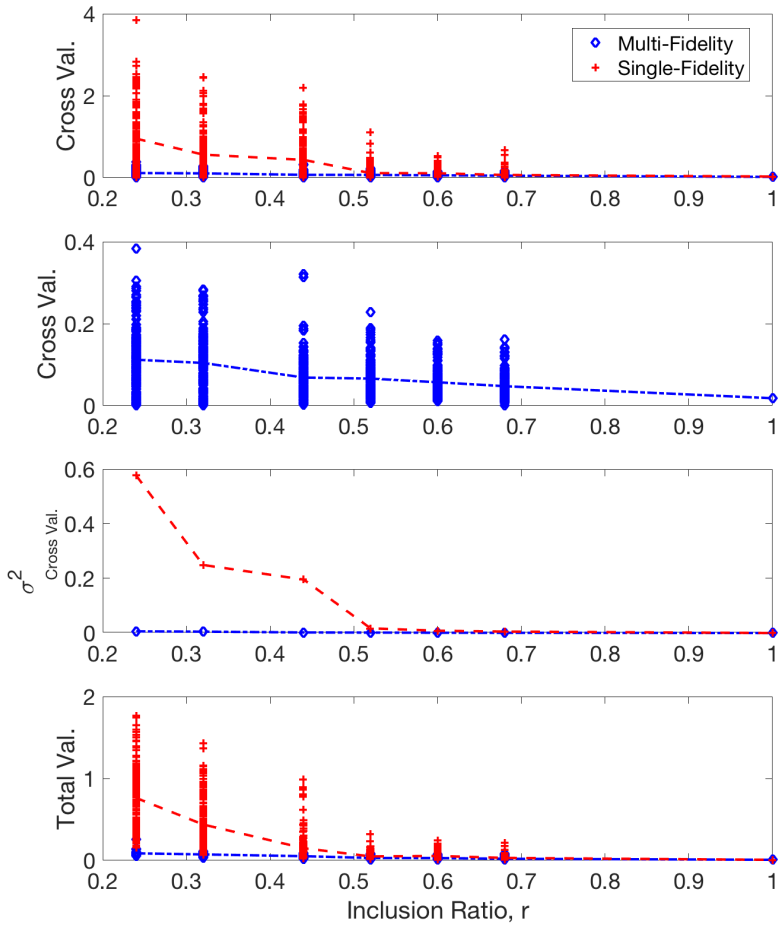

Figure 4.7: Validation metric trends across inclusion ratio for single- and multi-fidelity models.

where expensive data is available [78]. When the inclusion ratio is 1, expensive data is available everywhere that cheap data is. Therefore, the multi-fidelity modeling approach has no extra information to leverage over the single-fidelity approach. At this condition, it is expected (and verified in Figure 4.7) that the performance of both models converge.

The point at which multi-fidelity and single-fidelity performances diverged depends on the number of points included in the design rather than the inclusion ratio. When the amount of expensive data in a design fully saturates the natural variability of a phenomena, the performance of the two modeling methods converges irrespective of the amount of

cheap data in the design (and thus the inclusion ratio). In practical applications, expensive data is rarely abundant for the very reason that it is expensive to calculated and the design space is only sampled sparingly. As this condition breaks down, so too does the motivation for using multi-fidelity modeling techniques.

Standard deviation of individual model error for the expensive multi-fidelity model (MFM), expensive single-fidelity model (SFM), and cheap single-fidelity model is displayed in the top plot of Figure 4.8. A zoomed in view of expensive MFM data is presented in the bottom plot of Figure 4.8. For small inclusion ratios, the cheap SFM shown in green achieves a standard deviation of error (StdE) magnitude that is a factor of 7.5 lower than the expensive SFM StdE shown in red. The StdE of the cheap SFM is constant across all inclusion ratios because it always uses the same 25 points. Expensive MFM StdE converges to the cheap model StdE for low amounts of data (low inclusion ratio). For increasing amounts of training data, the expensive MFM has lower StdE (better performance) than the cheap SFM. Both the expensive MFM and expensive SFM perform better than the cheap SFM after an inclusion ratio of 0.5.

The cheap SFM has a StdE of 0.1 and is a very good predictor of the expensive data. Due to the construction of an additive MFM, the expensive MFM reverts to the cheap SFM for small amounts (or zero) expensive training data. The StdE of the cheap SFM intrinsically defines the approximate upper limit of StdE for the expensive MFM - though it is possible with some models (particularly at low inclusion ratios) to perform worse than the cheap SFM. This behavior is observed in Figure 4.8. As the inclusion ratio approaches 0, the StdE of the expensive MFM converges with the cheap SFM. For the spatial arrangement of bodies in the CFD simulations (as depicted in Figure 4.1) used in the present study, the significant performance improvement of the expensive MFM over the expensive SFM can in-part be attributed to the excellent performance of the underlying cheap SFM. However, the expensive MFM StdE is lower than the cheap SFM StdE, indicating the expensive MFM improves upon the performance achieved by the cheap SFM.

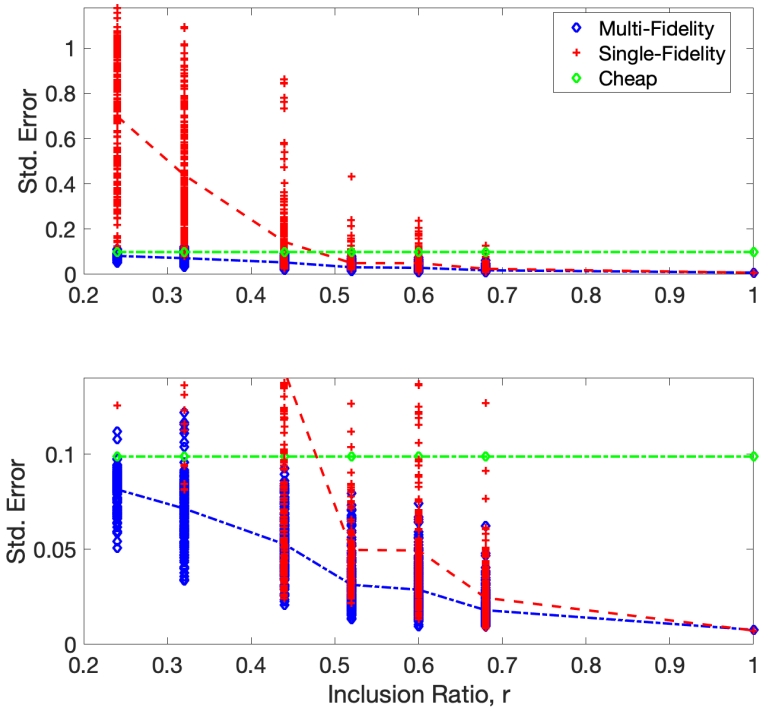

Figure 4.8: Standard deviation of error trends across inclusion ratio for single-fidelity, multi-fidelity, and cheap models.

At inclusion ratio 0.24, the expensive SFM StdE is a factor of 7.5 larger than the cheap StdE and the expensive MFM is nearly converged with the cheap StdE. This scenario shows the model sampling density is likely insufficient to appropriately capture the trends of the underlying phenomena as the expensive SFM fails to capture the trend (high StdE) and the expensive MFM relies almost entirely on the cheap SFM to achieve its increased performance. At high inclusions ratios, the performance of both expensive MFM and expensive SFM converge. A regime of interest occurs between inclusion ratios 0.35 and 0.55. Below this regime, the sampling density is too low to incorporate the effects of expensive data in either the expensive SFM or MFM. Above this regime, the sampling density is high enough that the performance difference between expensive SFM and MFM diminishes. Within this regime, the underlying phenomena is sparsely sampled and MFM techniques provide a performance improvement over standard SFM techniques.

Multi-fidelity modeling is useful when three conditions are satisfied:

- Cheap data provides some meaningful measure of the expensive data,
- Expensive data is only sparsely available across the design space,
- Cheap data is more abundant than expensive data.

4.4 Conclusions

The goal of this study is to determine whether multi-fidelity modeling techniques are suitable for predicting interference aerodynamics by leveraging low-fidelity isolated aerodynamics as approximations. The suitability of multi-fidelity modeling is considered confirmed if the technique can either improve the accuracy of a model for a given set of expensive data or reduce the necessary amount of data to achieve a desired model accuracy. This study utilizes data obtained from computational fluid dynamics simulations using NASA's Cart3D for three identical bodies, one primary upstream body and two bodies symmetrically located 35 meters downstream and 25 meters off-axis of the primary body. The downstream bodies are rotated through 0 to 360 degrees angle of attack while the upstream body remains fixed at 0 degrees angle of attack. Data presented in this study is collected for one of the two downstream bodies under the influence of the fluid flowfield wake of the primary upstream body.

This study concludes that isolated aerodynamics provide a useful approximation of interference aerodynamics and enable the use of multi-fidelity modeling to improve the accuracy of interference aerodynamics models for a given set of data as compared to single-fidelity modeling techniques. Across all inclusion ratios, multi-fidelity models perform better than or equal to single-fidelity models. A multi-fidelity model utilizing 6 expensive data points (r = 0.24) performs as well as a single-fidelity model utilizing 13 data points (r = 0.52), with both models achieve a cross-validation error metric of 0.112. Multi-fidelity

modeling is suitable for achieving a desired model accuracy while utilizing less expensive data points.

CHAPTER 5
CONCLUDING REMARKS AND FUTURE WORK

5.1 Concluding Remarks

This dissertation puts forth a methodology to determine required separation subsystem performance for human-scale supersonic descent jettison maneuvers. The work addresses a gap in current analysis capability to quantitatively competitively evaluate a variety of proposed supersonic vehicle staging architectures to determine a subset of fittest candidates for further detailed investigation. In the present work, the methodology is demonstrated on a 10x30 meter ellipsled entry vehicle utilizing a symmetric clam-shell supersonic aeroshell jettison maneuver. At the time of this dissertation publication, there exists no published work on descent supersonic staging. As a supplement to the methodology research, multi-fidelity modeling techniques are evaluated for applicability toward generating surrogate models of expensive interference aerodynamic responses by leveraging available inexpensive isolated aerodynamic data.

The methodology operates on both a micro and macro level. For a proposed separation architecture, the methodology micro level focuses on evaluating system performance for a single case, consisting of specified transition initiation flight conditions, transition time, and separation bank angle. The methodology iterates until a feasible, converged solution is achieved. The solution consists of required debris angle of attack and center of gravity thrust performance to mitigate far-field recontact risks. Such a solution will indicate whether a proposed jettison architecture is achievable using aerodynamic debris control alone or if thruster impulse is required to satisfy far-field recontact risk requirements. In many cases, the methodology identifies a solution withing 5% of a converged feasible solution in as few as 2 iterations. A converged, feasible mean solution is identified in as few

as 5 iterations.

In addition to evaluating required subsystem performance necessary to perform a specified jettison architecture, the methodology also serves a risk mitigation tool. Embedded in the methodology subroutines is the ability to specify what level of far-field recontact risk is acceptable. This risk tolerance may be modified to serve different mission constraints or designs.

On a macro level, the methodology is highly automated. For as much effort as a user would put into generating a single solution, an entire set of feasible designs can be generated for a range of transition times and separation bank angles. The automated nature of methodology enables a user to construct phase diagrams of optimal aerodynamic and thruster performance versus separation bank angle for a single transition time and optimal debris performance versus transition time. These phase diagrams provide crucial information to mission designers, enabling them to not only solve a single design point but also perform trade studies on a vehicle and descent mission architecture.

The field of supersonic descent jettison maneuvers suffers from a complete lack of literature on the topic. As such, no suitable data is available to validate the methodology against. In lieu of a data-driven validation campaign, a series of verification checks are performed on the different modules that comprise the full methodology. Checks are performed to ensure observed energy exchange and vehicle accelerations match expected values determined through independent analytic and modeling activities. Several simplifying assumptions are checked for validity against more time-intensive, rigorous analysis approaches.

Multi-fidelity modeling techniques were found to improve the accuracy and k-fold cross-validation metrics of interference aerodynamic drag coefficient models as compared to single-fidelity modeling techniques. Multi-fidelity modeling techniques performed particularly well for models built from sparse sets of interference data. The study utilizes data obtained from computational fluid dynamics simulations using NASA's Cart3D for

both isolated aerodynamics of a piece of ejected debris and interference aerodynamics of a debris in a configuration representative of a supersonic jettison maneuver.

5.2 Recommendations for Future Work

The goal of the present work is to prove out the initial methodology ideas and establish a baseline working methodology framework. In order to speed up analysis and expedite the initial feasibility exploration tasks, many simplifying assumptions were made. Recommendations are put forth for follow-up work to increase the fidelity of the simulation while still striking a balance with simulation speed in-line with the intended use for high-level, rapid analysis.

Transition initiation points were taken from NASA's EDLSA Architecture 1 study. Architecture 1 assumed the primary vehicle underwent a 20 second free-fall during the transition event. This assumption was believed to be a conservative estimate of flight dynamic performance and was used in place of detailed flight dynamic analysis of the transition event. As a natural next step for this research, the methodology should be used to study the effects of the transition event on the full EDL trajectory profile. Trades should examine the benefits of earlier or later transition initiation events and feed these impacts into the full mission architecture optimization.

The primary descent vehicle is assumed to be in aerodynamic free-fall during the transition event and does not ignite its propulsive descent engines until the end of the transition event. A study should investigate the feasibility of turning the descent engines on during the transition event (or after a specified time delay) and the effects of early ignition on offset distance requirements from the tumbling debris field.

The methodology was developed assuming the debris is the only body performing an active divert maneuver during the transition event. This assumption was made for several reasons. First, active diverts of primary descent vehicles have been extensively studied in the literature. As such, incorporating a primary vehicle active divert maneuver in the

present study was determined to have a poor return with respect to the amount of time required to implement such a maneuver versus the advancement to the state of the art it would yield. Second, and more importantly, due to the complex and chaotic interference aerodynamic interactions between a primary vehicle and a shed piece of debris, the jettisoned aeroshell would likely require an active separation system such as separation booster motors or aerodynamic flaps. A decision was made to determine the performance requirements of these on-board separation subsystems necessary to handle the entire aeroshell jettison divert maneuver. Debris-only divert maneuvers have not been extensively studied in the literature. Building the methodology to hand debris-only divert maneuvers is seen as a necessary stepping stone to eventually incorporating dual diverts - consisting of both a primary vehicle divert and active debris divert. Such a maneuver is anticipated to be the optimal transition solution.

The methodology currently considers the separation subsystem performance required to mitigate far-field recontact risks due to a single piece of jettisoned debris. Many proposed aeroshell jettison architectures require jettisoning 2 or more distinct pieces. For example, the clam-shell jettison architecture studied in-line with the development of the methodology requires jettisoning the aeroshell as two symmetric pieces. Currently, the methodology provides quantitative metrics that can be used in making design-level decisions, such as how to best eject 2 pieces of debris simultaneously, but these decisions must be made by a mission designer outside of the methodology framework. Future work could explore techniques to standardize the handling of simultaneous jettisons internal to the methodology. This would included assessing the feasibility of any proposed jettison architectures or flight conditions from a multi-jettison perspective.

The influence of interference aerodynamics between two similar-sized bodies in a supersonic flow can cause significant perturbations to each body's flight trajectory. The methodology should be extended to investigate the interference aerodynamic effects on required separation subsystem performance. The multi-fidelity modeling contribution of this

thesis is a step in this direction. Interference aerodynamics are computationally expensive. The methodology should be extended to use isolated aerodynamics results to predict a flight trajectory along which interference aerodynamics can be populated. The approach used in the multi-fidelity modeling contribution could be used to reduce the required density of the interference aerodynamic database while still maintaining the aerodynamic surrogate model fidelity.

REFERENCES

[1] D. Blette and R. D. Braun, "Supersonic Vehicle Configuration Transitions to Enable Supersonic Retropropulsion During Mars Entry, Descent, and Landing," *2016 IEEE Aerospace Conference*, 2016.

[2] B. G. Drake, S. J. Hoffman, D. B. Conference, IEEE, and 2010, "Human exploration of Mars, design reference architecture 5.0," *ieeexplore.ieee.org*,

[3] A. Cianciolo, J. L. Davis, D. R. Komar, and M. M. Munk, *Entry, Descent and Landing Systems Analysis Study: Phase 1 Report*, 2010.

[4] A Dwyer-Cianciolo, J Davis, and J Shidner, "Entry, descent and landing systems analysis: exploration class simulation overview and results," *AIAA/AAS Astrodynamics* . . ., 2010.

[5] D. R. Williams, *Earth Fact Sheet*, Sep. 2016.

[6] R. D. Braun and R. M. Manning, "Mars Exploration Entry, Descent, and Landing Challenges," *Journal of Spacecraft and Rockets*, vol. 44, no. 2, pp. 310–323, Mar. 2007.

[7] D. R. Williams, *Mars Fact Sheet*, Sep. 2016.

[8] G. A. Soffen, "Mars and the Remarkable Viking Results," *Journal of Spacecraft and Rockets*, vol. 15, no. 4, pp. 193–200, Jul. 1978.

[9] S. T. t. A. D. S. Technology and 1995, "Return to the Red Planet: An Overview of the Mars Pathfinder Mission," *arc.aiaa.org*,

[10] A Steltzner, P Desai, W Lee, and R Bruno, "The Mars exploration rovers entry descent and landing and the use of aerodynamic decelerators," *17th AIAA Aerodynamic* . . ., 2003.

[11] A. D. Steltzner, A Miguel San Martin, T. P. Rivellini, A. Chen, and D. Kipp, "Mars Science Laboratory Entry, Descent, and Landing System Development Challenges," *Journal of Spacecraft and Rockets*, vol. 51, no. 4, pp. 994–1003, Jul. 2014.

[12] A Sengupta, A Steltzner, and A Witkowski, "An overview of the Mars Science Laboratory parachute decelerator system," *2007 IEEE Aerospace* . . ., 2007.

[13] A Witkowski and R Bruno, "Mars Exploration Rover Parachute Decelerator System Program Overview," *AIAA Paper*, 2003.

[14] A. Witkowski, M. Kandis, and D. Adams, "Mars Scout Phoenix Parachute System Performance," in *20th AIAA Aerodynamic Decelerator Systems Technology Conference and Seminar*, Reston, Virigina: American Institute of Aeronautics and Astronautics, Jun. 2012, ISBN: 978-1-60086-969-3.

[15] E. J. Fallon, "System design overview of the Mars Pathfinder parachute decelerator subsystem," *AIAA,(97-1511)*, 1997.

[16] J. Cruz, R. Mineck, D. Keller, and M. Bobskill, "Wind Tunnel Testing of Various Disk-Gap-Band Parachutes," in *17th AIAA Aerodynamic Decelerator Systems Technology Conference and Seminar*, Reston, Virigina: American Institute of Aeronautics and Astronautics, Jun. 2012, ISBN: 978-1-62410-087-1.

[17] K. T. Edquist, A. M. Korzun, and A. A. Dyakonov, "Development of Supersonic Retropropulsion for Future Mars Entry, Descent, and Landing Systems," *Journal of Spacecraft ...*, 2014.

[18] A. M. Korzun, *Aerodynamic and performance characterization of supersonic retropropulsion for application to planetary entry and descent*, Thesis (Ph.D.)–Aerospace Engineering, Georgia Institute of Technology, 2012. Atlanta, Ga, 2012.

[19] K. T. Edquist, S. A. Berry, M. N. Rhode, B. Kelb, A. Korzun, A. A. Dyakonov, K. A. Zarchi, D. G. Schauerhamer, and E. A. Post, *Supersonic Retropropulsion Technology Development in NASA's Entry, Descent, and Landing Project*. Jun. 2012, ISBN: 20120014589.

[20] E. S. Love, C. E. Grigsby, L. P. Lee, and M. J. Woodling, *Experimental and Theoretical Studies of Axisymmetric Free Jets*. Jan. 1959, ISBN: 19980228067.

[21] J. N. Hefner and J. W. Keyes, "Effect of forward-facing jets on aerodynamic characteristics of blunt configurations at Mach 6.," *Journal of Spacecraft and Rockets*, 1967.

[22] E. S. Love, *A reexamination of the use of simple concepts for predicting the shape and location of detached shock waves*. Dec. 1957, ISBN: 19930085019.

[23] W. E. Moeckel, *Flow Separation Ahead of Blunt Bodies at Supersonic Speeds*. Jul. 1951, ISBN: 19930083006.

[24] J. N. Hefner and J. W. Keyes, "Effect of forward-facing jets on aerodynamic characteristics of blunt configurations at Mach 6.," *Journal of Spacecraft and Rockets*, vol. 4, no. 4, pp. 533–534, Apr. 1967.

[25] A. M. Korzun, R. D. Braun, and J. R. Cruz, "Survey of Supersonic Retropropulsion Technology for Mars Entry, Descent, and Landing," *Journal of Spacecraft and Rockets*, vol. 46, no. 5, pp. 929–937, Sep. 2009.

[26] W. E. Moeckel, *Flow Separation Ahead of Blunt Bodies at Supersonic Speeds*. Jul. 1951, ISBN: 19930083006.

[27] P. O. Jarvinen and R. H. Adams, *The aerodynamic characteristics of large angled cones with retrorockets*. Feb. 1970, ISBN: 19720005324.

[28] R. H. Adams and P. O. Jarvinen, *The effects of retrorockets on the aerodynamic characteristics of conical aeroshell planetary entry vehicles*, 1970.

[29] N Charczenko and K. W. Hennessey, "Investigation of a retrorocket exhausting from the nose of a blunt body into a supersonic free stream," 1961.

[30] R. M. Ghee, "Effects of a Retronozzle Located at the Apex of a 140 deg Blunt Cone at Mach Numbers of 3.00, 4.50, and 6.00," 1971.

[31] S. A. Berry, C. T. Laws, W. L. Kleb, M. N. Rhode, C. Spells, A. C. Mccrea, K. A. Trumble, D. G. Schauerhamer, and W. L. Oberkampf, "Supersonic retro-propulsion experimental design for computational fluid dynamics model validation," in *2011 IEEE Aerospace Conference*, IEEE, pp. 1–15, ISBN: 978-1-4244-7350-2.

[32] S. A. Berry, "Supersonic Retropropulsion Experimental Results from the NASA Ames 9- x 7-Foot Supersonic Wind Tunnel," Tech. Rep., May 2012.

[33] S. A. Berry and M. N. Rhode, *Supersonic Retropropulsion Test 1853 in NASA LaRC Unitary Plan Wind Tunnel Test Section 2*. Apr. 2014, ISBN: 20140006403.

[34] S. A. Berry, M. Rhode, K. Edquist, and C. Player, "Supersonic Retropropulsion Experimental Results from the NASA Langley Unitary Plan Wind Tunnel," in *42nd AIAA Thermophysics Conference*, Reston, Virigina: American Institute of Aeronautics and Astronautics, Jun. 2012, ISBN: 978-1-62410-146-5.

[35] N. M. Bakhtian and M. J. Aftosmis, "Analysis of Inviscid Simulations for the Study of Supersonic Retropropulsion," in *29th AIAA Applied Aerodynamics Conference*, Reston, Virigina: American Institute of Aeronautics and Astronautics, Jun. 2012, ISBN: 978-1-62410-145-8.

[36] A. M. Korzun, C. E. Cordell Jr., and R. D. Braun, "Comparison of inviscid and viscous aerodynamic predictions of supersonic retropropulsion flowfields," *AIAA Paper*, 2010.

[37] N. M. Bakhtian and M. J. Aftosmis, "Parametric Study of Peripheral Nozzle Configurations for Supersonic Retropropulsion," *Journal of Spacecraft and Rockets*, vol. 47, no. 6, pp. 935–950, Nov. 2010.

[38] A. M. Korzun and R. D. Braun, "Application of a Reynolds-Averaged Navier–Stokes Approach to Supersonic Retropropulsion Flowfields," *Journal of Spacecraft and Rockets*, vol. 50, no. 5, pp. 961–980, Sep. 2013.

[39] C. E. Cordell Jr., I. G. Clark, and R. D. Braun, "CFD verification of supersonic retropropulsion for a central and peripheral configuration," in *2011 IEEE Aerospace Conference*, IEEE, pp. 1–22, ISBN: 978-1-4244-7350-2.

[40] A. M. Korzun, C. E. Cordell Jr., and R. D. Braun, "Computational Aerodynamic Predictions of Supersonic Retropropulsion Flowfields," *Journal of Spacecraft and Rockets*, vol. 50, no. 5, pp. 950–960, Sep. 2013.

[41] D. Schauerhamer, K. Trumble, W. Kleb, J.-R. Carlson, and K. Edquist, "Continuing Validation of Computational Fluid Dynamics for Supersonic Retropropulsion," in *50th AIAA Aerospace Sciences Meeting including the New Horizons Forum and Aerospace Exposition*, Reston, Virigina: American Institute of Aeronautics and Astronautics, Jun. 2012, ISBN: 978-1-60086-936-5.

[42] C. E. Cordell Jr., "Computational fluid dynamics and analytical modeling of supersonic retropropulsion flowfield structures across a wide range of potential vehicle configurations," 2013.

[43] *NASA, SpaceX Share Data On Supersonic Retropropulsion*, Sep. 2016.

[44] S. J. Hoffman and D. I. Kaplan, *Human Exploration of Mars: The Reference Mission of the NASA Mars Exploration Study Team*. Jul. 1997, ISBN: 19980037039.

[45] B. G. Drake, *Reference mission version 3.0: addendum to the human exploration of Mars: the reference mission of the NASA Mars exploration study team*, 1998.

[46] J. T. J. Foughner, *Viking Mars Mission Support Investigations in the Langley Transonic Dynamics Tunnel*. May 1980, ISBN: 19800015853.

[47] B Raiszadeh, P. N. Desai, and R Michelltriee, "Mars Exploration Rover Heat Shield Recontact Analysis," *21st AIAA Aerodynamic . . .*, 2011.

[48] D. W. Way, R. W. POWELL, and A Chen, "Mars Science Laboratory: Entry, descent, and landing system performance," *IEEE Aerospace Conference*, pp. 1–19, 2007.

[49] D. W. Way, J. L. Davis, and J. D. Shidner, *Assessment of the Mars Science Laboratory Entry, Descent, and Landing Simulation*. Feb. 2013, ISBN: 20130010129.

[50] J. P. Decker and A. W. Wilhite, "Technology and methodology of separating two similar size aerospace vehicles within the atmosphere," *AIAA Paper*, 1975.

[51] *Image. x-15a-2 launch from b-52 with ablative coating and external tanks*, https://www.dfrc.nasa.gov/Gallery/Photo/X-15/Large/EC68-1889.jpg, Accessed: 2017-09-30.

[52] B. N. Pamadi and N. J. Hotcko, "Simulation and Analyses of Multi-Body Separation in Launch Vehicle Staging Environment," pp. 1–40, Nov. 2006.

[53] D. D. Tomlin, "Space shuttle Solid Rocket Booster (SRB) separation," Nov. 1975.

[54] B. N. Pamadi, T. A. Neirynck, N. J. Hotcko, W. I. Scallion, K. J. Murphy, and P. F. Covell, "Simulation and Analyses of Stage Separation of Two-Stage Reusable Launch Vehicles," *Journal of Spacecraft and Rockets*, vol. 44, no. 1, pp. 66–80, Jan. 2007.

[55] M. Toniolo, P. Tartabini, B. Pamadi, and N. Hotchko, "Constraint Force Equation Methodology for Modeling Multi-Body Stage Separation Dynamics," in *46th AIAA Aerospace Sciences Meeting and Exhibit*, Reston, Virigina: American Institute of Aeronautics and Astronautics, Jun. 2012, pp. 1–15, ISBN: 978-1-62410-128-1.

[56] B. Pamadi, T. Neirynck, P. Covell, N. Hotchko, and D. Bose, "Simulation and Analyses of Staging Maneuvers of Next Generation Reusable Launch Vehicles," in *AIAA Atmospheric Flight Mechanics Conference and Exhibit*, Reston, Virigina: American Institute of Aeronautics and Astronautics, Jun. 2012, pp. 1–20, ISBN: 978-1-62410-072-7.

[57] B. Pamadi, P. Tartabini, and B. Starr, "Ascent, Stage Separation and Glideback Performance of a Partially Reusable Small Launch Vehicle," in *42nd AIAA Aerospace Sciences Meeting and Exhibit*, Reston, Virigina: American Institute of Aeronautics and Astronautics, Jun. 2012, pp. 1–17, ISBN: 978-1-62410-078-9.

[58] Gary, "Estimation of Supersonic Stage Separation Aerodynamics of Winged-Body Launch Vehicles Using Response Surface Methods," pp. 1–34, Jun. 2008.

[59] D. T. Chan, D. J. Dalle, S. E. Rogers, and J. T. Pinier, "Space Launch System Booster Separation Aerodynamic Database Development and Uncertainty Quantification," *54th AIAA Aerospace ...*, 2016.

[60] J. P. Arrington and J. J. Jones, *Shuttle Performance: Lessons Learned*. Oct. 1983, ISBN: 19840002048.

[61] D. J. Dalle, S. E. Rogers, W. M. Chan, and H. C. Lee, *Inviscid and Viscous CFD Analysis of Booster Separation for the Space Launch System Vehicle*. Jan. 2016, ISBN: 20160004986.

[62] D. J. Dalle and S. E. Rogers, "Output-Based Adaptive Meshing Applied to Space Launch System Booster Separation Analysis," *33rd AIAA Applied Aerodynamics Conference*, 2015.

[63] S. E. Rogers, D. J. Dalle, and W. M. Chan, "CFD Simulations of the Space Launch System Ascent Aerodynamics and Booster Separation," in *53rd AIAA Aerospace Sciences Meeting*, Reston, Virginia: American Institute of Aeronautics and Astronautics, Jan. 2015, pp. 1–34, ISBN: 978-1-62410-343-8.

[64] B. Drake, "Human Exploration of Mars Design Reference Architecture 5.0Addendum #2," pp. 1–598, Feb. 2014.

[65] G. L. Brauer, D. E. Cornick, and R Stevenson, "Capabilities and applications of the Program to Optimize Simulated Trajectories (POST). Program summary document," 1977.

[66] D. J. Dalle, S. E. Rogers, H. C. Lee, and W. M. Chan, "Inviscid and Viscous CFD Analysis of Booster Separation for the Space Launch System Vehicle," in *54th AIAA Aerospace Sciences Meeting*, Reston, Virginia: American Institute of Aeronautics and Astronautics, Jan. 2016, pp. 864–29, ISBN: 978-1-62410-393-3.

[67] M. Gusman, C. Kiris, and M. Barad, "Aerodynamic Database Generation for SRB Separation from a Heavy Lift Launch Vehicle," in *29th AIAA Applied Aerodynamics Conference*, Reston, Virigina: American Institute of Aeronautics and Astronautics, Jun. 2012, pp. 2011–11, ISBN: 978-1-62410-145-8.

[68] P. E. Gill, W Murray, M. A. Saunders, and M. H. Wright, *User's guide for NPSOL (Version 4.0): a Fortran package for nonlinear programming, Report SOL 86-2, Department of Operations Research*, 1986.

[69] H. L. Justh, C. G. Justus, and H. S. Ramey, "Mars-GRAM 2010: improving the precision of Mars-GRAM," 2011.

[70] M Aftosmis, M Berger, and G Adomavicius, "A parallel multilevel method for adaptively refined Cartesian grids with embedded boundaries," in *38th Aerospace Sciences Meeting and Exhibit*, Reston, Virigina: American Institute of Aeronautics and Astronautics, Feb. 2013, pp. 281–16.

[71] M. Nemec and M. J. Aftosmis, "Adjoint Error Estimation and Adaptive Refinement for Embedded-Boundary Cartesian Meshes," in *18th AIAA Computational Fluid Dy-*

namics Conference, Reston, Virigina: American Institute of Aeronautics and Astronautics, Jun. 2012, pp. 1–18, ISBN: 978-1-62410-129-8.

[72] M. G. Fernández-Godino, C. Park, N.-H. Kim, and R. T. Haftka, "Review of multi-fidelity models," *arXiv.org*, Sep. 2016. arXiv: 1609.07196v3 [stat.AP].

[73] *Gaussian process regression models*, https://www.mathworks.com/help/stats/gaussian-process-regression-models.html, 2018 (accessed 2018-02-11).

[74] C. E. Rasmussen and C. K. I. Williams, "Gaussian Processes in Machine Learning," 2011.

[75] A Forrester, A Sobester, and A Keane, *Engineering design via surrogate modelling: a practical guide*, 2008.

[76] C. Park, R. T. Haftka, and N. H. Kim, "Remarks on multi-fidelity surrogates," pp. 1–22, Feb. 2017.

[77] F. A. C. Viana, R. T. Haftka, and V. Steffen, "Multiple surrogates: how cross-validation errors can help us to obtain the best predictor," *Structural and Multidisciplinary Optimization*, vol. 39, no. 4, pp. 439–457, Jan. 2009.

[78] M. C. Kennedy, A. O. Biometrika, and 2000, "Predicting the output from a complex computer code when fast approximations are available," *academic.oup.com*,